

**Study on atomic-scale plasma process based on  
substrate-temperature control by frequency-domain low-coherence  
interferometry**

**TSUTSUMI Takayoshi**

2015

Department of Electrical Engineering and Computer Science  
Graduate School of Engineering, Nagoya University

## **Chapter 1 Introduction**

1.1 History of large scale integrated circuits .....	1
1.2 Plasma etching process system .....	3
1.3 Influence of substrate temperature on plasma etching processes .....	6
1.3.1 Sticking coefficient .....	6
1.3.2 Rate of chemical reaction .....	8
1.3.3 Heat diffusion in gases .....	8
1.4 Energy influx at substrate surface during plasma process .....	10
1.5 Demand for development of temperature measurement and control .....	13
1.6 Purposes and construction of this thesis .....	16
1.7 References .....	18

## **Chapter 2 Diagnostic and evaluation methods for plasma internal parameters and etched feature**

2.1 Introduction .....	21
2.2 Substrate temperature measurement system .....	22
2.2.1 Frequency-domain low-coherence interferometry (FD-LCI) .....	22
2.2.2 Principle of temperature measurement .....	25
2.3 Temporal variation of substrate temperature .....	26
2.4 Scanning electron microscopy (SEM) .....	28
2.5 References .....	30

## **Chapter 3 Development of frequency-domain low-coherence interferometry for measuring semiconductor-substrate temperature**

3.1 Introduction .....	32
3.2 Experimental details .....	34
3.3 Results and discussion .....	36
3.3.1 Measurements of optical path length change and temperature .....	36
3.3.2 Effects of dispersion and polarization on optical path length measurement .....	43

## Contents

3.3.3 Relations between center wavelength of light source and measurement characteristic .....	44
3.4 Conclusion .....	54
3.5 References .....	56

### **Chapter 4 Measuring substrate temperature during plasma processes**

4.1 Introduction .....	59
4.2 Experimental details .....	61
4.3 Results and discussion .....	63
4.3.1 Model of heat balance in the substrate .....	63
4.3.2 Temporal variation of substrate temperature during plasma process .....	73
4.4 Conclusion .....	77
4.5 References .....	79

### **Chapter 5 Etching processes of organic films with precise control of substrate temperature**

5.1 Introduction .....	82
5.2 Experimental details .....	84
5.3 Results and discussion .....	87
5.3.1 Etch process with temporal control of substrate temperature .....	87
5.3.2 Influence of substrate temperature on etch rates and features for organic film .....	93
5.4 Conclusion .....	99
5.5 References .....	101

### **Chapter 6 Conclusions and future works**

6.1 Conclusion of present research .....	104
6.2 Scopes for future works .....	107

## Contents

<b>Acknowledgements</b> .....	110
<b>List of Papers</b> .....	114



## **Chapter 1 Introduction**

### **1.1 History of large scale integrated circuits**

Recently, electric devices have made our life convenient in various areas. In the latter half of the 1990s, Cell-phones have been widely used as communication tools. In the 2000s, the demand for electric devices has increased in new fields such as digital home electrical appliances, game machines, and cars. Additionally, NAND-type flash memory has been developed as new memory medium. Behind this background, advance of microfabrication techniques has contributed a great deal to the spread of semiconductor devices. As expressed in Moore's Law, the number of components in large scale integrated circuits (LSIs) has increased twofold in about 18 months. For example, the progress of the number of transistors per microprocessor unit (MPU) made in Intel Corporation. The MPU consisted of about 2,300 transistors was developed in 1971. Pentium(R) 4 processor™ consisted of 55 million transistors developed in 2001. Intel® Core™ i7 Processor consisted of transistors of 731 million in 2008.

Miniaturization of the semiconductor devices has contributed to not only improvement of the speed of processing and the consumed power, but also the cost reduction. Cost per one transistor has been significantly reduced to approximately 1/100 by reducing 10 times from its original size.

The half pitches of the MPU and dynamic random access memory (DRAM) are usually used as an index of miniaturization of semiconductor devices by International Technology Roadmap for Semiconductors (ITRS) [1]. As shown in Table 1.1, required values of the half pitch of 2015 are 31.8 nm in MPU, 15 nm in flash memory, 24 nm in DRAM. In general, the wire process at about one order of magnitude more precision than the half pitch is required. In other words, the required precision is about several times as long as the lattice constant of Silicon (5.4 Å). As miniaturization of semiconductor devices, the precision required for the fabrication processes have

## Chapter 1

approach the atomic scale.

In the manufacture of semiconductor devices, it is necessary to control the high-precision process since the processing dimension approaches the atomic scale. Especially, the plasma etching process, such as radical-enhanced isotropic etching and anisotropic etching based on directional reactive ions by the plasma process, plays an important role in microfabrication. Hence, it is necessary for further miniaturization to control the precision of the plasma etching process.

Table 1.1 Interconnect technology requirements.

Year of production	2015	2016	2017	2018	2019	2020
MPU/ASIC Metal 1 1/2 pitch (nm)	31.8	28.3	25.3	22.5	20.0	17.9
DRAM 1/2 pitch (nm)	24	22	20	18	17	15
Flash 1/2 pitch (nm)	15	14.2	13.0	11.9	11.9	11.9
FinFET Fin width (nm)	5.3	4.9	4.4	4.1	3.7	3.4

## 1.2 Plasma etching process system

Plasma etching process has been an essential component for the microfabrication of materials used to semiconductor devices with high precision. The parallel plate type discharge plasma has been mainly used as typical etching process from the beginning. Supplying radio frequency (RF) power to parallel plate electrodes, this system couples the external power supply to the plasma capacitively. This system is called capacitively coupled plasma (CCP) which has an advantage to achieve uniform processing characteristics. As shown in Fig. 1.1, the plasma is generated by applying an RF power to the electrode in a vacuum chamber, into which process gases are introduced. Radicals and ions are generated since molecules and atoms in gas dissociate and ionize due to the electron collision in the plasma. Etching of material is performed by chemical reaction between the radicals and a surface of the material. Moreover, the negative bias voltage on the substrate is generated by the RF power. This is because the mobility of the electron is faster than that of the ion.

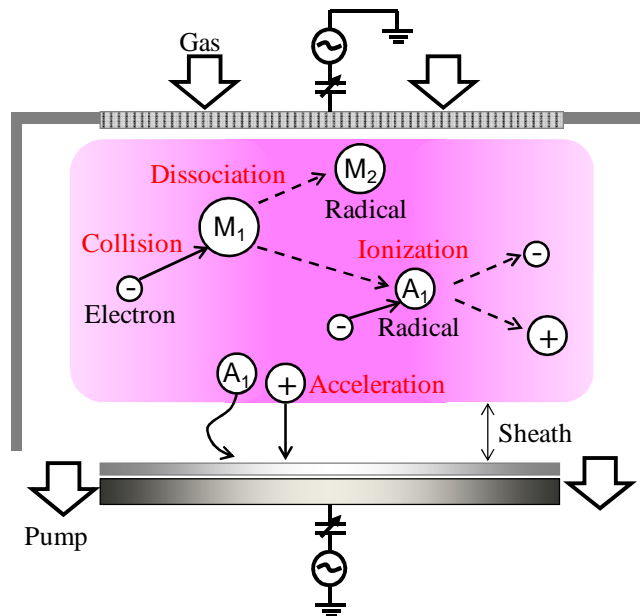


Fig. 1.1 Schematic diagram of parallel plate type discharge plasma.

As shown in Fig. 1.2(a), the electron reaches the substrate earlier than the ion at the beginning of plasma generation. This indicates that the substrate is charged negatively. On the other hand, the positive ion accelerates and strikes to the substrate by the electric field above the negatively charged substrate. As shown in Fig. 1.2(b), the negative self bias voltage ( $V_{dc}$ ) on the substrate is generated continuously due to the balance between the incident electrons and ions within the one cycle of RF in a steady-state. Striking vertically to the substrate by the self bias, the ions assist the chemical reaction between the radicals and the materials. Hence, CCP process achieves the anisotropic etching.

Microfabrication of the semiconductor device has been required to etch the material vertically in nanometer scale. As shown in Fig. 1.3, however, charging of the material or reflection of ion at the mask causes the etching of sidewalls. Plasma etching processes should be performed with the control of sidewalls of the etched feature. In the

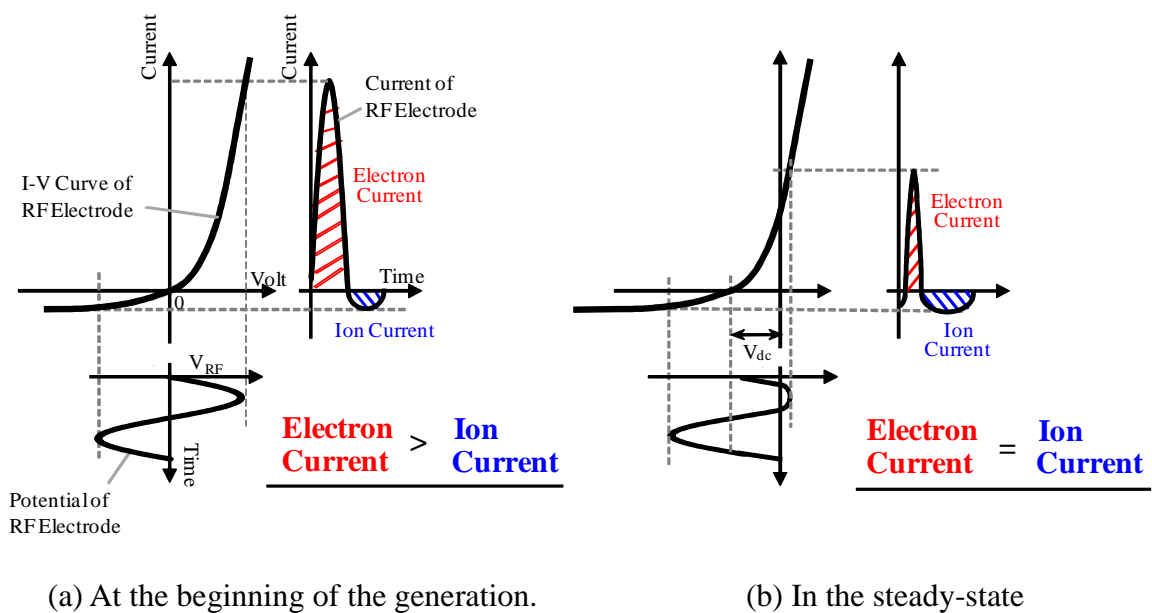


Fig. 1.2 Time-varying potential and current of RF electrode.

case of the etching of  $\text{SiO}_2$  [2-4],  $\text{CF}_x$  radicals sticking on a mask and sidewalls prevent the etching of the mask and the sidewalls. The process used the gases mixed a fluorocarbon type gas and oxygen or argon gas. The reaction between Si atom and F atom, O atom and C atom generated compounds such as  $\text{SiF}_x$  and CO.  $\text{CF}_x$  radical resulting from the dissociation of fluorocarbon type gases deposit on the surface of  $\text{SiO}_2$ . The ions are bombarded with enough energy to break the bond between Si atom and O atom. The products resulting from these chemical reactions and fluorocarbon type polymer prevent the etched sidewalls. Hence, the plasma etching processes achieve the anisotropic etching by not only the ion assistance but also the deposition on the sidewalls.

In the anisotropic etching with a high accuracy, the rate of chemical reaction and the rate of the deposition play the important role. These factors strongly depend on the temperature. Hence, the temperature of the reaction fields such as the substrate has a great influence on the etched feature of the material [5-13].

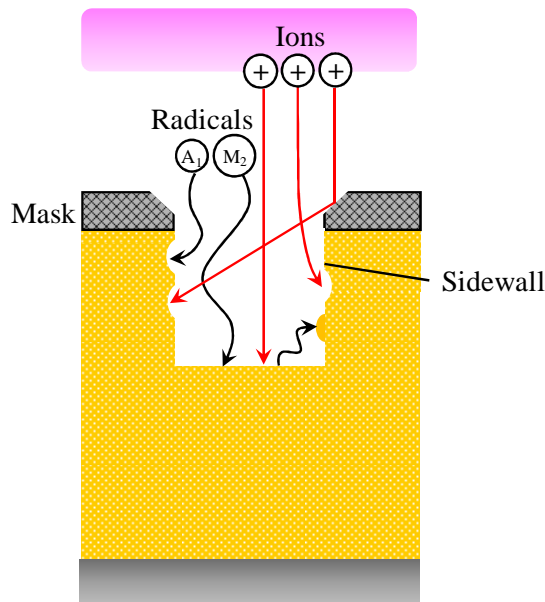


Fig. 1.3 Schematic diagram of plasma etching process.

### 1.3 Influence of substrate temperature on plasma etching processes

In the plasma etching processes with high RF power, the substrate temperature rises rapidly during plasma exposures and impose a temperature change above a few hundred degrees. This phenomenon complicates the interactions between the plasma and the substrate surface, and the control of etched features in the nanometer scale. In this section the dependence of temperature at reaction field on several factors under plasma processes are described.

#### 1.3.1 Sticking coefficient

The temperature dependence of the sticking or the recombination probability has been reported by many researchers [14-19]. The sticking probability consists of two factors, which are a precursor-mediated sticking probability of physisorption and a direct sticking probability of chemisorption [14]. Figure 1.4 shows the potential energy curve for molecular sticking. There is an activation barrier ( $E_a$ ) between the physisorption and the chemisorption. Since the probability of physisorption strongly depends on the surface temperature, the sticking coefficient should exhibit a dependence of substrate temperature.

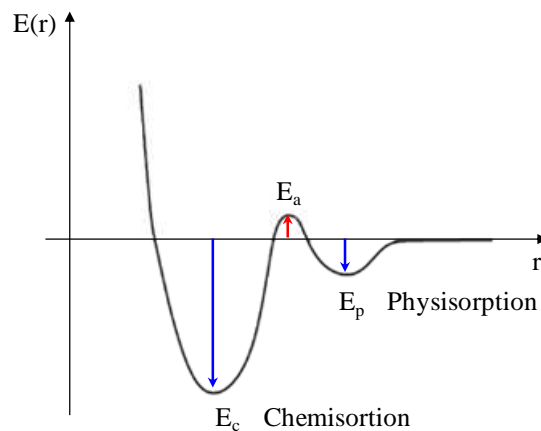


Fig. 1.4 Schematic illustration of potential energy curve for the sticking model.

The influence of sticking probability on the etched feature is described in the plasma etching process of  $\text{SiO}_2$  film. The radicals resulting from the dissociation of fluorocarbon type gas by the electron collision stick as protection film on the sidewalls in the hole and the wall of the chamber [12]. In the case of the low substrate temperature, the etched feature is shown in Fig. 1.5(a). Since the sticking probability of fluorocarbon type radical increased with decreasing the substrate temperature, the radicals deposit thickly on the upper part of sidewalls compared to the lower parts of the sidewalls. The phenomena indicated that the mask and the upper part of the sidewalls are protected from the ion bombardment. While the etched feature form the taper profile because the deposition material at the upper part of the sidewalls perform as mask. Under higher temperatures of the substrate, the etched feature is shown in Fig. 1.5(b). Since many radicals stick more on the upper part of the sidewalls, the etched feature approaches vertical profile. These mechanisms confirmed that the influence of substrate temperature on the sticking probability contributes to the etched feature.

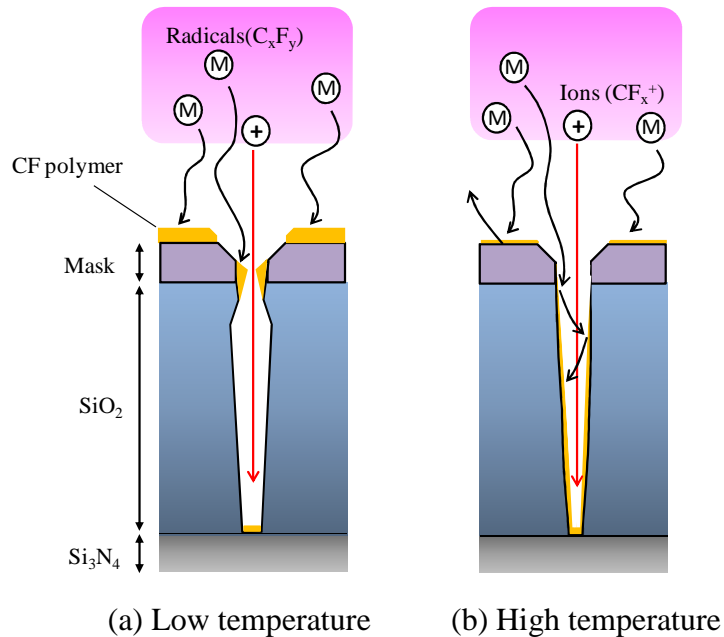


Fig. 1.5 Etching features (a) at low temperature and (b) at high temperature.

### 1.3.2 Rate of chemical reaction

Reaction rate can be classified into four types depending on temperature. In many reactions, reaction rate increases with temperature. In 1889, Arrhenius discovered that the temperature dependence of reactions could be given by the following equation:

$$k = Ae^{-E_a/RT}, \quad (1.1)$$

where  $k$  is the rate constant,  $A$  is called the frequency factor or pre-exponential factor,  $E_a$  is the activation energy ( $\text{kJ mol}^{-1}$ ),  $R$  is the gas constant, and  $T$  is the absolute temperature. The activation energy is the minimum amount of energy required to initiate a chemical reaction. The frequency factor,  $A$ , represents the frequency of collisions between reactant molecules. As expressed in Eq. (1.1), the surface temperature of the substrate, which is reaction field, influence the reaction rate strongly due to exponential change of the reaction rate as a function of the temperature. The temperature dependence of the loss probability of atoms on the substrate surface in plasma is usually given by an Arrhenius law [15-16].

### 1.3.3 Heat diffusion in gases

The temperature influences not only the chemical reaction, but also the thermal diffusion of neutral species. From equation of state for perfect gas, gas temperature and density is inversely proportional in the constant pressure. The gas density increases locally at the parts of higher temperature in the process chamber. When the substrate temperature is higher compared to the other parts (e.g. an electrode, a wall, a focus ring, etc.), it is expected that the radical supplied for chemical reaction decrease. In addition to change of radical density, decreasing the gas density causes decreasing the charged particles such as the ion and the electron assuming that the ionization probability by the electron collision is proportional to the gas density.

In the case of the process using several process gases, the low-mass molecules

## Chapter 1

contribute to balance the homogeneous distribution of the gas temperature in the chamber due to the mobility of the molecule depending on mass. The molecule with lower mass tends to concentrate on the high-temperature area.

The spatial distribution of gas temperature influences the characteristic of plasma etching processes by the interactions among the reactive species and materials.

### 1.4 Energy influx at substrate surfaces during plasma process

Since the interaction between the plasma and the material relate closely to the substrate temperature, the precise method is necessary to monitor and control the substrate temperature [20]. As shown in Fig. 1.6, the substrate is heated during plasma process due to the energy influx by heat radiation, charge carriers, and neutral species [21]. Comprehensive understanding of the heat balance at the substrate is required to control the substrate temperature which varies with process time. In this section, the temporal variation of the substrate temperature and the energy influx from the plasma to the substrate are described.

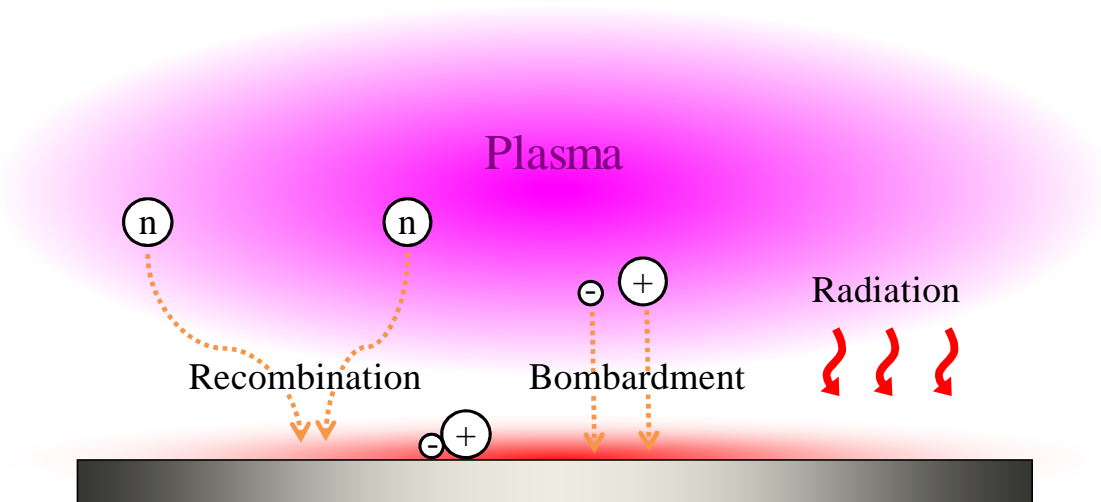


Fig. 1.6 Components of the energy influx to the substrate during plasma process.

As described above, the surface of the substrate heated due to the energy transfer from the plasma. In general, the total power input  $\dot{Q}_{\text{IN}}$  is given by

$$\dot{Q}_{\text{IN}} = \int (J_{\text{rad}} + J_{\text{ch}} + J_{\text{n}} + J_{\text{ads}} + J_{\text{react}} + J_{\text{ext}}) dA. \quad (1.2)$$

$J_{\text{rad}}$  is the heat radiation towards the surface,  $J_{\text{ch}}$  is the power transferred by charge carriers (electrons and ions), and  $J_{\text{n}}$  is the contribution of neutral species of the background gas and the neutral particles contributing to the film growth [21]. The latter terms in Eq. (1.2) are energy released by adsorption or condensation  $J_{\text{ads}}$  and the reaction energy of exothermic processes including molecular surface recombination  $J_{\text{react}}$ . Also power input by external sources  $J_{\text{ext}}$  influences the thermal balance of the substrate.

In a common low-temperature plasma process the contribution of heat radiation is ignorable, but in some plasma processes such as combination with CVD or arc evaporation it can increase by several tens of percent [22].

The main source of energy transfer is due to charge carriers, which get their directed kinetic energy by acceleration in the sheath in front of a surface. Generally, the total energy flux of charged particles is given by the product of the particle flux density to the substrate surface and the mean particle energy. Usually, the energy of ions consists of a potential and a kinetic part. In detail, the two components, which are positive ions and recombination between positive ions and electrons, may contribute to the energy influx  $J_{\text{ch}}$  by charge carriers from the plasma to the substrate during low-temperature plasma processes.

In the plasma etching process where the heat flux to the surface is dominated by the ion bombardment, the contribution of the potential energy term can be very substantial (several tens of percent) for low kinetic energies [23]. For insulating materials the potential energy of the ion released mainly consists of the recombination and the adsorption energy. In addition to the potential energy, ions transfer a part of their

## Chapter 1

kinetic energy when striking a surface. In the non-isothermal plasma process, a part of kinetic energy given to the surface depends on the substrate bias voltage, the mass ratio of the colliding particles, the angle of incidence, and the energy transfer coefficient [24].

In addition to charge carriers, neutrals contribute to the thermal power balance. In general, the heat of adsorption may contribute to the energy transfer by neutrals. In an adsorbed state the adsorption heat is released, which results in heating the surface. Excepting magnetron discharge sputtering [25], thermal evaporation and expanding arc plasmas [26], however, the heat transfer by the neutrals is insubstantial compared to the charged particles.

## **1.5 Demand for development of temperature measurement and control**

There are two major classes of methods for measuring the temperature by contact-type and noncontact-type. Table 1.2 shows the comparison among different measurement methods of the substrate temperature. The contact-type method measured the sample temperature by heat transfer from the sample to the probe. For using these methods, it is required to pay attention to the delay of heat transfer and heat conductivity of a heat transfer medium. Thermocouples and fluorescence thermometers have been conventionally used as typical contact-type methods. Thermocouples have advantages in cost and measurement accuracy.

In semiconductor processes, plasmas are generated by applying the high-frequency power (RF, VHF, microwave). For example, up to 10 kW of RF power is applied to a Si wafer of 300 mm in diameter due to productivity enhancement. Under high-power process, thermocouples have several problems, insulation failure between the probe and the sample, inhomogeneous plasma, anomalous discharge. When implementing a range of measures such as placing an insulator between the probe and the sample, thermo responsiveness decreases significantly.

Plasma processes for semiconductor devices (e.g. chemical vapor deposition, etching, ashing, etc.) are performed at low pressures, where the high heat transfer from the sample to the probe is required. The high heat transfer is obtained by plane contact between the sample and the probe, since the contact thermal conductance is efficient. In general, the ideal plate contact is insufficient due to the asperity of surface. This indicates that the heat transfer by an atmosphere gas between the sample and the probe is dominant. At low pressures, the heat transfer by the atmosphere gas is inefficient. Hence, the heat transfer from the sample to the probe is performed only at the contact point. Decreasing the thermal responsiveness and insufficient contact often results in erroneous measurements [27, 28-29].

## Chapter 1

Infrared radiation thermometer has been conventionally used as typical noncontact-type method. The temperature of the sample is deduced from the radiation energy which varies depending on the temperature. This method has advantages in the thermal responsiveness and invasiveness.

The detector sensitivity and the emissivity of the sample are taken into account when the temperature is estimated from the radiation energy. In the case of a semiconductor substrate, the measured radiation energy is influenced by dependence of the temperature on the emissivity and transmittance of a grimy window.

The emissivity of a Si wafer, which is conventionally used for semiconductor devices, was reported by Sato [30]. Over 873 K, the temperature of the Si wafer is easily measured by radiation thermometer due to independence of temperature on the emissivity. In the temperatures under 543 K and wavelengths above 1100 nm, on the other hand, decreasing the radiation energy and shift of the distribution of the emissivity lead to low accuracy. Moreover, the background radiation by the chamber parts and the radiation from plasma influence the measurement accuracy.

These reasons indicate that typical thermometers are not applicable for measurement of semiconductor substrates at low pressure. Other noncontact methods were proposed by many researchers [31-37]. However, there remain difficulties such as their poor tolerance to mechanical disturbance, resulting in limited resolution and temperature ranges.

## Chapter 1

Table 1.2 Comparison among different measurement methods of the substrate temperature.

	Thermocouples	Fluorescence thermometer	Infrared radiation thermometer
Type	Contact	Contact	Noncontact
Sampling position	Bottom	Bottom	Top
Temperature range	-50 ~ 1300°C	10 ~ 400°C	485 ~ 1800°C (Si wafer)
Accuracy (under the atmosphere pressure)	±1.0°C	±1.0°C	±2.7°C
Responsiveness in the vacuum	Slow	Slow	Fast
Disturbance from the plasma	N/A	N/A	Yes IR from the plasma

## **1.6 Purposes and construction of this thesis**

The goal of this study is to investigate the influence of the substrate temperature on the etching processes and to control the plasma for atomic-scale plasma process. Firstly, it is necessary to understand the thermal balance and energetic condition during the plasma process. The author develops noncontact temperature monitoring system for semiconductor substrates during plasma processes. Finally, The author tries to control the etching feature in atomic-scale by clarifying the influence of the substrate temperature on the etched feature.

In Chapter 2, theories of substrate-temperature measurement by frequency-domain low coherence interferometry (FD-LCI) are described. The temporal variation of the substrate temperature was described to evaluate the energy flux from the plasma to the substrate. Moreover, Scanning electron microscopy used as measurement methods of etched features was introduced.

In Chapter 3, rapid high-precision temperature monitoring systems for semiconductor substrate were developed by frequency-domain low coherence interferometry. This system can potentially measure substrate temperatures in a few milliseconds. A plane-parallel semiconductor substrate results in removing the mirror from the optical interferometry. This is expected that this system is less sensitive to mechanical vibrations and has a potential to improve the measurement accuracy. In terms of usefulness, the characteristics of this method for the Si wafer were investigated.

In Chapter 4, energy balance of a substrate during plasma exposure was investigated. The energy influx from the plasma to the substrate and the energy loss in the substrate were understood by measuring the temporal variation of the temperature during plasma exposure. The model of the energy balance at substrate was constructed to estimate the heat flux from the plasma to the substrate in detail.

In Chapter 5, a precise plasma etching process was developed by controlling

## Chapter 1

the substrate temperature based on the FD-LCI system. The author introduced a system of feedback control of actual temperature monitored in real-time by dynamical change of on-off intervals of plasma discharges. Keeping the sticking probability of the radical and the rate of chemical reaction depending on the temperature constant, the dependence of etch rates and features on the substrate temperatures was evaluated.

Finally, the results in the present study were summarized and future works were described in Chapter 6.

## 1.7 References

- [1] Intern. Technol. Roadmap for Semicond. (Semicond. Indust. Associat., 2013).
- [2] J. W. Coburn and H. F. Winters, *J. Vac. Sci. Technol.* **16**, 391 (1979).
- [3] R. A. Gottscho, C. W. Jurgensen, and D. J. Vitkavage, *J. Vac. Sci. Technol. B* **10**, 2133 (1992).
- [4] T. Tatsumi, *J. Plasma Fusion Res.* **83**, 325 (2007).
- [5] T. Ohiwa, K. Horioka, T. Aricado, I Hasegawa, and H. Okano, *Jpn. J. Appl. Phys.* **31**, 405 (1992).
- [6] H. Oshio, T. Ichiki, and Y. Horiike, *J. Electrochemical Soc.* **147**, 4273 (2000).
- [7] N. Negishi and M. Izawa, *J. Plasma Fusion Res.* **83**, 330 (2007).
- [8] H. Sugai, K. Nakamura, Y. Hikosaka and M. Nakamura, *J. Vac. Sci Technol. A* **13**, 887 (1995).
- [9] S. Ito, K. Nakamura, and H. Sugai, *Jpn. J. Appl. Phys.* **33**, L1261 (1994).
- [10] M. Schaepkens, R. C. M. Bosch, T. E. F. M. Standaert, G. S. Oehrlein, and J. M. Cook, *J. Vac. Sci. Technol. A* **16**, 2099 (1998).
- [11] Y. Hikosaka, M. Nakamura, and H. Sugai, *Jpn. J. Appl. Phys.* **33**, 2157 (1994).
- [12] H. Abe, M. Yoneda, and N. Fujiwara, *Jpn. J. Appl. Phys.* **47**, 1435 (2008).
- [13] Y. Hikosaka, M. Nakamura, and H. Sugai, *Jpn. J. Appl. Phys.* **33**, 2157 (1994).
- [14] A. Doshita, K. Ohtani, and A. Namiki, *J. Vac. Sci. Technol. A* **16**, 265 (1998).
- [15] T. Belmonte, L. LefeÁvre, T. Czerwiec, H. Michel, and A. Ricard, *Thin Solid Films* **341**, 27 (1999).
- [16] Y. C. Kim and M. Boudart, *Langmuir* **7**, 2999 (1991).
- [17] J. Sarrette, B. Rouffer, and A. Ricard, *Plasma Process. Polym.* **3**, 120 (2005).
- [18] M. M. Pejović, G. S. Ristić, Č. S. Milosavljević, and M. M. Pejović, *J. Phys. D* **35**, 2536 (2002).
- [19] P. Macko, P. Veis, and G. Cernogora, *Plasma Sci. Technol.* **13**, 251 (2004).
- [20] H. Yamamoto, H. Kuroda, M. Ito, T. Ohta, K. Takeda, K. Ishikawa, H. Kondo, M.

## Chapter 1

- Sekine, and M. Hori, *Jpn. J. Appl. Phys.* **51**, 016202 (2012).
- [21] H. Kersten, H. Deutch, H. Steffen, G. M. W. Kroesen, and R. Hippler, *Vacuum* **63**, 385 (2001).
- [22] H. Steffen, H. Kersten, and H. Wulff, *J. Vac. Sci. Technol. A* **12**, 2780 (1994).
- [23] K. Kersten, R. J. M. M. Snijkers, J. Schulze, and G. M. W. Kroesen, J. Deutch, F. J. Hoog, *Appl. Phys. Lett.* **64**, 1496 (1994).
- [24] H. F. Winters and D. Horne, *Phys. Rev. B* **10**, 55 (1974).
- [25] F. Alder, H. Kersten, and H. Steffen, *Contrib. plasma phys.* **35**, 213 (1995).
- [26] H. Kersten and G. M. W. Kroesen, *J. Vac. Sci. Technol. A* **8**, 38 (1990).
- [27] I. Hussla, K. Enke, H. Grünwald, G. Lorenz, and H. Stoll, *J. Phys. D* **20**, 889 (1987).
- [28] A. Cardso and A. K. Srivastava, *J. Vac. Sci. Technol. A* **8**, 84 (1990).
- [29] C. Koshimizu, T. Ohta, T. Matsudo, S. Tuchitani, and M. Ito, *Appl. Phys. Express* **3**, 056201 (2010).
- [30] T. Sato, *Jpn. J. Appl. Phys.* **6**, 339 (1966).
- [31] J. L. Booth, B. T. Beard, J. E. Stevens, M.G. Blain, and T. L. Meisenheime, *J. Vac. Sci. Technol. A* **14**, 2356 (1996).
- [32] J. L. Cui, K. Amtmann, J. Ristein, and L. Ley, *J. Appl. Phys.* **83**, 7929 (1998).
- [33] U. J. Gibson and M. Chernushenko, *Opt. Express* **4**, 443 (1999).
- [34] V. M. Donnelly and J. A. McCaulley, *J. Vac. Sci. Technol. A* **8**, 84 (1990).
- [35] H. Sankur and W. Gunning, *Appl. Phys. Lett.* **56**, 2651 (1990).
- [36] K. L. Saenger, F. Tong, J. S. Logan, and W. M. Holber, *Rev. Sci. Instrum.* **63**, 3862 (1992).
- [37] J. Kikuchi, S. Fujimura, R. Kurosaki, and H. Yano, *J. Vac. Sci. Technol. A* **15**, 2035 (1997).

## Chapter 1

## **Chapter 2 Diagnostic and evaluation methods for plasma internal parameters and etched feature**

### **2.1 Introduction**

Plasma processes have been used for the manufacture of semiconductor devices. With a progression of the miniaturization of semiconductor devices, the more accurate etching processes, the more high reproducibility, and the high control processes have been required. To achieve highly sophisticated etching process, it is important to understand the interaction between the plasma and the material.

In this chapter, various measurement techniques used for analyzing for this thesis are described. For analysis of the substrate temperature during plasma processes, Frequency-domain low-coherence interferometry (FD-LCI) was used. The temporal variation of the substrate temperature was described for evaluating the energy flux from the plasma the substrate. Moreover, scanning electron microscopy (SEM) was carried out for evaluating etched features of organic low- $k$  films after plasma processes.

### **2.2 Substrate temperature measurement system**

#### **2.2.1 Frequency-domain low-coherence interferometry (FD-LCI)**

The schematic of a FD-LCI system is shown in Fig. 2.1. The optical system is based on a Michelson interferometer, which splits the beam into the reference and sample arm signals. Using a spectrometer, interferences between the reflections from the entire surface of the substrate and from the reference mirror are observed as a spectrum, which is commonly known as a spectral interferogram.

The interferogram  $I$  can be divided into three terms: DC,  $I_{dc}$ ; cross-correlation,  $I_{cc}$ ; and autocorrelation,  $I_{ac}$  [1]. In the sample arm, the incident light is reflected both at the front and back surfaces of the sample, e.g., a transparent substrate. With illumination

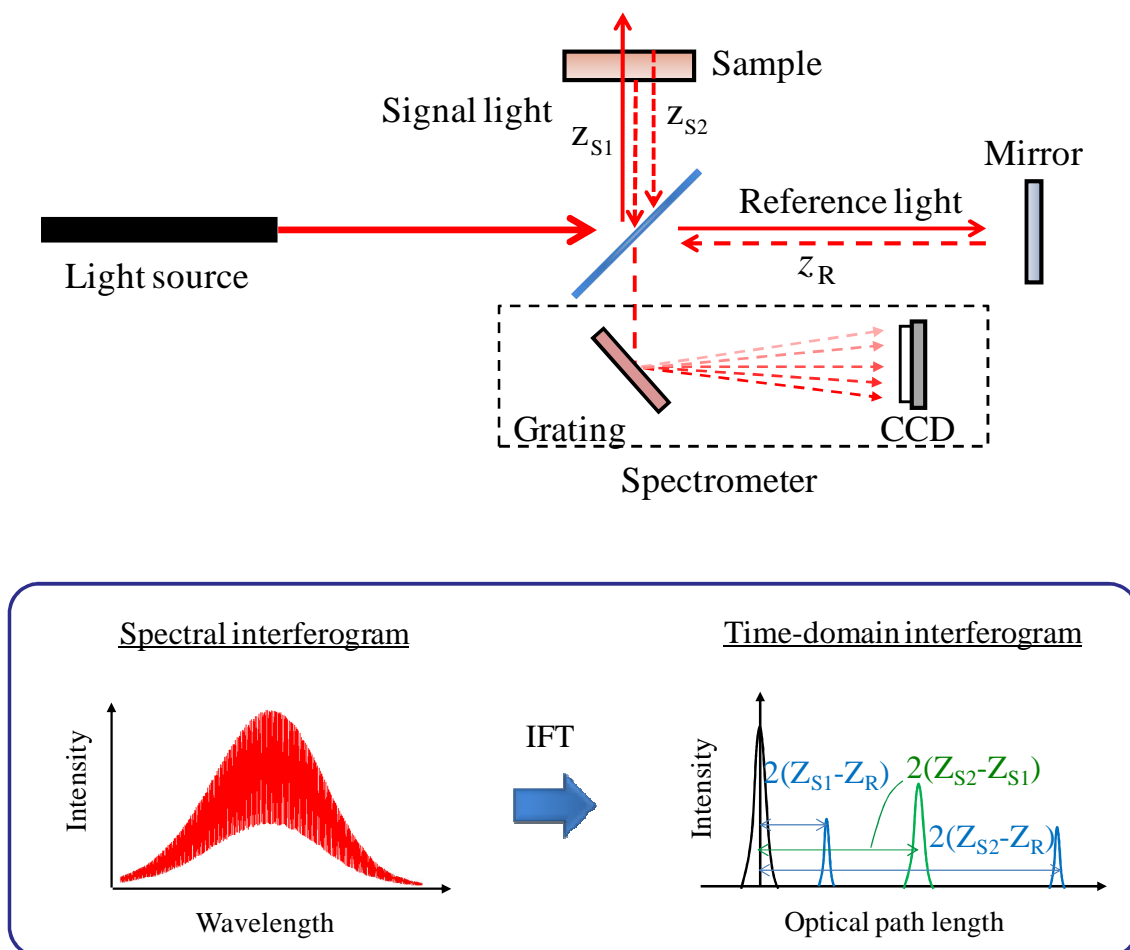


Fig. 2.1 The schematic of the conventional FD-LCI system for the semiconductor substrate.

## Chapter 2

from the light source having the spectral density  $S$  as a function of the wavenumber  $k$ , the interferogram terms are given by

$$I_{dc}(k) = S(k)(R_R + R_1 + R_2), \quad (2.1)$$

$$I_{cc}(k) = 2S(k) \sum_{n=1}^2 \sqrt{R_n} \cos[2k(z_R - z_n)], \quad (2.2)$$

$$I_{ac}(k) = 2S(k) \sqrt{R_1 R_2} \cos[2k(z_1 - z_2)], \quad (2.3)$$

where  $z_R$ ,  $z_1$ , and  $z_2$  are the positions in the  $z$ -axes of the reference mirror and the front and back surfaces of the substrate, respectively.  $R_R$  ( $=1$ ) is the reflectivity of the reference mirror.  $R_1$  and  $R_2$  are the reflectivities of the front and back surfaces of the substrate. The cross-correlation term  $I_{cc}$  and the autocorrelation term  $I_{ac}$  are expressed with cosine functions depending on both the light wavenumber and the distance between surfaces. Namely,  $(z_R - z_1)$  represents the distance between the reference arm and the front surface of the Si wafer, and  $(z_1 - z_2)$  represents the distance between the front and back surfaces of the Si wafer. While obeying the linear combinations of Fourier components with all lights simultaneously, an inverse Fourier transform of the spectral interferogram,  $i$ , can convert all the time-domain interferograms, as given by

$$i_{dc} = \gamma(z)(1 + R_1 + R_2), \quad (2.4)$$

$$i_{cc} = \sum_{n=1}^2 \sqrt{R_n} \{\gamma[z \pm 2(z_R - z_n)]\}, \quad (2.5)$$

$$i_{ac} = \sqrt{R_1 R_2} \{\gamma[z \pm 2(z_1 - z_2)]\}, \quad (2.6)$$

where  $\gamma(z)$  is the inverse Fourier transform of  $S(k)$ . If the light source spectral density has a Gaussian profile, the inverse Fourier transform  $\gamma$  given by

$$\gamma(z) = \exp \left[ - \left( \frac{z \Delta k}{\frac{I_c}{2\sqrt{\ln 2}}} \right)^2 \right], \quad (2.7)$$

where  $\Delta k$  is the full width at half maximum of the light source spectrum and  $l_c$  is the coherence length, which is dependent on measurement accuracy and the minimum measurable thickness of a substrate [2]. The coherence length  $l_c$  is given by

$$l_c = 2 \ln 2 \lambda_0^2 / \pi \Delta \lambda, \quad (2.8)$$

where  $\Delta \lambda$  is the full width at half maximum (FWHM) of the light spectrum profile and  $\lambda_0$  is the center wavelength of the light source. From these equations, DC, cross-correlation, and autocorrelation signals peak at  $z = 0$ , at the optical path length difference between the reference and sample arm signals, and at the optical path length difference between the front and back surfaces of a substrate, respectively. The optical path length of the substrate is equivalent to be the peak interval of cross-correlation signals. The peak position of autocorrelation corresponds to the optical path length of a substrate. If the reflections at the front and back surfaces of a sample show coherent interference, autocorrelation signals will appear on the  $I_{ac}$  graph. Commercial silicon wafers, polished on both sides, provide typically autocorrelation signals with respect to substrate thickness on the coherent interferogram. This is why the reference mirror can be removed. The inverse Fourier transform (inverse-FT) of the spectral interferogram without a reference mirror can provide interferograms owing to the DC and autocorrelation terms, and the FD-LCI without the fixed reference mirror is of the autocorrelation-type (ACT).

### 2.2.2 Principle of temperature measurement

The temperature of the Si substrate is derived from the change in the optical path length due to thermal expansion and changes in the refractive index induced by changes in temperature. The optical-path length  $L$  of a certain substrate is

## Chapter 2

$$L = n(T, \lambda)d(T), \quad (2.9)$$

where  $n$  is the refractive index and  $d$  is the thickness of the substrate. When the temperature of the substance changes from  $T$  to  $T + \Delta T$ , the refractive index and the thickness changes as follows:

$$d(T) \rightarrow d(T)(1 + \alpha(T)\Delta T), \quad (2.10)$$

$$n(T, \lambda) \rightarrow n(T, \lambda)(1 + \beta(T, \lambda)\Delta T), \quad (2.11)$$

where  $\alpha$  is the thermal expansion and  $\beta$  is the temperature coefficient of the refractive index, respectively.  $\alpha$  is dependent on temperature. On the other hand,  $\beta$  has the function of wavelength and temperature. The optical path length  $L'$  of the substrate at the temperature  $T + \Delta T$  is expressed as below,

$$L' = n(T, \lambda) \cdot d(T) \{1 + (\alpha(T) + \beta(T, \lambda))\Delta T\}. \quad (2.12)$$

The change in the optical path length  $\Delta L$  is described by

$$\Delta L = L' - L \cong n(T, \lambda) \cdot d(T) (\alpha(T) + \beta(T, \lambda)) \Delta T. \quad (2.13)$$

Hence, the variation in the optical path length in a Si substrate due to the temperature change of the substrate depends both on thermal expansion and the temperature coefficient of refractive index. Substrate temperature can be estimated from the optical path length in the substrate, when the length at room temperature and its temperature dependence are known [3].

### 2.3 Temporal variation of substrate temperature

The model of temporal variation of the substrate temperature is described in detail by many researchers [4-9]. The model is derived from the heat balance of the substrate-heating and substrate-cooling environment. The model considers the substrate heating by the plasma and the heat losses by the radiative and cooling system. The energy balancing at the substrate is given by

$$\dot{Q}_{\text{IN}} = \frac{dH_{\text{W}}}{dt} + \dot{Q}_{\text{OUT}}, \quad (2.14)$$

where  $\dot{Q}_{\text{IN}}$  is the power flux in ( $\text{J S}^{-1}$ ),  $\dot{Q}_{\text{OUT}}$  is the power flux out ( $\text{J S}^{-1}$ ) and  $H_{\text{w}}$  is the enthalpy of the substrate (J).

$$\dot{Q}_{\text{IN}} = \rho c_p dA \frac{dT_{\text{W}}}{dt} + k_1 A (T_{\text{W}} - T_{\text{H}}) + k_2 A (T_{\text{W}}^4 - T_{\text{U}}^4), \quad (2.15)$$

where  $\rho$  is the density ( $\text{kg m}^{-3}$ ),  $c_p$  is the heat capacity ( $\text{J kg}^{-1} \text{K}^{-1}$ ),  $d$  is the thickness of the substrate (m),  $A$  is the area of the substrate ( $\text{m}^2$ ),  $T_{\text{W}}$  is the substrate temperature (K),  $T_{\text{H}}$  is the substrate holder temperature (K),  $T_{\text{U}}$  is the temperature of the environment (K),  $t$  is the time (s),  $k_0 = \rho c_p d$  ( $\text{J m}^{-2} \text{K}^{-1}$ ),  $k_1$  is the conduction coefficient ( $\text{W m}^{-2} \text{K}^{-1}$ ) and  $k_2$  is the radiation coefficient ( $\text{W m}^{-2} \text{K}^{-4}$ ). The radiation coefficient is expressed as  $2\epsilon\sigma$ .  $\epsilon$  is the spectral emittance.  $\sigma$  is the Stefan-Boltzmann constant. The factor of 2 results from the assumption of having a radiating area of twice the substrate. The first term on the right-hand side of Eq. (2.15) describes the heating of the substrate and is the energy stored in the whole substrate. In the case of a Si wafer, the average temperature of the substrate is assumed to be equal to the surface temperature, since the heat conductivity of the silicon wafer is high. The second term describes the heat flux transferred conductively from the substrate by gas and radiation along the sample holder. The third term one describes the radiative losses. In a common low-temperature plasma, the contribution of radiative losses is small. The differential Eq. (2.15) is solved as follows:

$$k_0 \frac{dT_W}{dt} = \frac{\dot{Q}_{IN}}{A} - k_1(T_W - T_H). \quad (2.16)$$

By separation of variables Eq. (2.16) is solved as

$$\int_0^{T_W - T_H} \frac{d(T_W - T_H)}{k_1(T_W - T_H) - \dot{Q}_{IN}/A} = - \int_0^t \frac{dt}{k_0}. \quad (2.17)$$

Solution of (2.17) gives

$$\ln \left| \frac{k_1(T_W - T_H) - \dot{Q}_{IN}/A}{-\dot{Q}_{IN}/A} \right| = - \frac{tk_1}{k_0}, \quad (2.18)$$

$$T_W = T_H + \frac{\dot{Q}_{IN}/A}{k_1} \left[ 1 - \exp\left(-\frac{tk_1}{k_0}\right) \right]. \quad (2.19)$$

The temperature difference between the beginning and the end of processes is proportional to the heat flux from the plasma, and is inversely proportional to the conduction coefficient. The temperature difference is a source of complexity to comprehend the temperature dependence of plasma processes.

## 2.4 Scanning electron microscopy (SEM)

Scanning electron microscopy (SEM), which is one of the electron microscopies, images the sample surface by incidence of electron accelerated in fast scan. Due to high resolution, SEM is the powerful tool for analysis the topography of samples in nanoscience and nanotechnology due to obtaining a high-resolution image.

In 1935, Max Knoll has reported the first SEM image of silicon steel showing electron channeling contrast [10]. Moreover, Charles Oatley has made an improvement in the first SEM instrument in 1965. An electron microscope uses a beam of electrons to enlarge an image of the sample. In SEM, the image is produced by obtaining a secondary electron emitted from the sample [11]. A schematic of optical and electrical system in the SEM is shown in Fig. 2.2. It consists of electron gun, condenser lens, scanning coil, objective lens, electron detector, etc. Electrons emitted from an electron gun pass through lenses to be focused on and scanned across the sample. The electron beam should be bright with small energy spread. Display unit consist of CRT (Cathode Ray Tube), deflection coils, scanning circuits, signal amplifier, etc. Magnification,  $M$ , results from the mapping process according to the ratio of the dimension scanned on the CRT to the dimension of the scanned sample  $M = (\text{Length of CRT display}) / (\text{Length of sample scan})$ . The electron energy is generally from 1 to 30 keV for most semiconductor sample. The use of high-energy electrons has an advantage over optical microscopes; larger magnifications are obtained since electron wavelength are smaller (that is 0.4 nm in case of the commercial model; Hitachi, S-5200) compared to photon wavelength and the depth of focus is higher. In this study, the electron energy is set to be relatively low energy 5 keV, preventing the organic film used as etched samples from the deformation and the charge up by electron bombardment. To reduce the charge up of it, its surface was coating by sputter-deposited gold film.

In 1923, De Broglie has proposed that particles can be regarded as waves [12].

## Chapter 2

The electron wavelength  $\lambda_e$  is expressed as a function of the electron velocity  $v$  or the accelerating voltage  $V$ ,

$$\lambda_e = \frac{h}{mv} = \frac{h}{\sqrt{2qmV}} = \frac{1.22}{\sqrt{V}} [nm]. \quad (2.20)$$

From Eq. (2.20), the electron wavelength at 1 kV is estimated at 0.012 nm. The value is a wavelength significantly below the 400 to 700 nm wavelength of visible light. Hence, the use of the electron microscopy produces the high-resolution image compared to that of an optical microscope.

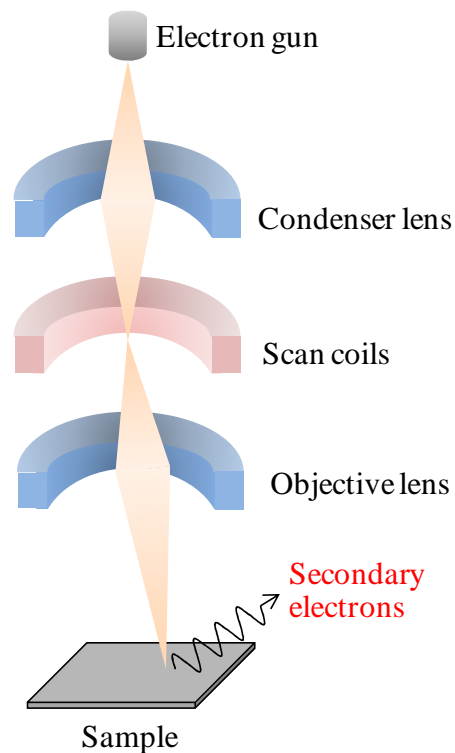


Fig. 2.2. Schematic diagram of electron beam area in SEM system.

## 2.5 References

- [1] W. Drexler and J. G. Fujimoto, *Optical Coherence Tomography—Technology and Applications* (Springer, Berlin, 2008) pp. 53–55.
- [2] T. Hiraoka, T. Ohta, T. Kageyama, M. Ito, N. Nishizawa, and M. Hori, *Jpn. J. Appl. Phys. Part 1* **52**, 026602 (2013).
- [3] K. Takeda, Y. Tomekawa, T. Shiina, M. Ito, Y. Okamura, and N. Ishii, *Jpn. J. Appl. Phys.* **43**, 7737 (2004).
- [4] R. A. Bond, S. Dzioba, and H. M. Naguib, *J. Vac. Sci. Technol.* **18**, 335 (1981).
- [5] P. Parry, *J. Vacuum Sci. Technol.* **13**, 622 (1976).
- [6] I. Hussla, K. Enke, H. Grünwald, G. Lorenz, and H. Stoll, *J. Phys. D* **20**, 889 (1987).
- [7] H. Kersten and G. M. W. Kroesen, *J. Vac. Sci. Technol. A* **8**, 38 (1990).
- [8] R. Rochotzki and M. Friedrich, *IEEE Proc. A* **139**, 61 (1992).
- [9] K. Takaki, A. Takahashi, and T. Fujiwara, *Jpn. J. Appl. Phys.* **37**, 3514 (1998).
- [10] M. Knoll, *Zeitschrift für technische Physik* **16**, 467 (1935).
- [11] P. Sigmund, *Phys. Rev.* **184**, 383 (1969).
- [12] D. K. Schroder, *Semiconductor Materials and Device Characterization Third Edition*, (Wiley, New York, 2006).

## Chapter 2

## **Chapter 3 Development of frequency-domain low-coherence interferometry for measuring semiconductor-substrate temperature**

### **3.1 Introduction**

Many methods of measuring substrate temperature during plasma processing have been proposed [1-4]. For conventional contact-type temperature sensors such as thermocouples and fluorescence thermometers, it is necessary to make the sensing position to the backside surface of wafer substrate. The thermal conductance between the wafer and probe easily affects the measurement accuracy. Particularly at low pressures, poor contact often results in less accurate measurement, that is, it is difficult for those conventional systems to measure substrate temperatures with high accuracy during plasma processing [5]. Noncontact methods enable a more accurate substrate temperature measurement. However, pyrometers could not be used to measure the temperature of silicon wafers, because the thermal radiation depends on the temperature and its variation is too small to detect especially at temperatures below 600°C [6]. Other noncontact methods using an optical interferometer with an infrared laser were proposed [7-13]. These noncontact optical techniques determine temperature changes from the thermal expansion and the refractive index changes of a transparent substrate of known thickness. However, there remain difficulties such as their poor tolerance to mechanical disturbances, resulting in limited resolution and temperature ranges when monitoring Si wafers.

In the system that monitors substrate temperature by frequency-domain low-coherence interferometry (FD-LCI) the author developed, temperature is measured from the shifts in the optical path length of the substrate due to the temperature shifts. The conventional FD-LCI system has a potential for high-sensitivity measurement in the millisecond time scale [14-19]. In conventional FD-LCI using a dual-path

## Chapter 3

interferometer, however, the compensations for the dispersion and the polarization differences between the reference and sample lights are required in measuring the optical path length of the substrate with accuracy [20-21]. The high parallelism of the semiconductor substrate enables the removal of a reference mirror from the interferometry in FD-LCI. Hence, he developed an autocorrelation-type frequency-domain low-coherence interferometry (ACT-FD-LCI) system, which can measure substrate temperature with a common path interferometry, by removing the reference mirror [22].

In this chapter, the robust characteristics of the ACT-FD-LCI system were investigated. In particular, he examined its precisions and the effects of the dispersion and polarization differences on ACT-FD-LCI using the common path and conventional FD-LCI using the dual path by varying the polarization of the signal arm. Moreover, the dependences of center wavelength of the light source on accuracy and temperature range of ACT-FD-LCI were investigated.

## 3.2 Experimental details

The fiber-base FD-LCI system for measuring the substrate temperature is shown in Fig. 3.1. A superluminescent diode (SLD: a central wavelength, 1.31  $\mu\text{m}$ ; full width at half maximum, 50 nm) was used as a low-coherence light source. The fiber optical circulator prevents fluctuation spectrum of the SLD due to incidence from the reference arm and the sample arm. The fiber coupler split the light of the SLD with 50/50 splitting ratio. The difference in optical distance between the reference arm and the sample arm was set at 2.0 mm by arranging the reference mirror. A 480- $\mu\text{m}$ -thick Si wafer was placed in a blackbody furnace to accurately control its temperature, which was measured using thermocouples placed on the surface of the Si wafer. The accuracy of the temperature measurement depended on calibration with temperatures measured using thermocouples. The spectral interferograms was observed using the array detector, which was a Hamamatsu linear image sensor with 1024 horizontal pixels. The maximum line scan rate was 39000 scans per second, which corresponded to the time resolution of 26  $\mu\text{s}$ . This indicates that the FD-LCI system can be applied to rapid thermal processing. As described above, in the case of ACT-FD-LCI, the optical path length of a substrate was deduced from the interference of sample arm signals. Hence, the optical path lengths of the Si wafer were measured by blocking out the light of the reference arm.

To discuss the dependence of a center wavelength of a light source on the accuracy and the temperature range of ACT-FD-LCI in Section 3.4.3, the optical path lengths of the 480- $\mu\text{m}$ -thick Si wafer were measured with three light sources that have different center wavelengths. Table 3.1 shows specifications detail of their light sources. The coherence lengths shown in Table 3.1 were determined from Eq. (2.8). All spectrum interferograms of the 480- $\mu\text{m}$ -thick Si wafer, which were depended on the center wavelength of the light source, were observed by an optical spectrum analyzer (Anritsu MS9740A).

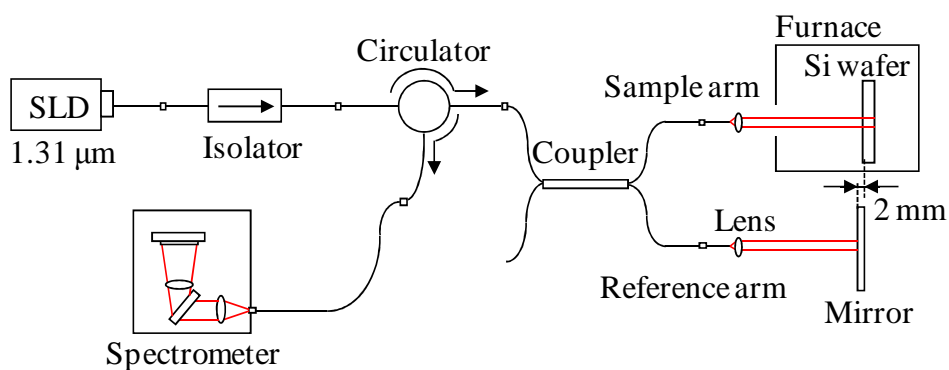


Fig. 3.1 Fiber-optic frequency-domain low-coherence interferometer for temperature measurement. Here, SLD is the superluminescent diode.

Table 3.1 Specifications of light sources used in ACT-FD-LCI.

	Center wavelength [nm]	FWHM [nm]	Coherence length [ $\mu\text{m}$ ]
OPTOENERGY A40102230M7	1040	27.5	17.8
COVEGA SLD-7005	1310	40.6	19.0
COVEGA SLED-346	1550	50.9	21.2

### 3.3 Results and discussion

#### 3.3.1 Measurements of optical path length change and temperature

Each spectral interferogram of the 480- $\mu\text{m}$ -thick Si wafer by conventional FD-LCI and ACT-FD-LCI was observed as shown in Fig. 3.2. Figure 3.2(a) shows a spectral interferogram obtained by FD-LCI at room temperature. Sinusoidal changes appear in the spectral interferogram signal that corresponds to the interferogram containing the terms of DC, cross-correlation, and autocorrelation. From Eq. (2.2), the spectral interferogram obtained by FD-LCI contains the cosine function of the variable  $(z_R - z_n)$  in the cross-correlation term.  $(z_R - z_1)$  and  $(z_R - z_2)$  are the optical difference between the reference arm and the front surface of the Si wafer, and that between the reference arm and the back surface of the Si wafer, respectively. Under this experimental condition,  $(z_R - z_1)$  corresponds to 2.0 mm, which was the difference in optical distance between the reference and sample arms.  $(z_R - z_2)$ , which was the sum of 2.0 mm and the optical path length of the 480- $\mu\text{m}$ -thick Si wafer, was 3.7 mm. The pitches of the cosine function were about 0.429 and 0.234 nm, respectively. A spectrometer whose wavelength resolution was 0.074 nm satisfied these pitches. Considering multiple reflections from the Si wafer, the spectrometer can detect multiple reflections. From Eq. (2.3), the spectral interferogram obtained by FD-LCI also contains the cosine function of the variable  $(z_1 - z_2)$  in the autocorrelation term.  $(z_1 - z_2)$  is the optical path length of the Si wafer. The pitch was equivalent to 0.514 nm. The pitch of the interference term between a reflection from the front surface of the Si wafer and the second reflection from the back surface of the Si wafer was 0.257 nm. The pitch of the interference term between a reflection from the front surface of the Si wafer and the third reflection from the back surface of the Si wafer was 0.172 nm. The spectrometer can detect the interference signals from two reflections. Hence, the spectral interferogram obtained by FD-LDI contained three terms in cross-correlation and three terms in autocorrelation.

Figure 3.2(b) shows a spectral interferogram obtained by ACT-FD-LCI at room temperature. Compared with the spectral interferogram obtained by conventional FD-LCI, that obtained by ACT-FD-LCI has a simpler shape and is similar to Gaussian interferograms. It is composed of DC and a cosine function of the variable  $(z_1 - z_2)$  in autocorrelation terms owing to the removal of the reference mirror.

Figure 3.3 shows a time-domain interferogram obtained by FD-LCI through the inverse Fourier transform of the spectral interferograms shown in Fig. 3.2(a) and 3.2(b). Figure 3.3(a) shows plots of typical DC and cross-correlation and autocorrelation peaks. These peak positions are in agreement with the theory described above. The cross-correlation peaks arise from the interference between the light reflected from the mirror and that reflected from the front and the back surfaces of the wafer. The twofold difference in optical distance between the reference and the sample arm gives a value of approximately 4.0 mm. Adding this difference in optical distance and the twofold optical path length of the wafer gives a value of approximately 7.3 mm. Moreover, considering multiple reflections from the Si wafer, the cross-correlation peaks appear at 10.6 mm. The autocorrelation peaks arise from the interference between the lights reflected from the front and back surfaces of the wafer. The twofold optical path length of the wafer gives a value of approximately 3.3 mm. Owing to multiple reflections from the Si wafer, the autocorrelation peaks appear at 6.6 and 10.0 mm.

Figure 3.3(b) shows a time-domain interferogram obtained by ACT-FD-LCI. Figure 3.3(b) shows plots of only the DC and autocorrelation peaks because the reference mirror was removed from the low-coherence interferometry. Hence, the interferogram obtained by ACT-FD-LCI shows elimination of cross-correlation peaks observed in Fig. 3.3(a).

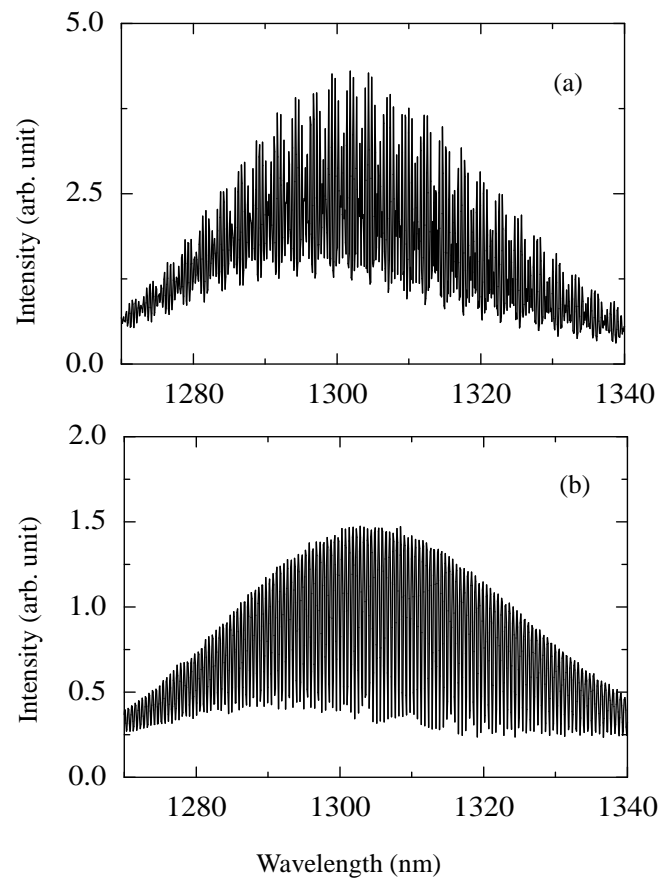


Fig. 3.2 Spectral interferograms. (a) conventional FD-LCI and (b) ACT-FD-LCI using the SLD (a central wavelength, 1.31  $\mu\text{m}$ ; full width at half maximum, 50 nm).

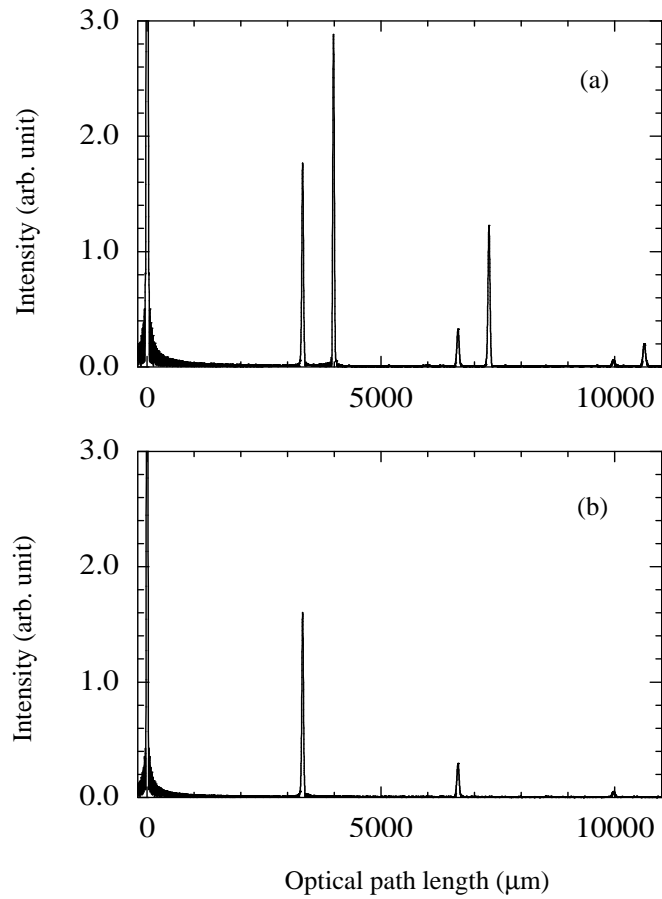


Fig. 3.3 Cross-correlation and autocorrelation spectrums obtained by inverse Fourier transforms of the spectral interferograms shown in Fig. 3.2.

Figure 3.4 shows a graph of the optical path lengths measured by FD-LCI and ACT-FD-LCI as a function of the temperature of the Si wafer in the blackbody furnace. This figure indicates that the same optical path lengths of the wafer depending on temperature were obtained using both methods. The relationship between the temperature of the Si wafer (480  $\mu\text{m}$ ) and the optical path length derived by ACT-FD-LCI is described as

$$T = -4.4 \times 10^{-3} L^2 + 3.3 \times 10 L - 6.1 \times 10^4, \quad (3.1)$$

where  $T$  ( $^{\circ}\text{C}$ ) and  $L$  ( $\mu\text{m}$ ) are the temperature and optical path length, respectively. He can measure the temperature of Si wafers in real time by using this equation. Figure 3.5 shows the standard deviations of 20 measurements at each temperature in the range from 20 to about  $600^{\circ}\text{C}$ . The standard deviations of temperature measurements by ACT-FD-LCI were less than  $0.04^{\circ}\text{C}$  at temperatures below  $550^{\circ}\text{C}$ . This performance shows a substantial improvement compared with the precision of  $0.28^{\circ}\text{C}$  obtained using conventional FD-LCI. Taking into consideration its applications to other semiconductor substrates, which have a lower refractive index and shows smaller changes in optical length with temperature than Si, the improved precision of ACT-FD-LCI is advantageous for general purpose. As the temperature increases above  $550^{\circ}\text{C}$ , however, the standard deviation increases exponentially. The autocorrelation peaks were not obtained at temperatures above  $650^{\circ}\text{C}$ , which is due to the increase in the absorption coefficient of the Si wafer with increasing temperature [23]. The result indicates that ACT-FD-LCI using SLD with a wavelength of  $1.31 \mu\text{m}$  is difficult for measuring slight thermal changes at temperatures above  $550^{\circ}\text{C}$  in a  $480\text{-}\mu\text{m}$ -thick Si wafer, and the utility of this technique strongly depends on the absorption coefficient of a sample. By employing SLD with longer wavelengths, the deterioration would be improved even at much higher temperatures.

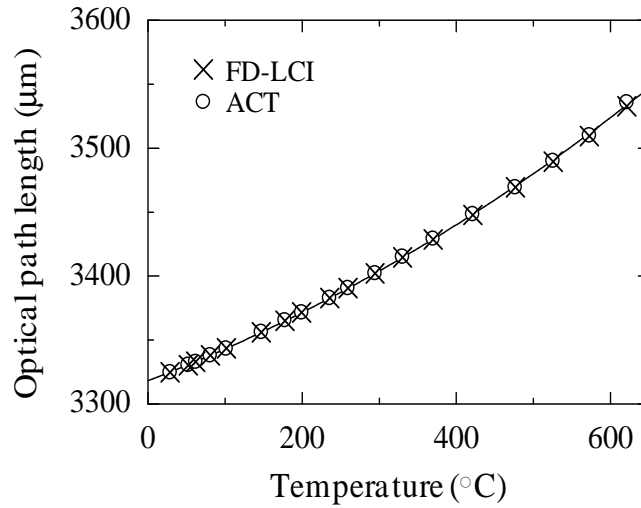


Fig. 3.4 Variation in optical path length with temperature for a 480- $\mu\text{m}$ -thick Si wafer inside a blackbody furnace determined by FD-LCI and ACT-FD-LCI using the SLD (a central wavelength, 1.31  $\mu\text{m}$ ; full width at half maximum, 50 nm).

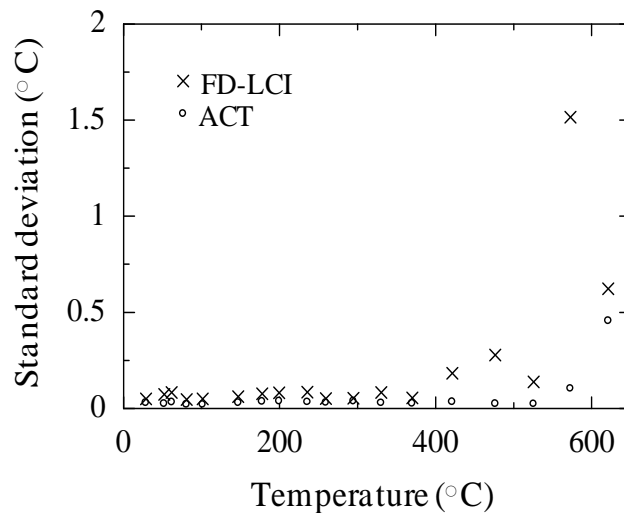


Fig. 3.5 Standard deviation of temperatures measured by FD-LCI and ACT-FD-LCI as a function of furnace temperature using the SLD (a central wavelength, 1.31  $\mu\text{m}$ ; full width at half maximum, 50 nm).

The response speed of an ACT-FD-LCI is demonstrated by temperature measurements of a Si wafer being rapidly thermally annealed by halogen-lamp irradiation of its back surface. For reference, a thermocouple is in contact with the front surface of the wafer. Figure 3.6 plots the time evolution of the temperature (at a resolution of 1 ms) measured using both the ACT-FD-LCI and the thermocouple. The results indicate that the ACT-FD-LCI measures the wafer temperature at a rate of  $5.74^{\circ}\text{C/s}$ . In contrast, the thermocouple does not correctly measure the wafer temperature, reporting an erroneous heating rate of  $3.81^{\circ}\text{C/s}$  with a time delay exceeding 0.1 s. This failure arises from poor thermal contact between the Si wafer and the thermocouple.

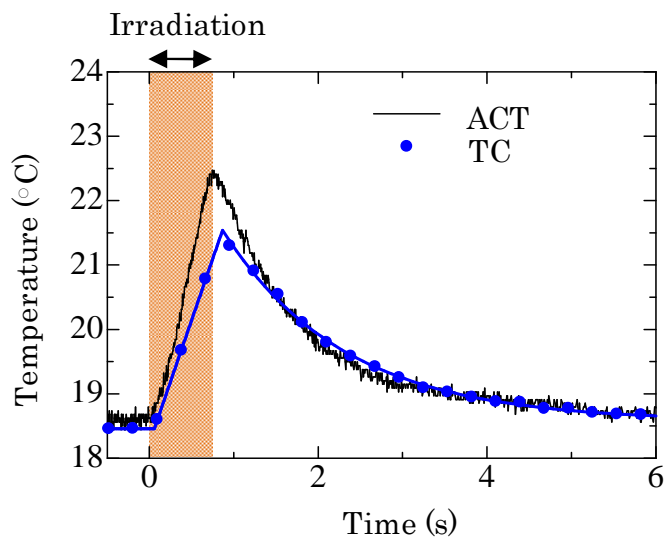


Fig. 3.6 Real-time monitoring of the temperature of a Si wafer during irradiation by a halogen lamp.

### 3.3.2 Effects of dispersion and polarization on optical path length

In the case of a dual-path interferometer such as the conventional FD-LCI systems, the dispersion and the polarization differences between the reference and sample lights affect the interferences. The coherence length  $l_c$  described above is the FWHM of the cross-correlation or cross-correlation peak and strongly depends on the dispersion. In the case of FD-LCI using a dual-path interferometer, the FWHM of the cross-correlation peak at 7.3 mm in Fig. 3.3(a), which is the interference between the reference light and the light reflected on the back surface of the Si wafer, was 49  $\mu\text{m}$ . On the other hand, for ACT-FD-LCI using a common-path interferometer, the FWHM of the autocorrelation peak at 3.3 mm, which is the interference between the front and back surfaces of the wafer, was 41  $\mu\text{m}$ . Because the measurement accuracy for substrate temperature is related to the FWHM of the correlation peak, the measurement accuracy is improved by ACT-FD-LCI with a smaller FWHM than FD-LCI [24].

By varying the polarization of the signal arm using a polarization controller, I have investigated the effects of the polarization differences between FD-LCI using a dual-path interferometer and ACT-FD-LCI using a common-path interferometer. In the case of FD-LCI, the peak intensity of cross-correlation decreased by 78% and the standard deviation of optical path length worsened from 15 to 46 nm. On the other hand, in ACT-FD-LCI, the peak intensity decreased only by 5% and the standard deviation of optical path length was nearly the same, from 12 to 10 nm.

Measurement errors of the ACT-FD-LCI were mainly caused by imperfect optics. Actually, the use of a common-path interferometer has high robustness against fiber-induced dispersion, polarization mismatch, and polarization changes due to mechanical vibration. Consequently, ACT-FD-LC is more stable and reliable than conventional FD-LCI.

### 3.3.3 Relations between the center wavelength of light sources and measurement characteristic

The temperature of a Si wafer can be estimated from the change in an optical path length by using ACT-FD-LCI. The optical path length of the substrate is expressed as a product of a refractive index and a thickness. The refractive index  $n$  and the coefficient of the temperature dependence of the refractive index  $\beta$  depend on a wavelength of a light source in an interferometry. Figure 3.5 showed that increasing the absorption coefficient with increasing the substrate temperature reduced the accuracy of measurement. The absorption coefficient of the Si wafer also depends on the wavelength of the light source. These indicate that the wavelength of the light source is the important factor in determining the accuracy and the temperature measuring range of ACT-FD-LCI.

In this section, the optical path length of the 480- $\mu\text{m}$ -thick Si wafer has been measured at three different wavelengths, which are 1040 nm, 1310 nm, and 1550 nm, by using ACT-FD-LCI. Spectral interferograms obtained by the optical spectrum analyzer were shown in Fig. 3.7. The spectrum interferogram at 1550 nm (Fig. 3.7(c)) contained a high proportion of the autocorrelation term relatively. The intensity of the autocorrelation term was expressed in Eq. (2.3). The peak intensity is obtained for a product of  $R_1$  and  $R_2$ . The effective reflectivity at each wavelength was derived from Fresnel coefficient. The effective reflectivities at a front and a back surface of a substrate are given by

$$R_1(\lambda) = |\rho_0|^2 = \left| \frac{n_0 - n_1(\lambda)}{n_0 + n_1(\lambda)} \right|^2, \quad (3.2)$$

$$R_2(\lambda) = |\tau_0 \tau_1 \rho_0 \exp(-i\delta)|^2 = \left| \frac{4n_0 n_1(\lambda)(n_0 - n_1(\lambda))}{(n_0 + n_1(\lambda))^3} \right|^2, \quad (3.3)$$

where  $n_0$  and  $n_1(\lambda)$  are the refractive indexes of air and Si wafer, respectively.  $\rho_0$  is the amplitude reflection coefficient at the air/Si interface,  $\tau_0$  is the amplitude transmission

coefficient at the air/Si interface,  $\tau_1$  is the amplitude transmission coefficient at the Si/air interface,  $\delta$  is the phase difference between the light reflected at air/Si interface and the light reflected at the Si/air interface. The refractive indexes of a Si at room temperature (25°C) were estimated using the Cauchy dispersion formula as follows:

$$n_1(\lambda) = 3.484 + \frac{6.381 \times 10^{-14}}{\lambda^2} + \frac{5.638 \times 10^{-26}}{\lambda^4}. \quad (3.4)$$

Factors of Eq. (3.4) were calculated from the refractive index and wavelength [12]. From Eqs. (2.1), (2.2), (2.3), (3.2), (3.3), and (3.4), the ratios of the autocorrelation's peak intensity to DC's that in spectrum interferograms were 0.47 at all wavelengths. This indicated that the dependence of the wavelength on the spectrum interferogram did not cause containing the high proportion of the autocorrelation term at 1550 nm. Possible explanations are following. (1) The signal light reflected off the back surface of the substrate was not focused at precise position of optical fiber through the lens. (2) Noise signals appeared as the autocorrelation term due to a multiple reflection at an interface between optical devices.

Figure 3.8 shows time-domain interferences obtained by inverse Fourier transform of the spectral interferograms shown in Fig. 3.7. The DC and autocorrelation terms were obtained in all time-domain interferences. Intensities of the time-domain interferences were normalized so that the DC's peak intensities in all time-domain interferences are equal. The interferences around 3500  $\mu\text{m}$  show autocorrelation terms between the front and back surface of the Si wafer. From Eq. (2.6), the peak position of autocorrelation terms corresponds to the optical path length of a substrate. The longer wavelength a light source has, the shorter the optical path length of Si wafer become. This is because the optical length is obtained for the product of the refractive index and the thickness. Estimated from Eq. (3.4), the refractive index of Si wafer at 1040 nm, 1310 nm, and 1550 nm are 3.59, 3.54, and 3.52, respectively. The interferences around 3500  $\mu\text{m}$  at 1550 nm obtained maximum intensity. Moreover, noise signals appeared

## Chapter 3

around DC signal in time-domain interference at 1550 nm. These results caused that the spectrum interferogram at 1550 nm contained the high proportion of the autocorrelation terms.

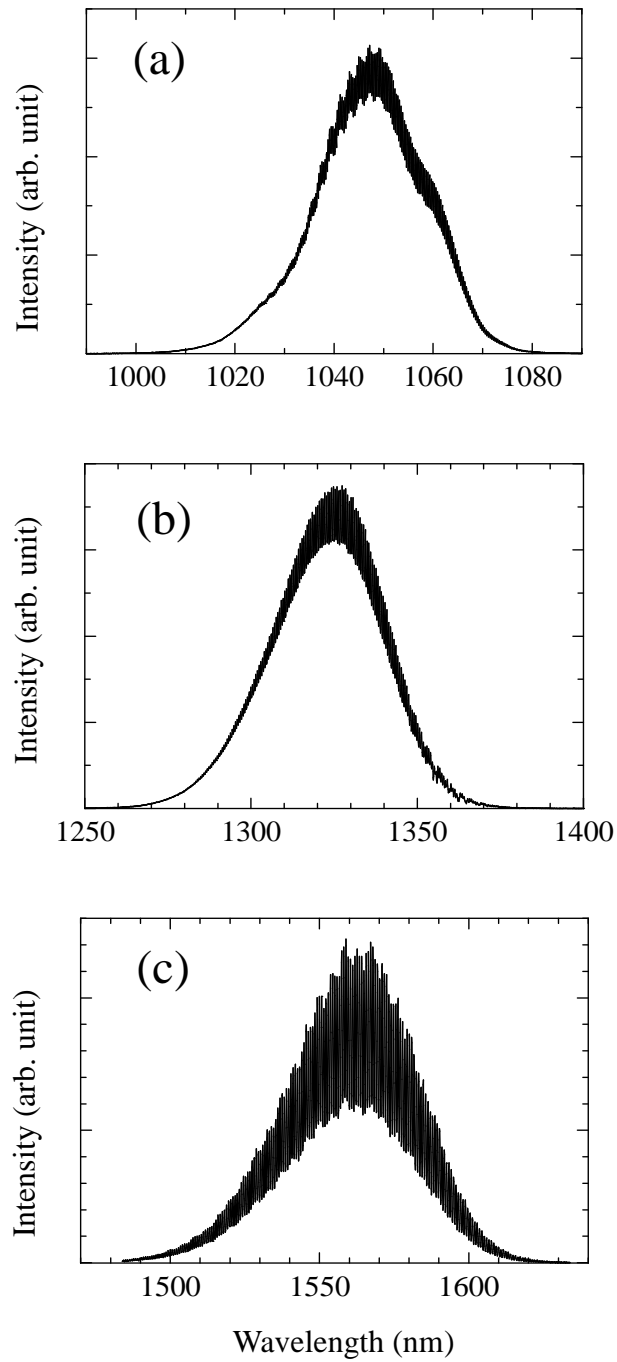


Fig. 3.7 Spectral interferograms of 480- $\mu\text{m}$ -thick Si wafer at (a) 1040 nm, (b) 1310 nm, and (c) 1550 nm using SLDs shown in Table 3.1.

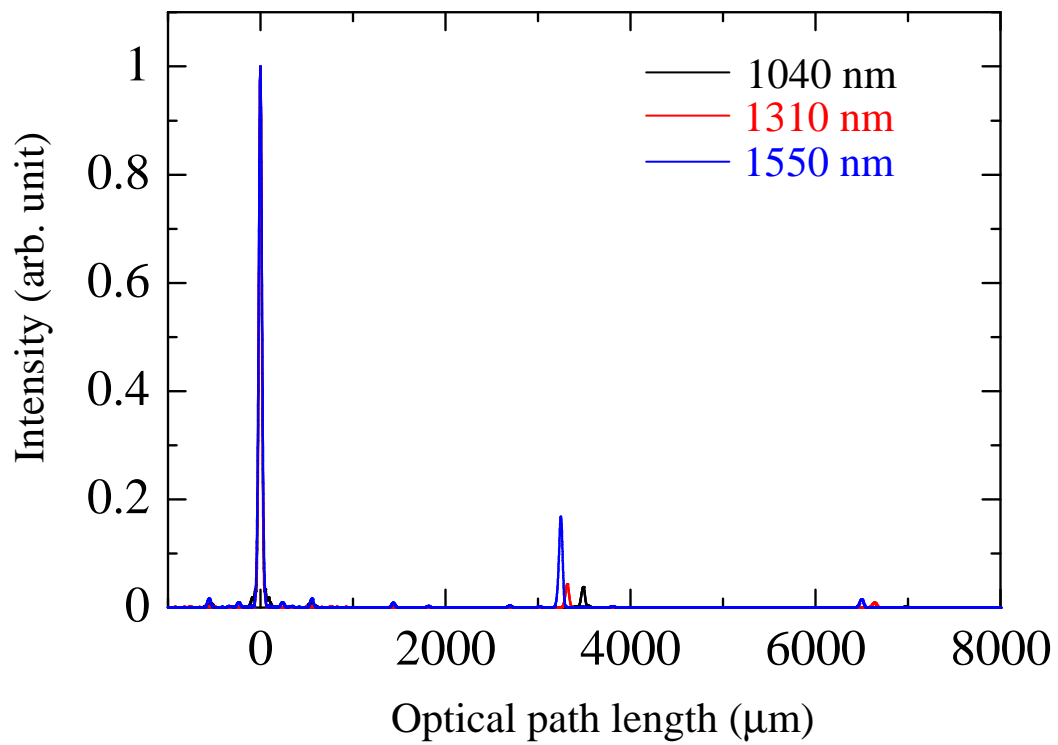


Fig. 3.8 Time-domain interferences obtained by inverse Fourier transforms of the spectral interferograms shown in Fig. 3.7.

## Chapter 3

Figure 3.9 shows a graph of the optical path lengths measured at all wavelengths as function of the temperature of the Si wafer in the blackbody furnace. This result indicated the dependence of the wavelength on the refractive index and the optical path length of the Si wafer. In the case of 1040 nm, the optical path length was not obtained over 120°C because of decreasing the intensity of the autocorrelation term. Figure 3.10 shows the peak intensities of the autocorrelation terms at all wavelengths as function of the temperature. The peak intensity at 1040 nm decreased exponentially due to increasing the absorption coefficient of Si at 1040 nm with temperature [24]. In Fig. 3.5, the peak intensity at 1310 nm was not observed at temperatures above 650°C. In the case of 1550 nm, these results expect an upper limit detection of the temperature to rise due to the lower absorption coefficient of the 480- $\mu\text{m}$ -thick Si wafer. The important factor in determining the temperature range of measurement is not only the absorption coefficient, but also the thickness of the wafer.

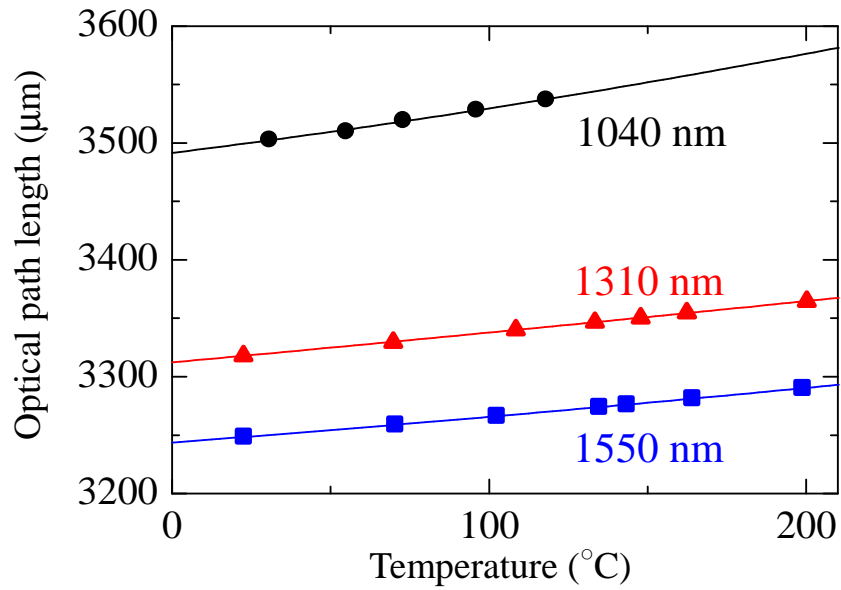


Fig. 3.9 Variation in the optical path length of 480- $\mu\text{m}$ -thick Si wafer with temperature at 1040 nm, 1310 nm, and 1550 nm.

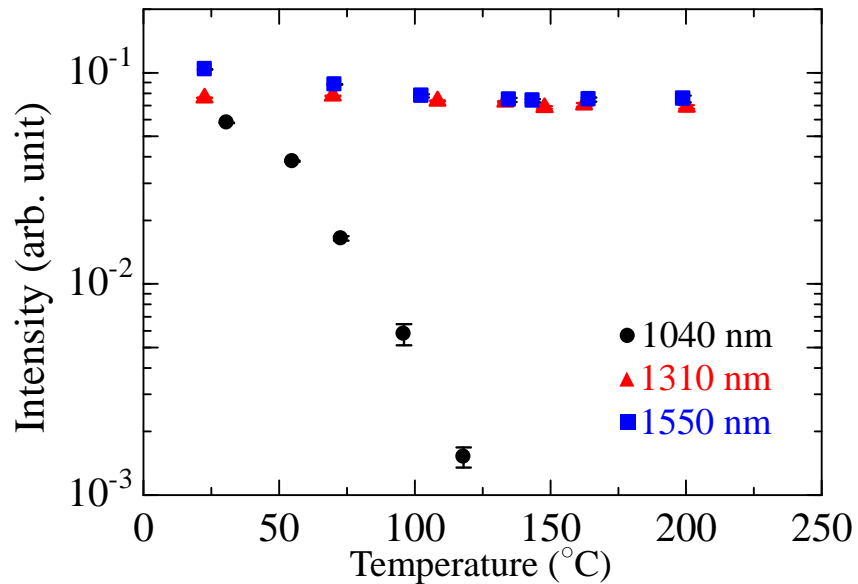


Fig. 3.10 Peak intensities of autocorrelation terms as a function of temperature at 1040 nm, 1310 nm, and 1550 nm.

The changing of optical path lengths as function of the temperature of the Si wafer are shown in Fig. 3.11 and given by

$$\Delta L_{1040}(T) = 4.31 \times 10^{-4} \Delta T^2 + 3.37 \times 10^{-1} \Delta T + 6.38 \times 10^{-2}, \quad (3.5)$$

$$\Delta L_{1310}(T) = 6.80 \times 10^{-5} \Delta T^2 + 2.48 \times 10^{-1} \Delta T - 1.32 \times 10^{-2}, \quad (3.6)$$

$$\Delta L_{1550}(T) = 1.39 \times 10^{-4} \Delta T^2 + 2.06 \times 10^{-1} \Delta T - 2.80 \times 10^{-3}, \quad (3.7)$$

where  $\Delta T$  ( $^{\circ}\text{C}$ ) and  $\Delta L$  ( $\mu\text{m}$ ) are the changing of the temperature and the optical path length, respectively. As shown in Fig. 3.11, the change rates of optical path length at temperatures below  $100^{\circ}\text{C}$  were 398, 257, 223  $\text{nm}/^{\circ}\text{C}$ . The optical path length change was calculated by using Eq. (2.12) and the coefficient of linear thermal expansion  $\alpha$  and  $\beta$  of silicon investigated by McCaulley [25]. The calculated values were shown in Fig. 3.11. The measured optical path length showed more change than calculated values over all wavelengths. The possible cause is that the observed  $\beta$  were higher than  $\beta$  investigated by McCaulley.

The coefficients of the temperature dependence of the refractive index  $\beta$  of silicon at 1310 nm and 1550 nm were derived by using Eq. (2.12) and were shown in Fig. 3.12. The  $\beta$  investigated by McCaulley also are shown in Fig. 3.12 [25]. Since the  $\beta$  at lower wavelength shows the most change, this result gives validity of measurement by ACT-FD-LCI. However, the measured optical path length show more change than calculated that because the derived  $\beta$  were lower than the investigated  $\beta$ .

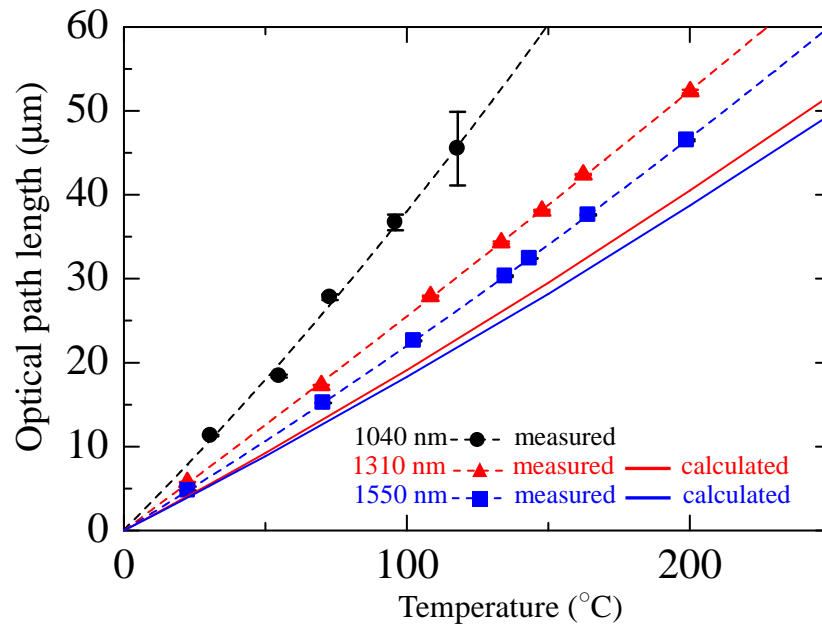


Fig. 3.11 The measured and calculated change of the optical path length of 480- $\mu\text{m}$ -thick Si wafer at 1040 nm, 1310 nm, and 1550 nm.

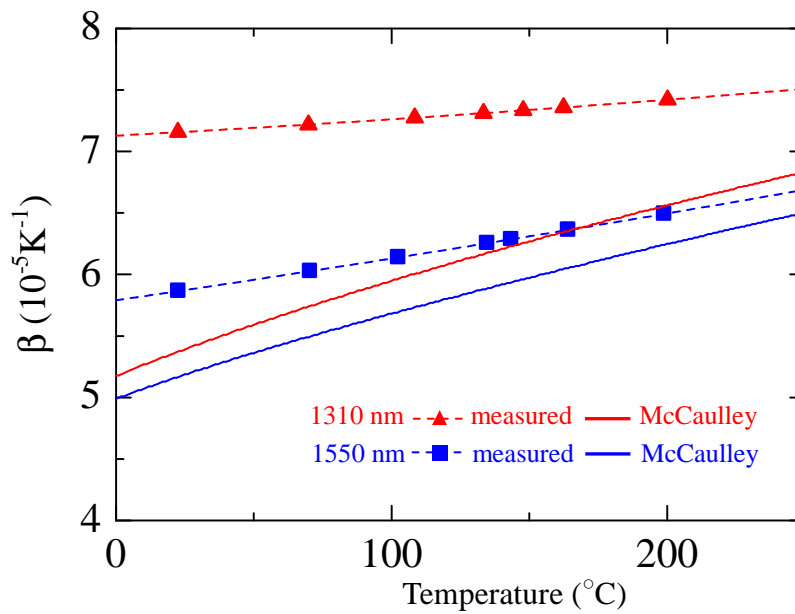


Fig. 3.12 The measured and calculated  $\beta$  of Si wafer as function of temperature at 1040 nm, 1310 nm, and 1550 nm.

## Chapter 3

These results confirmed that the ACT-FD-LCI using the light source with a wavelength of 1040 nm is not applied for the measurement of the 480-mm-thick Si wafer at temperatures over 120°C because of increasing the absorption coefficient of Si wafer with temperature. On the other hand, ACT-FD-LCI using light source with a wavelength of 1040 nm has the highest resolution of temperature because of the optical path length show the most change. Since the coherence length shown in Eq. (2.8) strongly depends on the center wavelength of the light source, the measurement accuracy is improved by ACT-FD-LCI using light source with a low center wavelength [24]. Since a semiconductor substrate has the low refractive index and low absorption coefficient, it is effective to use the light source with a low center wavelength.

### 3.4 Conclusion

The author has compared in detail an autocorrelation-type frequency-domain low-coherence interferometry (ACT-FD-LCI) system with the conventional frequency-domain low-coherence interferometry system. A high-precision rapid-response system for measuring the temperature of silicon wafers has been developed and demonstrated using a frequency-domain low-coherence interferometer (FD-LCI) employing autocorrelation signals without a reference mirror, in contrast to a conventional FD-LCI. The standard deviation of temperature measurement by ACT-FD-LCI was less than  $0.04^{\circ}\text{C}$  at temperatures below  $550^{\circ}\text{C}$  for a typical Si thickness of  $480\ \mu\text{m}$ , as determined from the measured optical path length. The performance has been improved, as compared with a precision of  $0.28^{\circ}\text{C}$  in the conventional FD-LCI. The results exhibit a high precision with a response time as short as 1 ms when monitoring the temperature of Si wafer.

He has discussed the dependence of center wavelength of the light source on accuracy and temperature range of ACT-FD-LCI. The optical path length of the  $480\text{-}\mu\text{m}$ -thick Si wafer was measured with three light sources that have different center wavelength, 1040 nm, 1330 nm, and 1550 nm. The absorption coefficient and the dependences of temperature on it influence on temperature range of measurement. They strongly depend on the center wavelength of light source. ACT-FD-LCI using light source with a wavelength of 1040 nm does not apply for measurement of the  $480\text{-}\mu\text{m}$ -thick Si wafer at temperatures over  $120^{\circ}\text{C}$  because of increasing the absorption coefficient of Si wafer with temperature. On the other hand, ACT-FD-LCI using light source with a lower wavelength has the higher resolution of temperature.

These results have confirmed that ACT-FD-LCI can successfully reduce the noise arising from mechanical vibrations, fiber-induced dispersion, and polarization mismatch. This technique is a robust and practically useful tool for measuring substrate temperature. In the case that a semiconductor substrate which has the low refractive

## Chapter 3

index and the low absorption coefficient, hence, it is an effective method to use the light source with a low center wavelength.

### 3.5 References

- [1] J. L. Booth, B. T. Beard, J. E. Stevens, M.G. Blain, and T. L. Meisenheime, *J. Vac. Sci. Technol. A* **14** , 2356 (1996).
- [2] J. L. Cui, K. Amtmann, J. Ristein, and L. Ley, *J. Appl. Phys.* **83**, 7929 (1998).
- [3] U. J. Gibson and M. Chernushenko, *Opt. Express* **4**, 443 (1999).
- [4] A. Cardoso and A. K. Srivastava, *J. Vac. Sci. Technol. B* **19**, 397 (2001).
- [5] K. Denpoh, *IEEE. Trans. Semicond. Manuf.* **11**, 25 (1998).
- [6] T. Sato, *Jpn. J. Appl. Phys.* **6**, 339 (1966).
- [7] V. M. Donnelly and J. A. McCaulley, *J. Vac. Sci. Technol. A* **8**, 84 (1990).
- [8] H. Sankur, *Appl. Phys. Lett.* **56**, 2651 (1990).
- [9] K. L. Saenger, *Rev. Sci. Instrum.* **63**, 3862 (1992).
- [10] J. Kikuchi, S. Fujimura, R. Kurosaki, and H. Yano, *J. Vac. Sci. Technol. A* **15**, 2035 (1997).
- [11] K. Takeda, Y. Tomekawa, T. Shiina, M. Ito, Y. Okamura, and N. Ishii, *Jpn. J. Appl. Phys.* **43**, 7737 (2004).
- [12] T. Ohta, C. Koshimizu, K. Kawasaki, K. Takeda, and M. Ito, *J. Appl. Phys.* **105**, 013110 (2009).
- [13] C. Koshimizu, T. Ohta, T. Matsudo, S. Tuchitani, and M. Ito, *Appl. Phys. Express* **3**, 056201 (2010).
- [14] A. F. Fercher, C. K. Hitzenberger, G. Kamp, and S. Y. El-zaiat, *Opt. Commun.* **117**, 43 (1995).
- [15] M. A. Choma, M. V. Sarunic, C. H. Yang, and J. A. Izatt, *Opt. Express* **11**, 2183 (2003).
- [16] J. F. de Boer, B. Cense, B. H. Park, M. C. Pierce, G. J. Tearney, and B. E. Boums, *Opt. Lett.* **28**, 2067 (2003).
- [17] R. Leitgeb, C. K. Hitzenberger, and A. F. Fercher, *Opt. Express* **11**, 889 (2003).
- [18] R. Huber, M. Wojtkowski, and J. G. Fujimoto, *Opt. Express* **14**, 3225 (2006).

- [19]W. Drexler and J. G. Fujimoto, *Optical Coherence Tomography—Technology and Applications* (Springer, Berlin, 2008) p. 53.
- [20]A. B. Vakhtin, D. J. Kane, W. R. Wood, and K. A. Peterson, *Appl. Opt.* **42**, 6953 (2003).
- [21]A. R. Tumlinson, J. K. Barton, B. Povazay, H. Sattman, A. Unterhuber, R. A. Leitgeb, and W. Drexler, *Opt. Express* **14**, 1878 (2006).
- [22]T. Tsutsumi, T. Ohta, K. Ishikawa, K. Takeda, H. Kondo, M. Sekine, M. Hori, and M. Ito, *Appl. Phys. Lett.* **103**, 182102 (2013).
- [23]H. A. Weakliem and D. Redfield, *J. Appl. Phys.* **50**, 1491 (1979).
- [24]T. Hiraoka, T. Ohta, T. Kageyama, M. Ito, N. Nishizawa, and M. Hori, *Jpn. J. Appl. Phys.* **52**, 026602 (2013).
- [25]J. A. McCaulley, V. M. Donnelly, M. Vernon, and I. Taha, *Phys. Rev. B* **49**, 7408 (1994).

## Chapter 3

## **Chapter 4 Measuring substrate temperature during plasma processes**

### **4.1 Introduction**

Plasma etching and plasma chemical vapor deposition (CVD) are important technologies for ultralarge-scale integrated circuits (ULSIs) fabrication. Process engineers have faced many complicated phenomena occurring during plasma processes. One is caused by the increased in the surface temperatures of the substrate and chamber parts. In plasma processes, the rise of wall temperature changes the radical densities of gaseous chemical species. The etch selectivity of oxide-to-nitride/silicon was reported to be enhanced by the temperature control [1-3]. The recombination rates of active species transported to the surface depend on the temperature [4-7].

To achieve a precise control in plasma processes, the substrate temperature must be controlled on the basis of accurate measurements [8]. Many methods of measuring substrate temperatures during plasma processes have been proposed [9-13]. It is difficult to measure substrate temperature with high accuracy because there remain difficulties such as their poor tolerance to mechanical disturbances, resulting in limited resolution and temperature ranges when monitoring silicon wafers. The author developed a noncontact measurement of substrate temperature using an autocorrelation type frequency-domain low-coherence interferometry (ACT-FD-LCI) system shown in Chapter 3. The temperature is measured from the shifts in the optical path length of the substrate due to temperature shifts [14-15]. The system has significant advantages of response and precision over other methods. To improve the quality and the etched features [8, 16-19], the plasma processes can be performed by monitoring and controlling the substrate temperature with the ACT-FD-LCI system. The heat balance of the substrate during the plasma process generally depends on the energy influx by bombardment and reaction of the electron, the ions, and the neutral species for a

## Chapter 4

common low-temperature plasma [20]. In order to comprehend the interaction between the plasma and the surface of the substrate, it is important to obtain the energy influx to the substrate during plasma processes.

In this chapter, a high-precision and rapid-response system for measuring the temperature of the Si wafer has been demonstrated using the ACT-FD-LCI system. The model of the heat balance is constructed by measuring the temporal variation of a Si wafer temperature in order to obtain the correct energy influx from the plasma to the Si wafer. Furthermore, he demonstrated the measurement of temperature for Si wafer to obtain the energy influx from plasma to the surface of the Si wafer depending on the bias voltage.

## 4.2 Experimental details

Figure 4.1 shows the schematic diagram of employing the 100 MHz excited capacitively coupled plasma (CCP) reactor. VHF (100 MHz) power was applied to the upper electrode. A 2 MHz bias power was supplied to the substrate, which was 4 inches in diameter on the lower electrode. The distance between the upper and the lower electrode was fixed at 30 mm. A Si wafer was electrostatically chucked to the lower electrode, which was maintained at a specific temperature  $20^{\circ}\text{C}$  by circulating a coolant, He gas was filled in the small gap of the wafer and the electrode obtaining a good thermal conductivity during plasma processes.  $\text{N}_2$  gas introduced from the upper electrode with a showerhead shape and total pressure was maintained at 2.0 Pa.

The setup for the measurement system of ACT-FD-LCI is shown in Fig. 4.2. The measurement system consists of a superluminescent diode (SLD), an optical circulator, an optical fiber, and a lens. The exit light from SLD irradiated the Si wafer through the optical circulator, the lens, and chamber components. The irradiated light is reflected off the back and front surface of the Si wafer. The spectral interferogram was observed using the array detector, which was a Hamamatsu linear image sensor with 1024 horizontal pixels. The time resolution was set at 50 ms.

As described in Section 2.2, this system can monitor the temperature by measuring optical path length of the Si wafer that depends on temperature while the initial wafer temperature and the wafer thickness were known. The coolant temperature was defined as the initial substrate temperature. The optical path length of a 480-mm-thick Si wafer was estimated by using Eq. (3.1). As expressed in Eq. (2.9), the ratio between the calculated and the measured optical path length is equivalent to the thickness ratio between the 480-mm-thick Si wafer and the used Si wafer. The Si wafer temperature was deduced from the thickness ratio and Eq (2.13). Hence, the Si wafer temperature was monitored in real time by using ACT-FD-LCI.

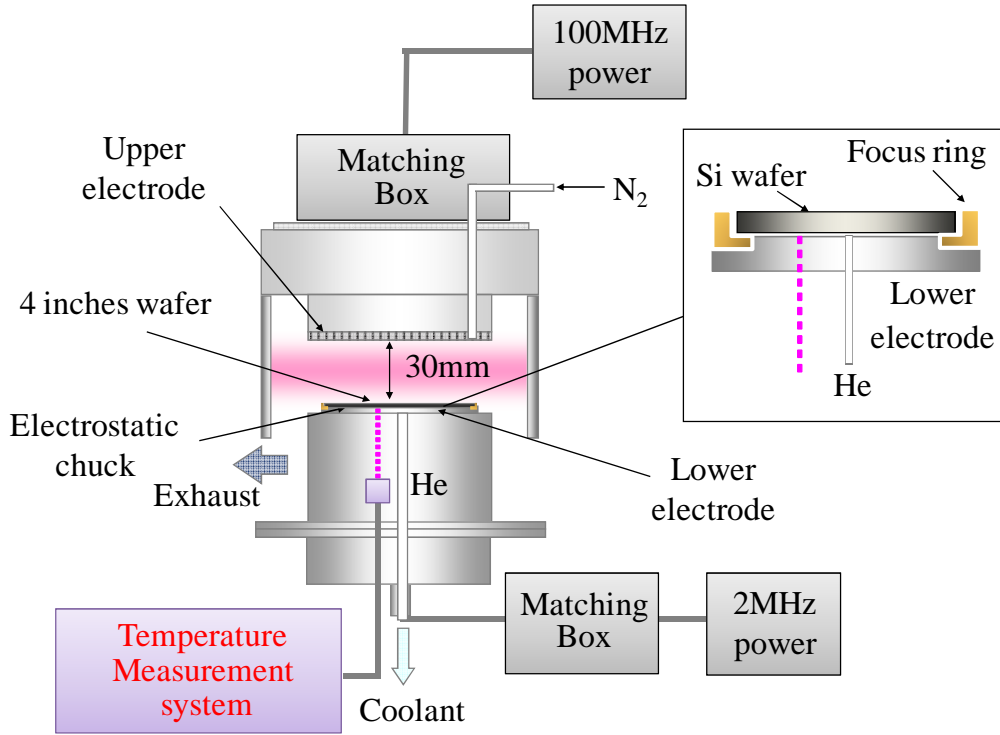


Fig. 4.1 Schematic diagram of experiment apparatus of dual frequency CCP etcher.

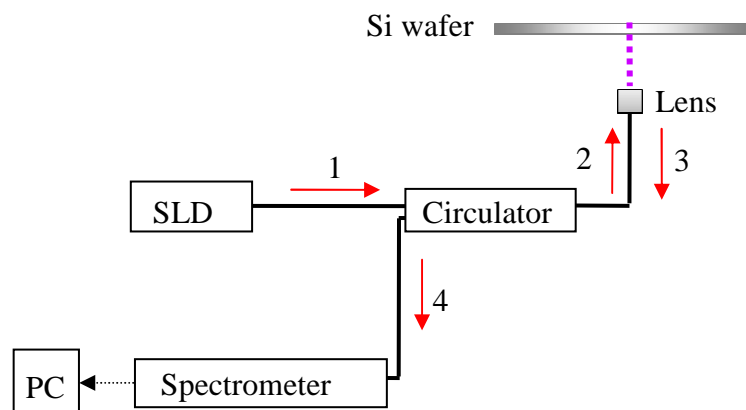


Fig. 4.2 Fiber optic system of ACT-FD-LCI for a temperature measurement. SLD stands for super luminescent diode as low coherent light source.

### 4.3 Results and discussion

#### 4.3.1 Model of heat balance in the substrate

It is important to consider the heat flux for the comprehension of the interaction between the plasma and the surface of the substrate and the control of the substrate-temperature during processes. I measured the temperature of the Si wafer during plasma processes by the ACT-FD-LCI. Figure 4.3 shows temporal variation of temperature of the Si wafer with VHF power of 400 W, without supplied power to the lower electrode. The temperatures of Si wafer were stable at 20°C before plasma exposures and rose rapidly after plasma exposures at all conditions.

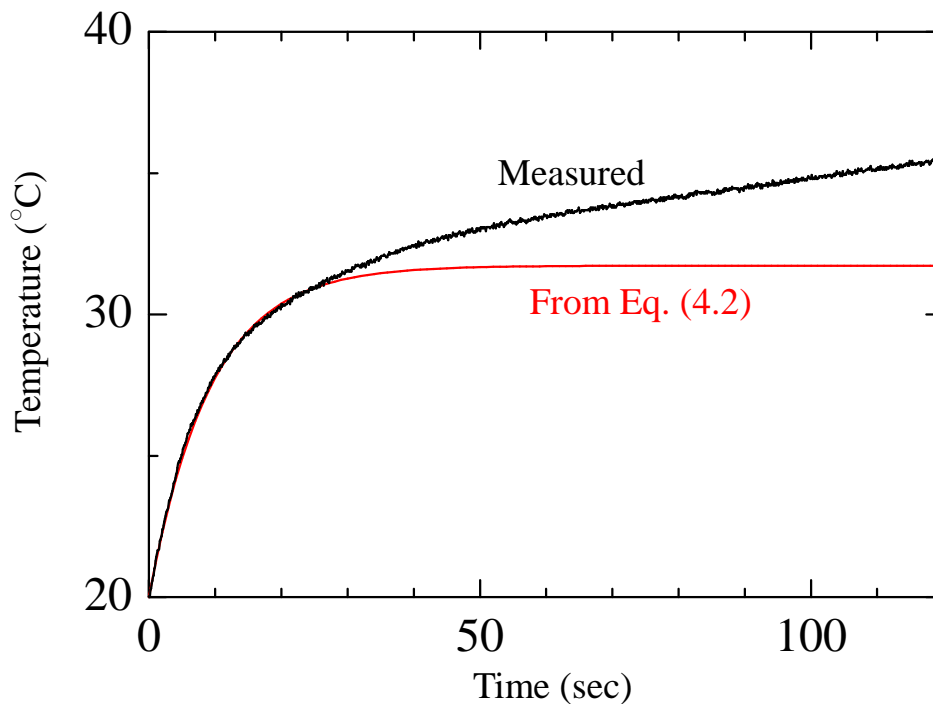


Fig. 4.3 Temporal variation of temperature of the Si wafer during plasma exposure.

I need to use the model of the heat balance in order to obtain the heat flux from the plasma to the substrate. As described in Section 1.4, The model reported is follows [21]:

$$\dot{Q}_{\text{IN}} = \rho c_p dA \frac{dT_W}{dt} + k_1 A (T_W - T_L) + k_2 A (T_W^4 - T_U^4), \quad (4.1)$$

where  $\dot{Q}_{\text{IN}}$  is the heat flux from plasma to the substrate in (W),  $\rho$  is the density ( $\text{kg m}^{-3}$ ),  $c_p$  is the heat capacity ( $\text{J kg}^{-1} \text{K}^{-1}$ ),  $d$  is the thickness of the wafer (m),  $A$  is the area of the wafer ( $\text{m}^2$ ),  $T_W$  is the wafer temperature (K),  $T_L$  is the temperature of the lower electrode (K),  $T_U$  is the temperature of the environment (K),  $t$  is the time (s),  $k_1$  is the conduction coefficient ( $\text{W m}^{-2} \text{K}^{-1}$ ) and  $k_2$  is the radiation coefficient ( $\text{W m}^{-2} \text{K}^{-4}$ ). The first term on the right-hand side expresses the temporal variation of the wafer temperature. The second term expresses the heat transfer between the wafer and the lower electrode. The third term expresses the radiative losses. In this study, this term was neglected due to the low temperature range relatively. Eq. (4.1) is solved as

$$T_W = T_L + \frac{\dot{Q}_{\text{IN}}}{k_1 A} \left[ 1 - \exp\left(-\frac{tk_1}{k_0}\right) \right], \quad (4.2)$$

where  $k_0$  was defined as  $\rho c_p d$  ( $\text{J m}^{-2} \text{K}^{-1}$ ). The  $T_L$  is expected to keep the initial temperature because of the efficient cooling by cooling medium and the low incoming power. It has been assumed that the thermal gradient within the wafer is negligible because of the good conductivity of the silicon wafer.

The curve obtained from Eq. (4.2) was fitted to experimental ones in order to obtain the heat flux from plasma to substrate and the heat transfer coefficient from the Si wafer to the lower electrode. The obtained curve corresponded to measured temperature under 25 sec as shown in Fig. 4.3. Over 25 sec, the curve was saturated while the measured temperature gradually increased. This result indicated that the heat flux deduced from Eq. (4.2) was susceptible to error in this experiment. This non-saturated temperature increase is possibly explained by the temperature increase of

a focus ring (FR) shown in Fig. 4.1. Since the FR is not cooled, its temperature might reach relatively high. The high temperature of the FR resulted in increasing amounts of heat transfer from the FR to the Si wafer with the time of plasma exposure. I assumed that the influence of the FR on the heating curve is insufficient at the beginning of the plasma exposure. The assumption indicates that the heat flux and  $k_1$  obtained by using Eq. (4.2) are precise.  $\dot{Q}_{IN}$  and  $k_1$  obtained by fitting Eq (4.2) to the heat curve under 5 sec were 6.7 W and  $62 \text{ Wm}^{-2}\text{K}^{-1}$ , respectively. ACT-FD-LCI can measure the average temperature along the depth direction of the Si wafer. Under this experiment the temperature distribution of the Si wafer along the depth direction need to be estimated. In static state the different temperature between the front and the back surface is given by

$$\frac{\dot{Q}_{IN}}{A} = \frac{k_{Si}}{d}(T_1 - T_2), \quad (4.3)$$

where  $k_{Si}$  is the heat conductivity of the Si wafer,  $T_1$  is the temperature of the front surface (K), and  $T_2$  is the temperature of the back surface (K). The used Si wafer was 4 inches in diameter and was 400  $\mu\text{m}$  thick.  $k_{Si}$  was used for  $168 \text{ Wm}^{-1}\text{K}^{-1}$ . From Eq. (4.3) the different temperature was 0.002 K. Under this experimental condition, hence, the temperature measured by ACT-FD-LCI could be considered as the wafer temperature.

The model of the heat balance considering the heat transfer from the FR to the wafer is given by

$$\dot{Q}_{IN} = \rho c_p dA \frac{dT_W}{dt} + k_1 A (T_W - T_L) + k_3 A_2 (T_W - T_F), \quad (4.4)$$

where  $k_3$  is the heat transfer coefficient from the FR to the wafer ( $\text{W m}^{-2} \text{K}^{-1}$ ),  $A_2$  is the area of the thermal contact surface between the FR and the wafer,  $T_F$  is the temperature of the FR. The temporal variation of the FR temperature was derived from Eq. (4.4) which were plugged for. Solution of Eq. (4.4) gives

$$\dot{Q}_{\text{IN}} - \rho c_p dA \frac{dT_{\text{W}}}{dt} - k_1 A (T_{\text{W}} - T_{\text{L}}) = k_3 A_2 (T_{\text{W}} - T_{\text{F}}). \quad (4.5)$$

The value of the left-hand side of Eq. (4.5) was obtained by plugging the  $\dot{Q}_{\text{IN}}$ , the  $k_1$ , and the  $T_{\text{W}}$ . Figure 4.4 shows the temporal variation of the value. Moreover, the heat curve of the FR was defined as

$$T_{\text{F}} = \Delta T_{\text{max}} [1 - \exp(-t / \tau)] + T_{\text{L}}, \quad (4.6)$$

where  $\Delta T_{\text{max}}$  and  $\tau$  are the equilibrium temperature and the thermal time constant. The curve given by the right-hand side of Eq. (4.6) was fitted to the values shown in Fig. 4.4 in order to obtain  $\Delta T_{\text{max}}$  and  $\tau$ .  $\Delta T_{\text{max}}$  and  $\tau$  were 195°C and 630 s, respectively. Figure 4.5 shows the measured temperature of the Si wafer and the deduced temperature of the FR to discuss the influence of the heat transfer from the FR to the wafer. When the FR temperature is lower than the wafer temperature, for 42 sec after plasma discharge, the third term on the right-hand side of Eq. (4.4) behaves as the heat losses. On the other hand, the third term behaves as the heating term when the FR temperature is higher than the wafer temperature.

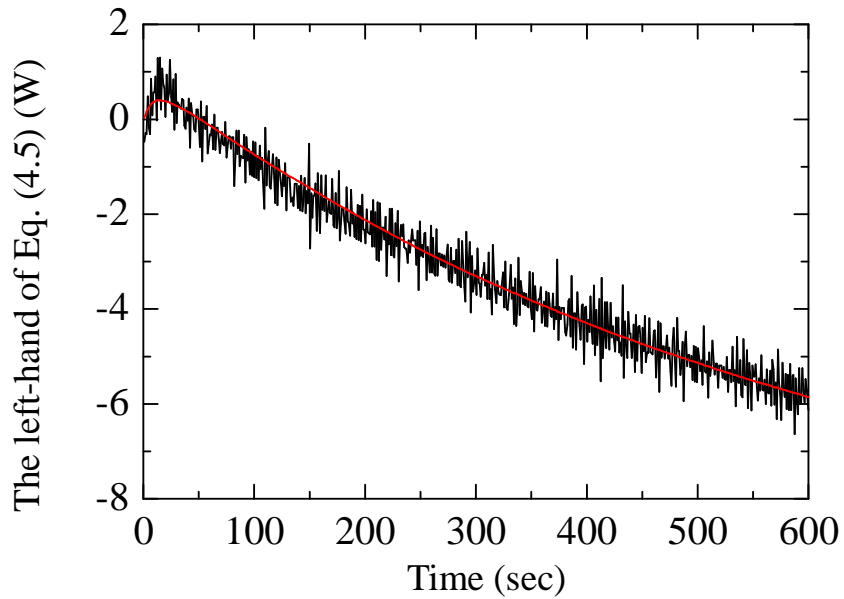


Fig. 4.4 The value of the left-hand of Eq. (4.5) as a function of process time and the fitting line obtained from the right-hand of Eq. (4.5) and Eq. (4.6).

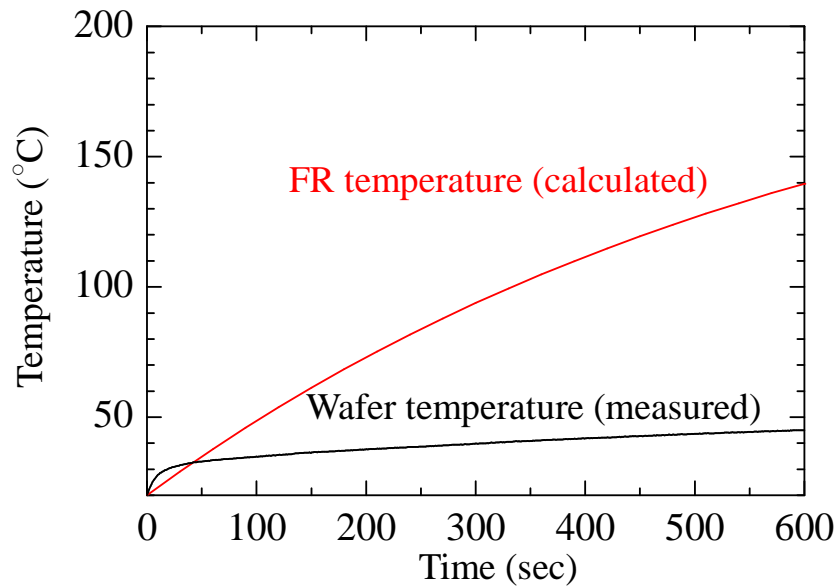


Fig. 4.5 Temporal variation of the measured temperature of the Si wafer and of the calculated temperature of the focus ring.

## Chapter 4

Figure 4.6 shows the temporal variation of the wafer temperature derived from Eq. (4.4) to which the values of  $\dot{Q}_{IN}$ ,  $k_1$ ,  $\Delta T_{max}$ ,  $\tau$ , and  $k_3A_3$  were assigned. The calculated temperature of the Si wafer was approximately corresponding to the measured temperature. However, the different between the measured temperature and the calculated one occurred in time from 10 sec to 60 sec. This phenomenon was shown in Fig. 4.4. The possible explanation for the temperature difference was the improper assumption of the temporal variation of the FR temperature under 60 sec. It means that the heat curve of the FR defined as Eq. (4.6) does not exponentially increase immediately after the plasma exposure. On the other hand, two temperatures of the Si wafer were corresponding under 10 sec because the influence of increasing the FR temperature on the Si wafer is neglected at the beginning of the plasma exposure.

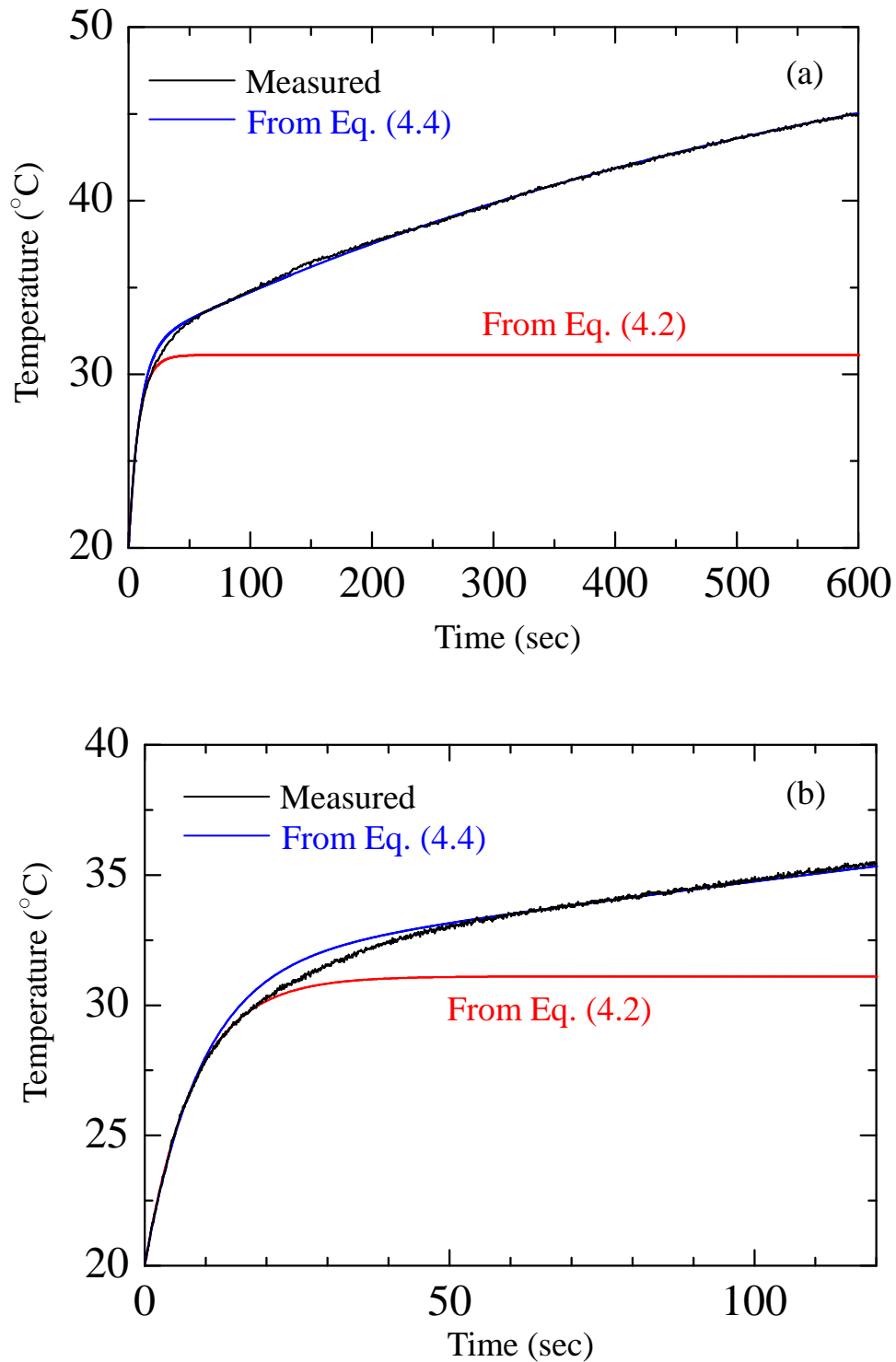


Fig. 4.6 Temporal variation of the measured and calculated temperatures of the Si wafer in time between 0 and (a) 600 sec, and (b) 120 sec.

The author investigated the influence of the FR on the radial distribution of the temperature in the Si wafer. Figure 4.7 shows the illustration of the analysis method for the radial distribution of the wafer temperature. This method assumes that the distribution of the substrate temperature in height direction and the distribution of the energy influx from the plasma in radial direction are uniform. The Si wafer was divided into 254 cells, which are 400  $\mu\text{m}$  cell because the Si wafer was 4 inches in diameter and 400  $\mu\text{m}$  in thickness. The heat balance of the cell is given by

$$\rho c(dx dy dz) \frac{dT_{xn}}{dt} = (Q_{\text{plasma}} + Q_x) - (Q_{\text{He}} + Q_{xn+1}), \quad (4.7)$$

where  $T_{xn}$  is the cell temperature (K),  $Q_{\text{plasma}}$  is the heat flux from plasma to the cell (W),  $Q_{xn}$  is the heat flux from the next cell to the cell (W),  $Q_{\text{He}}$  is the heat flux from the cell to the lower electrode cell through Helium gas (W).  $Q_{\text{plasma}}$  and  $Q_{\text{He}}$  are expressed as

$$Q_{\text{plasma}} = \frac{\dot{Q}_{\text{IN}}}{A} dx dy, \quad (4.8)$$

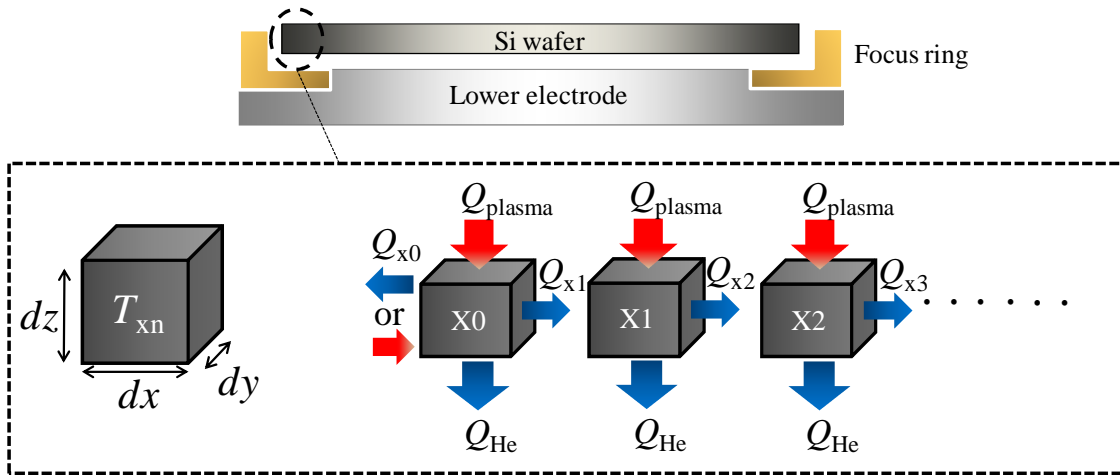


Fig. 4.7 Schematic illustration of analysis for the radial distribution of the substrate temperature.

$$Q_{\text{He}} = k_1 (T_{\text{xn}} - T_L) dx dy. \quad (4.9)$$

The values of  $\dot{Q}_{\text{IN}}$  and  $k_1$  obtained by fitting Eq (4.2) were estimated to 6.7 W and 62  $\text{Wm}^{-2}\text{K}^{-1}$ , respectively.  $Q_{\text{x0,254}}$ , which is the heat flux from the FR to the cell next to the FR, is given by

$$Q_{\text{x0,254}} = k_3 A_3 \frac{dy}{2\pi r} (T_F - T_{\text{x0}}), \quad (4.10)$$

where  $r$  is the radius of the Si wafer. As described above, the values of  $k_3 A_3$  obtained by Eq (4.5), (4.6), and the measured temperature of the Si wafer was estimated to  $6.2 \times 10^{-2} \text{WK}^{-1}$ . The others  $Q_{\text{xn}}$  are expressed as

$$Q_{\text{xn}} = k_{\text{Si}} \frac{(T_{\text{xn-1}} - T_{\text{xn+1}})}{dx} dy dz, \quad (4.11)$$

where  $k_{\text{Si}}$  is the heat conductivity of the Si wafer.  $k_{\text{Si}}$  was used for  $168 \text{Wm}^{-1}\text{K}^{-1}$ . From Eqs (4.7) - (4.11), the temporal variation of the radial distribution of the temperature in the Si wafer was estimated. Figure 4.8 shows the temporal variation of the radial distribution during  $\text{N}_2$  plasma exposure. The temperature of the Si wafer decreases with distance from the center of the wafer because of heat transfer from the cell at the edge to the FR when the FR temperature is lower than that of the Si wafer. As shown in Fig. 4.8(b) and (c), the temperature difference between the center cell and the edge cell were 0.02 and  $0.27^\circ\text{C}$  at 1 and 10 sec, respectively. These results indicated that the measured temperature of the wafer by ACT-FD-LCI is independent on the location of temperature measurement during plasma exposure within a few seconds. The temperature difference in the Si wafer gradually widens since the FR temperature exceed the temperature of the Si wafer. As shown in Fig. 4.8(d) and (e), the temperature different between the center cell and the edge cell were 0.82, 3.27, and  $5.76^\circ\text{C}$  at 100, 300, and 600 sec, respectively. Hence, it is necessary to consider the location, which the signal light pass through, on the measured temperature of the Si wafer.

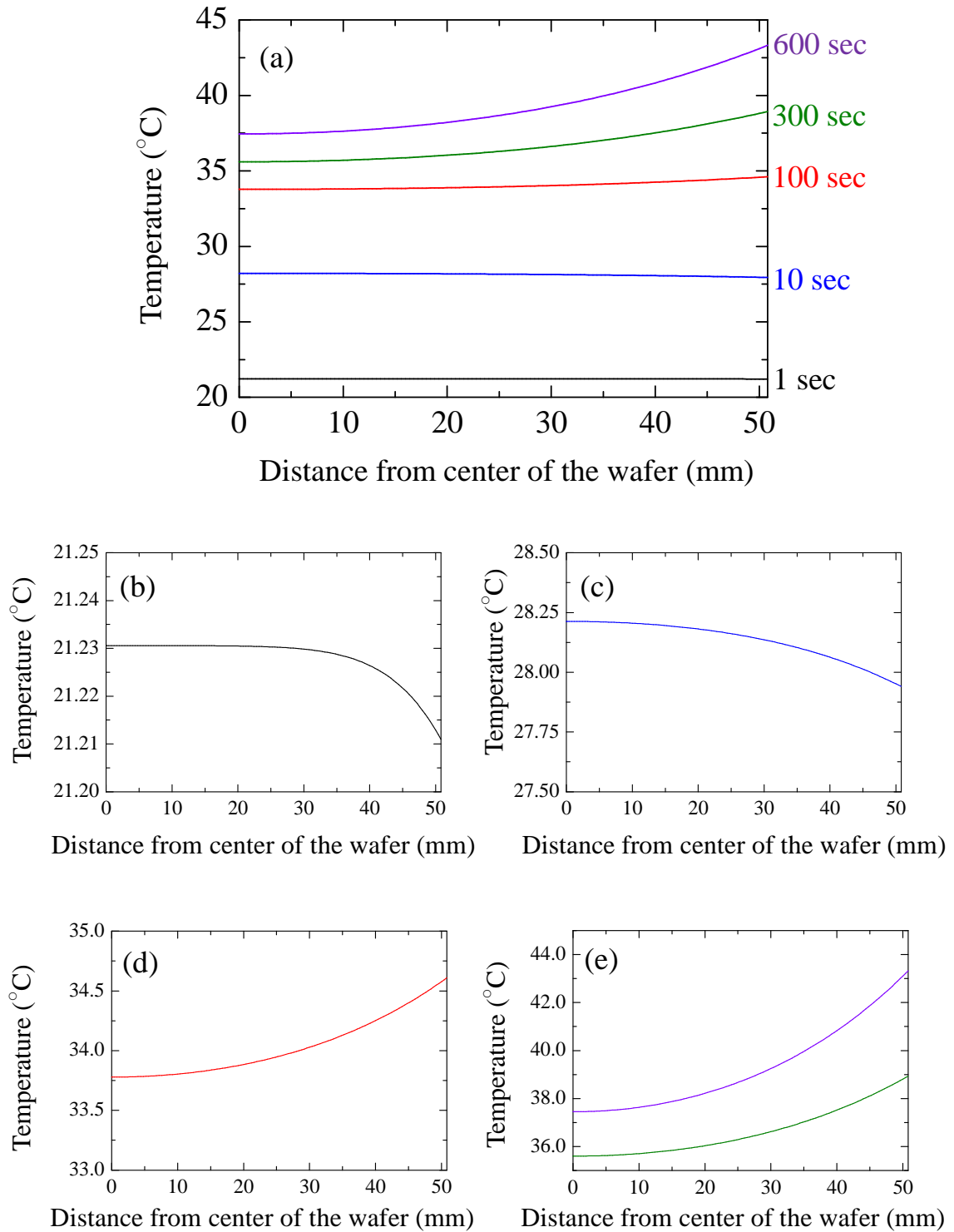


Fig. 4.8 Temporal variation of the radial distribution of the Si wafer temperature (a) for 600 sec, (b) at 1 sec, (c) at 10 sec, (d) at 100 sec, (e) at 300 and 600 sec.

### 4.3.2 Temporal variation of substrate temperature during plasma process

The author measured the temperature of Si wafer during plasma processes by the ACT-FD-LCI when the bias power applied to the lower electrode. Figure 4.9(a) shows temporal variation of temperature of Si wafer with the bias voltages of 10 to 131 V. The temperatures of Si wafer were stable at 20°C before plasma exposures and rose rapidly after plasma exposures at all conditions. The Si wafer were cooled and reached the same temperature rapidly after the plasma was switched off. Figure 4.9(b) shows the variation of the temperature from 0 sec to 3 sec. the slight change of temperature was measured at the beginning of the plasma exposure due to the high response and time resolution of ACT-FD-LCI.

As described in Section 4.3.1, the curve obtained from Eq. (4.2) was fitted to experimental ones in order to obtain the heat flux from plasma to substrate and the heat transfer coefficient from the Si wafer to the lower electrode. To neglect the influence of the FR on temporal variation of the wafer temperature, experimental values at times from 0 sec to 10 sec are fitted. The heat flux varies with the bias power as show in Fig. 4.10. The heat flux from plasma to the Si wafer increased with increase in the bias voltage. In general, the heat source contains the heat radiation, the power transfer by the charge carriers (electrons and ions), and the contribution of neutral particles. The energy influx by the ions is given by [20]

$$J_i = j_i \delta e V_{\text{bias}}, \quad (4.12)$$

where  $j_i$  is the ion particle flux density,  $\delta$  is the efficiency of energy transfer to the substrate,  $eV_{\text{bias}}$  is expressed as the free fall energy. From Eq. (4.12), the energy influx by the ions increases in proportion to the bias voltage. The efficiency of energy transfer given by [20, 22]

$$\delta = 4k_c \frac{M_1 M_2}{(M_1 + M_2)^2} (\sin\Theta/2)^2, \quad (4.13)$$

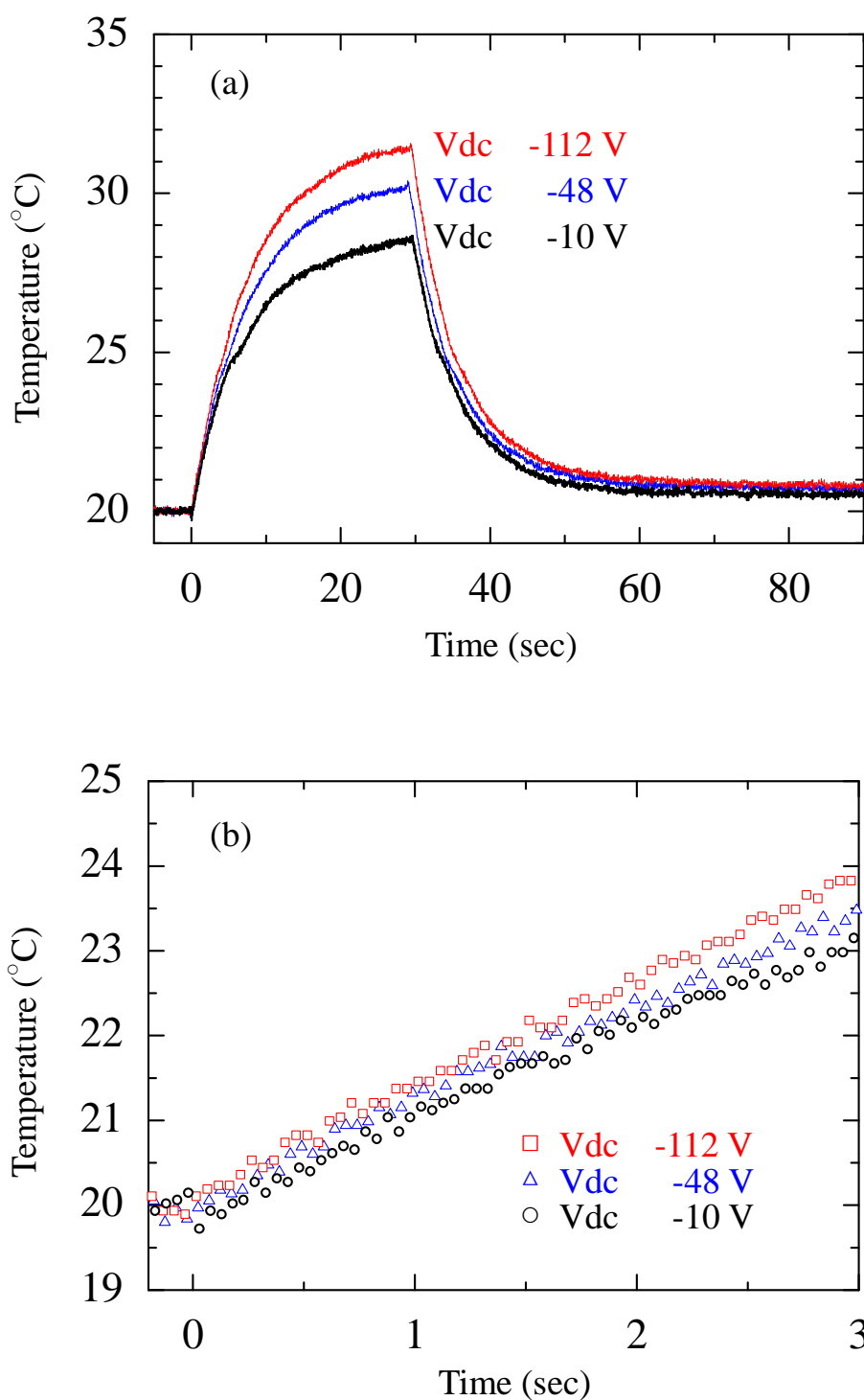


Fig. 4.9 Temporal variation of the Si wafer temperature during plasma exposure for various bias voltages.

where  $k_c$  is the kinetic transfer coefficient,  $M$  is the mass of the colliding particles,  $\Theta$  is the angle of incident. Under low-pressure conditions, the ion particle flux can be corresponding to the Bohm equation and be given by

$$j_i = n_e \sqrt{\frac{kT_e}{m_i}} \exp(-0.5), \quad (4.14)$$

where  $m_i$  is the mass of ions,  $T_e$  is the electron temperature,  $n_e$  is the electron density. Eq. (4.12), (4.13), and (4.14) indicated that the electron density or the electron temperature is obtained from the slope of the heat flux as a function of the bias voltage when either the electron temperature or the electron density is known. Moreover, the heat transfer coefficient from the Si wafer to the lower electrode shown in Fig. 4.11 is about  $82.3 \text{ W/m}^2 \cdot \text{K}$  and is independent of the bias power.

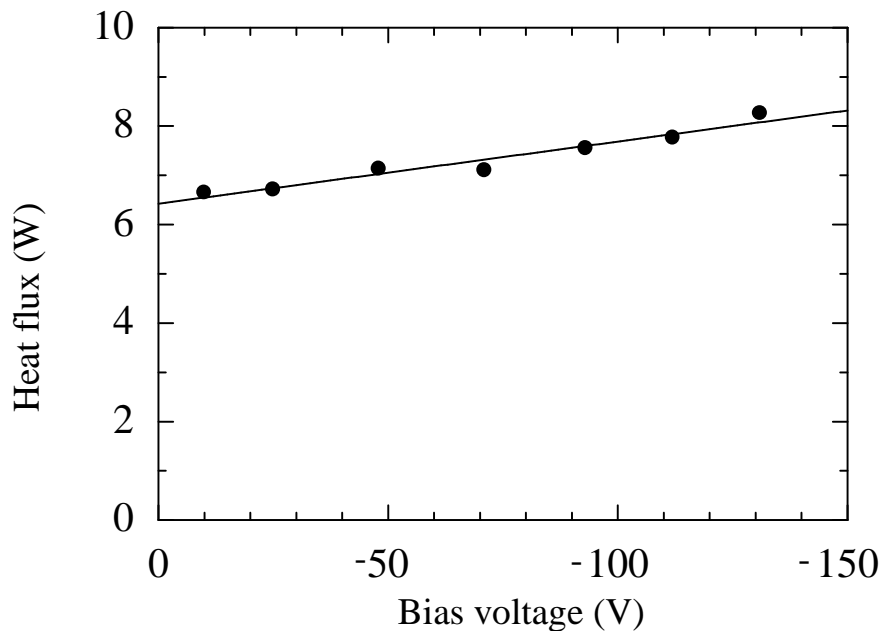


Fig. 4.10 Heat flux from the plasma to the Si wafer as a function of the bias voltage.

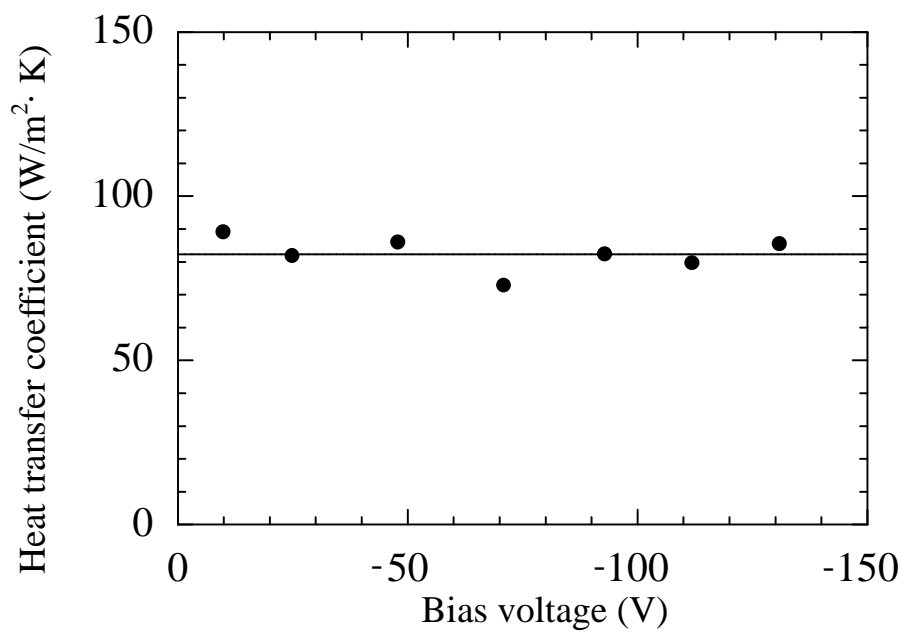


Fig. 4.11 Heat transfer from wafer to the lower electrode as a function of the bias voltage.

#### 4.4 Conclusion

It is important to comprehend the interaction between the plasma and the surface of the substrate and the control of the substrate-temperature during processes. A high-precision and rapid-response system for measuring the temperature of the Si wafer has been demonstrated using the autocorrelation-type frequency-domain low-coherence interferometry (ACT-FD-LCI) system.

The model of the heat balance needs to consider the heat transfer from the chamber parts to the Si wafer in order to obtain the correct heat flux from the plasma to the Si wafer. The measured temperature of the Si wafer deviated from the existing model of the balance between the heating and the heat loss because the model neglected the influence of the temporal variation of the focus ring surrounding the Si wafer on the heat balance. I developed the model of the heat balance considering the influence of the temperature of the chamber parts around the Si wafer. Under this experiment, the temperature of focus ring obtained by the new model rose more slowly and reached higher equilibrium temperature than the temperature of the Si wafer. Due to increasing amounts of heat from the focus ring to the Si wafer, the measured temperature was gradually deviated from the existing model with processing time.

Author demonstrated the temperature measurement for the Si wafer to obtain the heat flux from plasma to the surface of the Si wafer depending on the bias voltage. The slight differences of the substrate-temperature at the bias voltages were measured at the beginning of the plasma exposure owing to the high precision and response of the ACT-FD-LCI system. The equilibrium temperatures depend on the bias voltage due to the energy influx by the ions increase with increasing the bias voltages. The electron density or the electron temperature is obtained from the slope of the heat flux as a function of the bias voltage when either the electron temperature or the electron density is known.

As estimated the heat flux from the plasma to the substrate, the variation of the

## Chapter 4

temperature of the chamber parts around the substrate causes error. To neglect the influence, the substrate-temperature needs to be measured by a high-precision and fast-response measurement system. Hence, these indicated that ACT-FD-LCI system is practically useful tool for the comprehension of the interaction between the plasma and the surface of the substrate and the control of the substrate-temperature during processes.

## 4.5 References

- [1] H. Sugai, K. Nakamura, Y. Hikosaka, and M. Nakamura, *J. Vac. Sci. Technol. A* **13**, 887 (1995).
- [2] M. Schaepkens, R. C. M. Bosch, T. E. F. M. Standaert, G. S. Oehrlein, and J. M. Cook, *J. Vac. Sci. Technol. A* **16**, 2099 (1998).
- [3] H. Oshio, T. Ichiki, and Y. Horiike, *J. Electrochem. Soc.* **147**, 4273 (2000).
- [4] T. Belmonte, L. Lefevre, T. Czerwicz, H. Michel, and A. Ricard, *Thin Solid Films* **341**, 27 (1999).
- [5] A. L. Myerson, *J. Chem. Phys.* **50**, 1228 (1969).
- [6] M. M. Pejovic, G. S. Ristic, C. S. Milosavljevic, and M. M. Pejovic, *J. Phys. D* **34**, 2536 (2002).
- [7] P. Macko, P. Veis, and G. Cernogora, *Plasma Sci. Technol.* **13**, 251 (2004).
- [8] H. Yamamoto, H. Kuroda, M. Ito, T. Ohta, K. Takeda, K. Ishikawa, H. Kondo, M. Sekine, and M. Hori, *Jpn. J. Appl. Phys.* **51**, 016401 (2012).
- [9] J. L. Booth, B. T. Beard, J. E. Stevens, M.G. Blain, and T. L. Meisenheime, *J. Vac. Sci. Technol. A* **14**, 2356 (1996).
- [10] J. L. Cui, K. Amtmann, J. Ristein, and L. Ley, *J. Appl. Phys.* **83**, 7929 (1998).
- [11] U. J. Gibson and M. Chernushenko, *Opt. Express* **4**, 443 (1999).
- [12] A. Cardoso and A. K. Srivastava, *J. Vac. Sci. Technol. B* **19**, 397 (2001).
- [13] V. M. Donnelly and J. A. McCaulley, *J. Vac. Sci. Technol. A* **8**, 84 (1990).
- [14] T. Tsutsumi, T. Ohta, K. Ishikawa, K. Takeda, H. Kondo, M. Sekine, M. Hori, and M. Ito, *Appl. Phys. Lett.* **103**, 182102 (2013).
- [15] K. Takeda, Y. Tomekawa, T. Shiina, M. Ito, Y. Okamura, and N. Ishii, *Jpn. J. Appl. Phys.* **43**, 7737 (2004).
- [16] T. Ohmi, T. Ichikawa, T. Shibata, K. Matsuda, and H. Iwabuchi, *Appl. Phys. Lett.* **53**, 45 (1988).
- [17] T. Ohmi, T. Ichikawa, T. Shibata, K. Matsuda, and H. Iwabuchi, *J. Appl. Phys.* **66**,

## Chapter 4

4756 (1989).

[18]T. Kuroda and H. Iwakuro, Jpn. J. Appl. Phys. **29**, 923 (1990).

[19]T. Ohiwa, K. Horioka, T. Arikado, I. Hasegawa<sup>1</sup> and H. Okano, Jpn. J. Appl. Phys. **31**, 405 (1992).

[20]H. Kersten, H. Deutch, H. Steffen, G. M. W. Kroesen, R. Hippler, Vacuum **63**, 385 (2001).

[21]I. Hussla, K. Enke, H. Grünwald, G. Lorenz, and H. Stoll, J. Phys. D **20**, 889 (1987).

[22]H. F. Winters and D. Horne, Phys. Rev. B **10**, 55 (1974).

## Chapter 4

## **Chapter 5 Etching processes of organic films with precise control of substrate temperature**

### **5.1 Introduction**

Plasma processes for etching, ashing, deposition, and cleaning are important technologies to improve the performance and the packing density of ultralarge-scale integrated circuits (ULSIs). In the past, parameters such as the applied power, the gas pressure, the mixture ratio of gases, the initial substrate temperature, i.e. the temperature of substrate holder, have been adjusted to optimize plasma processes. In the case of plasma etching process, the etched feature has been controlled by trial-and-error adjustment of parameters. However, the precise control of nanometer-scale etched feature comes with a difficulty due to many complicated phenomena occurring when varying parameters. To control etched features with high accuracy, it is necessary to clarify the interactions among the plasma and the substrate surface and the development mechanisms of etched feature.

One of the infrequently-reported complicated phenomena is the dependence of the temporal variation of substrate temperature on the etched feature. The etch rate and the etched feature are sensitive to the substrate temperature [1-4]. The etch selectivity in fluorocarbon plasmas was enhanced by adjusting the wall temperature since the loss coefficients of the fluorocarbon and the fluorine species from the plasma to the walls vary with temperature [3-6]. The sticking coefficient of a product protecting against sidewall etching of the trench depends on the surface temperature of the substrate [4, 6-8]. In the case of the process using several process gases, the low-mass molecules contribute to balance the homogeneous distribution of the gas temperature in the chamber due to the high mobility of the low-mass molecule gas. The molecules with lower mass tend to concentrate on the high-temperature region. In addition to these dependences of temperatures, under plasma processes with applying the high RF-power

such as the etching of silicon dioxide films, the substrate temperature rises a few hundred degrees from the initial temperature [9]. The interactions between the plasma and the substrate surface at the beginning and the end of processes need to be considered as entirely different conditions. Hence, it is difficult to clarify the formation mechanisms of etched feature.

To monitor and control of the substrate temperature during plasma processing, a noncontact substrate temperature measurement technique using an autocorrelation type frequency-domain low-coherence interferometry (ACT-FD-LCI) system has been developed [10]. The ACT-FD-LCI measured the optical path length of the substrate when adjusting the initial temperature of the substrate with a He backside cooling system. The temperature is estimated from the shift in the optical path length measured during plasma processes [11]. The system has significant advantages of response and precision over other methods [12-13].

In this chapter, Author introduced a feedback control system based on the actual temperature monitoring in real time by dynamical change of on-off intervals of plasma discharges to prevent complicating the formation mechanisms of etched feature. Moreover, the temperature dependence on the etched features of low- $k$  organic films employing a 100 MHz excited capacitively coupled plasma (CCP) reactor with 2 MHz biasing employing  $H_2$  and  $N_2$  mixture gases was investigated. The etching of the low- $k$  organic films by plasma process remains difficulties such as uniformity and roughness on etched surfaces [14-15]. Moreover, the etched feature of the organic film strongly depends on the substrate temperature [2]. He applied the system of feedback control of substrate temperature to the etching of low- $k$  organic film which has the difficulties of the fabrication and is extremely sensitive to temperature variations.

## 5.2 Experimental details

Figure 5.1 shows a schematic diagram of the experimental apparatus of a 100 MHz excited capacitively coupled plasma (CCP) reactor. A 2 MHz bias power was supplied to the lower electrode, where a Si wafer was set with a diameter of 100 mm. The Si wafer was electrostatically chucked to the lower electrode, which was maintained at a specific temperature 10°C, 50°C, and 90°C by circulating a coolant, He gas was filled in the small gap of the wafer and the electrode obtaining a good thermal conductivity during plasma processes. A mixture gas of H<sub>2</sub> and N<sub>2</sub> was introduced and a pressure was kept at 2.0 Pa. Flow rates of H<sub>2</sub> and N<sub>2</sub> gases were controlled by mass flow controllers. Processes were performed with the gas flow rate of 75 sccm for H<sub>2</sub> and 25 sccm for N<sub>2</sub>, 100 MHz power of 400 W and 2 MHz bias power of 200 W. The substrate temperature was measured every 50 ms by the ACT-FD-LCI. Optical emission spectroscopy (OES) was used for the diagnostics of gas phase in the plasma. The relative densities of specific species are estimated by the intensity of the optical emission. All monitoring systems could perform in real time. Measured data were collected in a main server and analyzed in real time. The computer server governed all actuators to control the plasma parameters.

An organic film, SILK, with SiO<sub>2</sub> hard mask of Line /Space (65 nm/65 nm) patterns was prepared on a Si wafer as an etching sample. The thickness of the SiO<sub>2</sub> hard mask was 20 nm and that of the organic film was 200 nm. The etched features were analyzed with the cross-section of the etched patterns observed using a scanning electron microscope (SEM, Hitachi, S-5200). The H<sub>2</sub>/N<sub>2</sub> plasmas were used to etch the organic films [16-19].

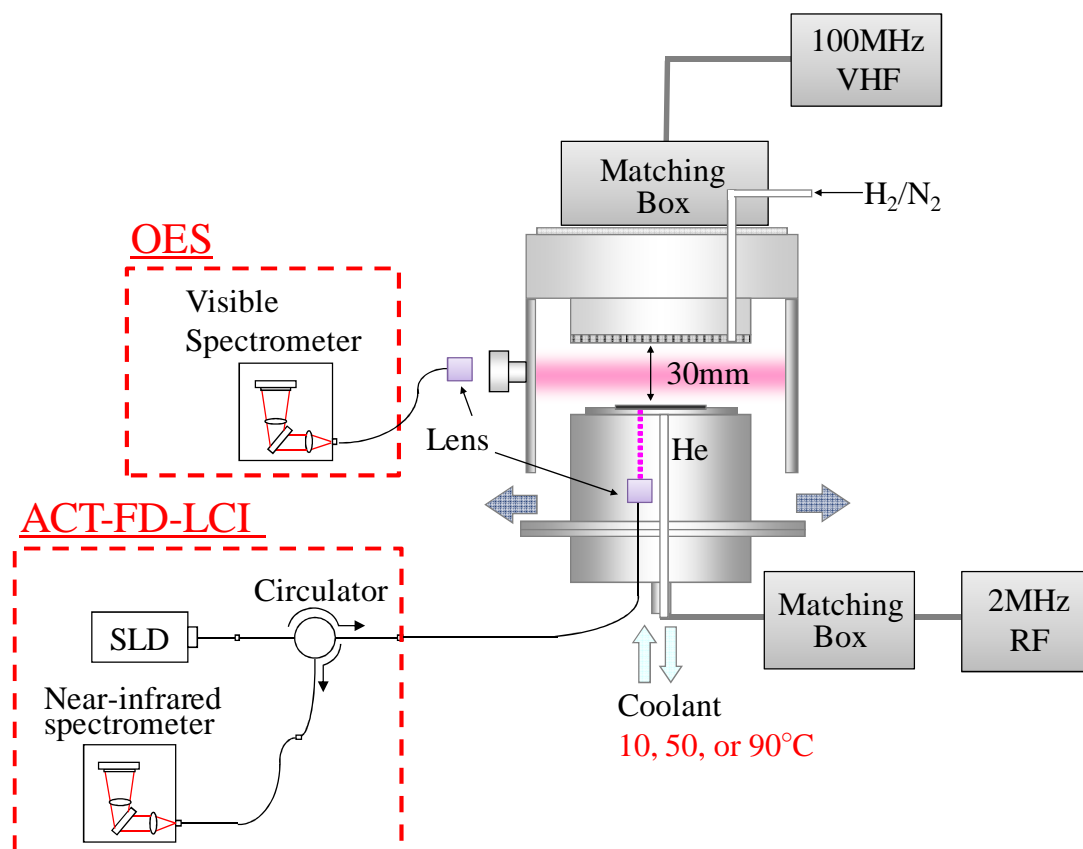


Fig. 5.1 Schematic diagram of experiment apparatus of dual frequency CCP etcher with ACT-FD-LCI and OES systems.

Figure 5.2 shows the schematic illustration of scheme for the substrate temperature control. First, the temperature increases with the time of plasma discharge and reaches the higher threshold. When reaching the threshold, the plasma turns immediately off to stop the temperature increase. Then, the substrate is cooled and a short period later, the temperature reaches the lower threshold. Next plasma discharge starts again and these sequences repeat until the finishing of etching process. The system controls all actuators; the intervals of on-off of the plasma discharge for maintaining the substrate temperature around  $20^{\circ}\text{C}$ ,  $60^{\circ}\text{C}$ , and  $100^{\circ}\text{C}$ . These temperatures of the coolant are set at  $10^{\circ}\text{C}$  lower than the specific temperatures of the lower electrode, i.e.  $10^{\circ}\text{C}$ ,  $50^{\circ}\text{C}$ , and  $90^{\circ}\text{C}$ . The higher thresholds were set at  $20.5^{\circ}\text{C}$ ,  $60.5^{\circ}\text{C}$ , and  $100.5^{\circ}\text{C}$ . The lower thresholds were set at  $20^{\circ}\text{C}$ ,  $60^{\circ}\text{C}$ , and  $100^{\circ}\text{C}$ .

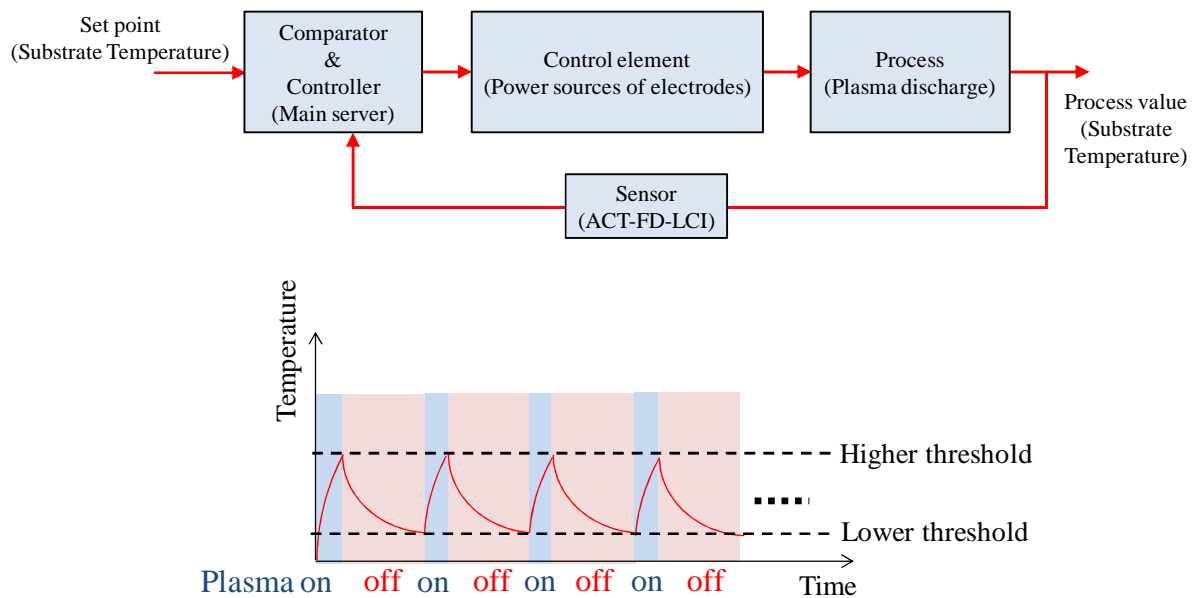


Fig. 5.2 Schematic illustration for the control of substrate temperature by the on-off of plasma discharge.

## 5.3 Results and discussion

### 5.3.1 Etch process with temporal control of substrate temperature

Figure 5.3 shows the temporal variation of the substrate temperature without and with the feedback control of that was monitored in real time. In the  $H_2/N_2$  plasma without control of the substrate temperature, the initial temperature was adjusted at  $20^\circ\text{C}$ . The substrate temperature reached about  $110^\circ\text{C}$  at 60 sec. In this feedback control, the on-off interval of plasma discharge was dynamically changed to keep the wafer temperature.

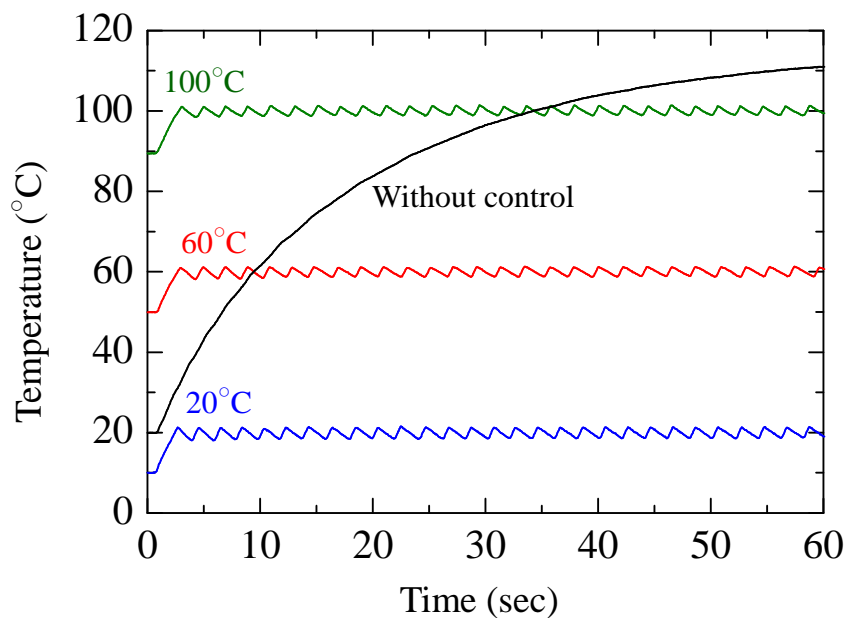


Fig. 5.3 Temporal variations of substrate temperature during plasma processes without and with controls of substrate temperatures.

Before investigating the effects of the wafer temperature on the etched feature, the author checked if the wafer temperature gives any changes in the plasmas. OES measurements were carried out for the plasmas with the wafer temperature of 20°C, 60°C, and 100°C. Figure 5.4 shows the optical emission spectra for all temperatures. These spectra show almost same feature in the wavelength range between 300 nm and 1000 nm. The results indicated that the influence of the substrate temperature on the plasma is negligible in this system and the etched feature is ascribed to the surface reaction for each wafer temperature.

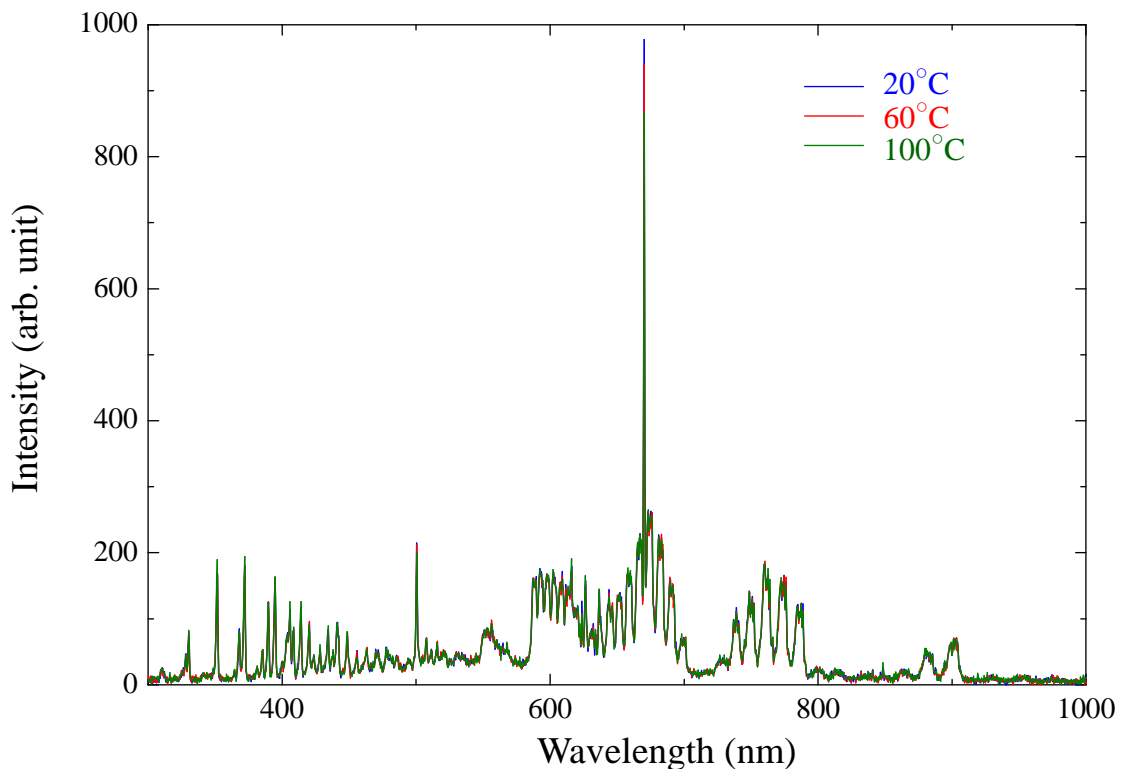


Fig. 5.4 Optical emission spectra of H<sub>2</sub>/N<sub>2</sub> plasmas when the substrate temperature was controlled at 20°C, 60°C, 100°C.

The first discharges were performed until the temperature reached the higher thresholds. As expressed in Eq. (4.1), the cooling efficiency was proportional to the different temperature between the wafer and the electrode. The initial temperatures, i.e. electrode temperature, were maintained at  $10^{\circ}\text{C}$  lower than the setting temperatures to get a cooling efficiency. Hence, the first discharges take long time compared to the other discharges. Figure 5.5 shows the duty ratio for each a discharge through the plasma processes. The duty ratio of the first discharge is the highest due to the longest discharge time. The duty ratio gradually decreased and finally saturated. This result indicated that it is difficult to maintain the specific temperature in conventional pulse discharge plasmas. As described in Section 4.3.1, the heat efflux from the wafer reduced due to increasing the temperature of the focus ring.

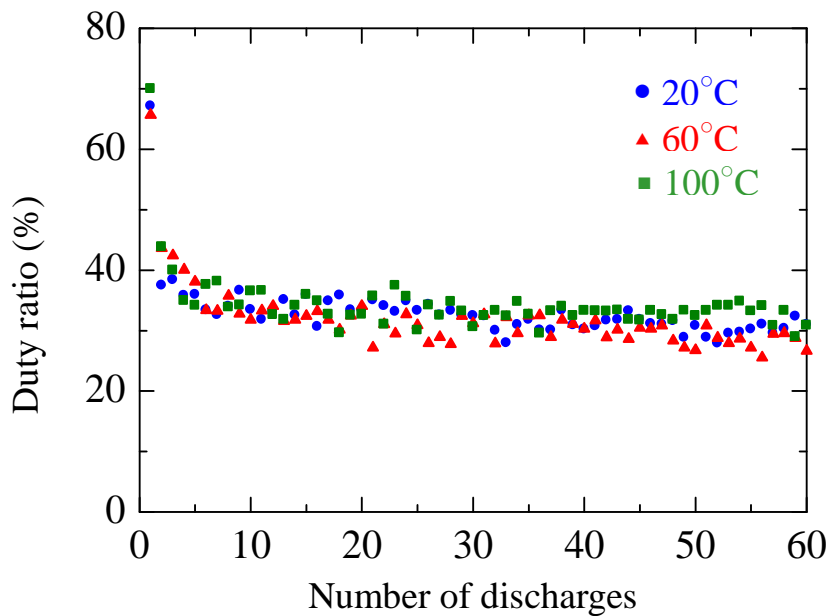


Fig. 5.5 Variations of duty ratio per a discharge in plasma processes with controls of substrate temperatures.

Figure 5.6 shows the fine temperature change for the setting temperatures of 20°C, 60°C, and 100°C in Fig. 5.3. The temperature gap between the higher and the lower threshold of temperature were set at 0.5°C. However, the actual temperature differences at 120 sec were 3.6°C, 3.3°C, and 3.1°C for the setting temperature of 20°C, 60°C, and 100°C, respectively. Both the maximum and the minimum of temperature exceeded the thresholds in all discharges.

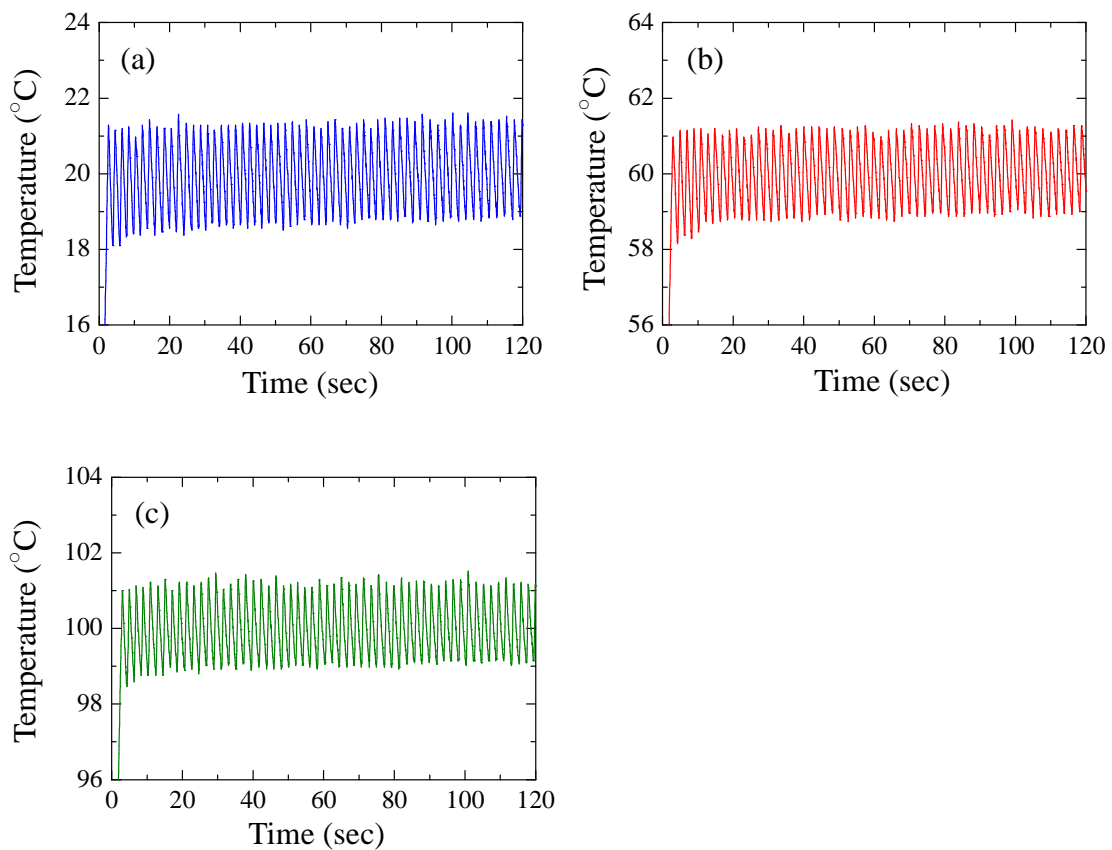


Fig. 5.6 Temporal variations of substrate temperature during plasma processes with controls of substrate temperatures at (a) 20°C, (b) 60°C, and (c) 100°C.

The computer server governed all actuators including power sources for the upper electrode and the lower electrode. Figure 5.7 shows the temporal variations of the substrate temperature and the bias voltage of the lower electrode. As described in Section 4.3.2, the increase rate in the substrate temperature was proportional to the bias voltage. The substrate temperature rose slowly at the initial rise of the bias voltage. After the substrate temperature exceeded the higher threshold, the increase rate reduced gradually with the decreasing of the bias voltage. Hence, the substrate temperature kept rising over the higher threshold while the bias voltage remained as a heat source for the substrate.

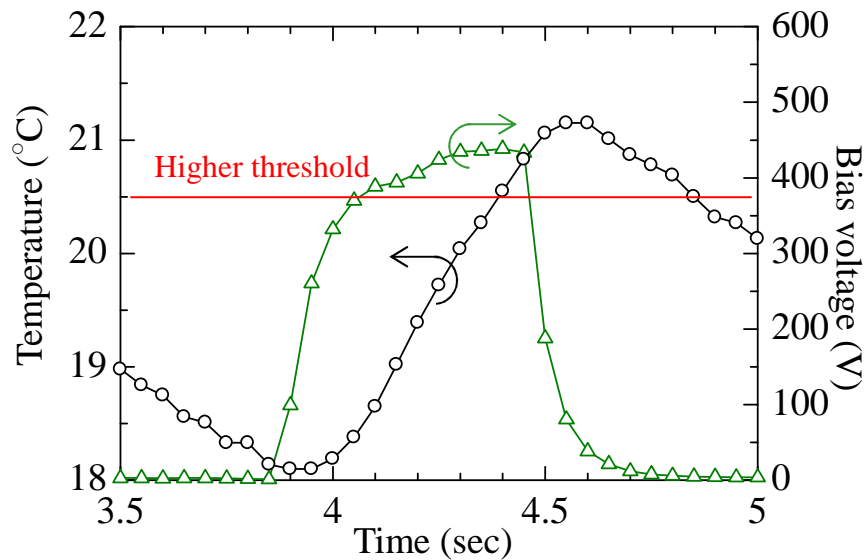


Fig. 5.7 the relation between the bias voltages of the lower electrode and the substrate temperature during plasma processes with controls of substrate temperatures.

Temporal variations of the supplied powers and the bias voltages of the electrodes in the control system are shown in Fig. 5.8. It takes 0.45 sec and 0.65 sec to supply the power into the upper electrode and the lower electrode from the signal output of control program for starting the discharge in system. The bias voltage of the upper electrode decreased after supplying the power into the lower electrode. These time lags on this system cause the overshoot of the substrate temperature under the lower threshold.

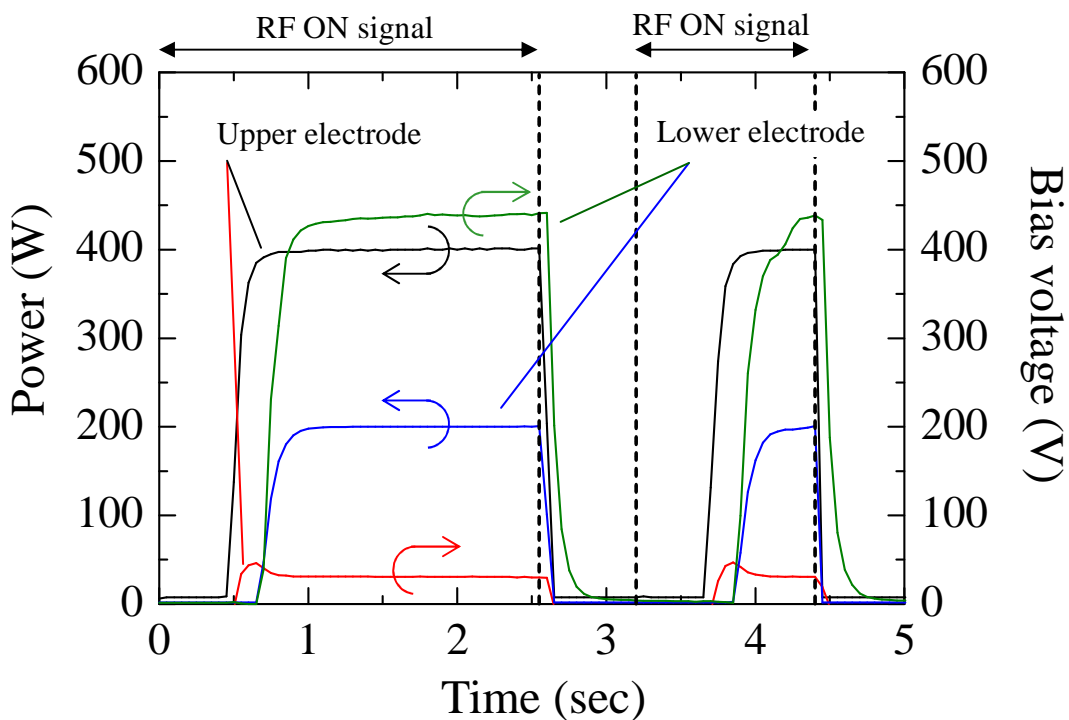


Fig. 5.8 temporal variations of the supplied powers and the bias voltages of two electrodes during plasma processes with controls of substrate temperatures.

### 5.3.2 Influence of substrate temperature on etch rates and features for organic film

To clarify the dependence of temperature on each rate and etched features, the etching processes of the organic film were performed by the  $H_2/N_2$  plasmas with control of the substrate temperature at  $20^\circ\text{C}$ ,  $60^\circ\text{C}$ , and  $100^\circ\text{C}$ . Figure 5.9 shows the cross section measured by SEM for every 10 sec of discharge time in all processes. These pictures indicated the dependence of the temperature on the trench widths. The higher the substrate temperature kept, the larger the trench width became. Moreover, the microtrenches at the trench bottom grew during plasma processes for  $20^\circ\text{C}$  and  $60^\circ\text{C}$ .

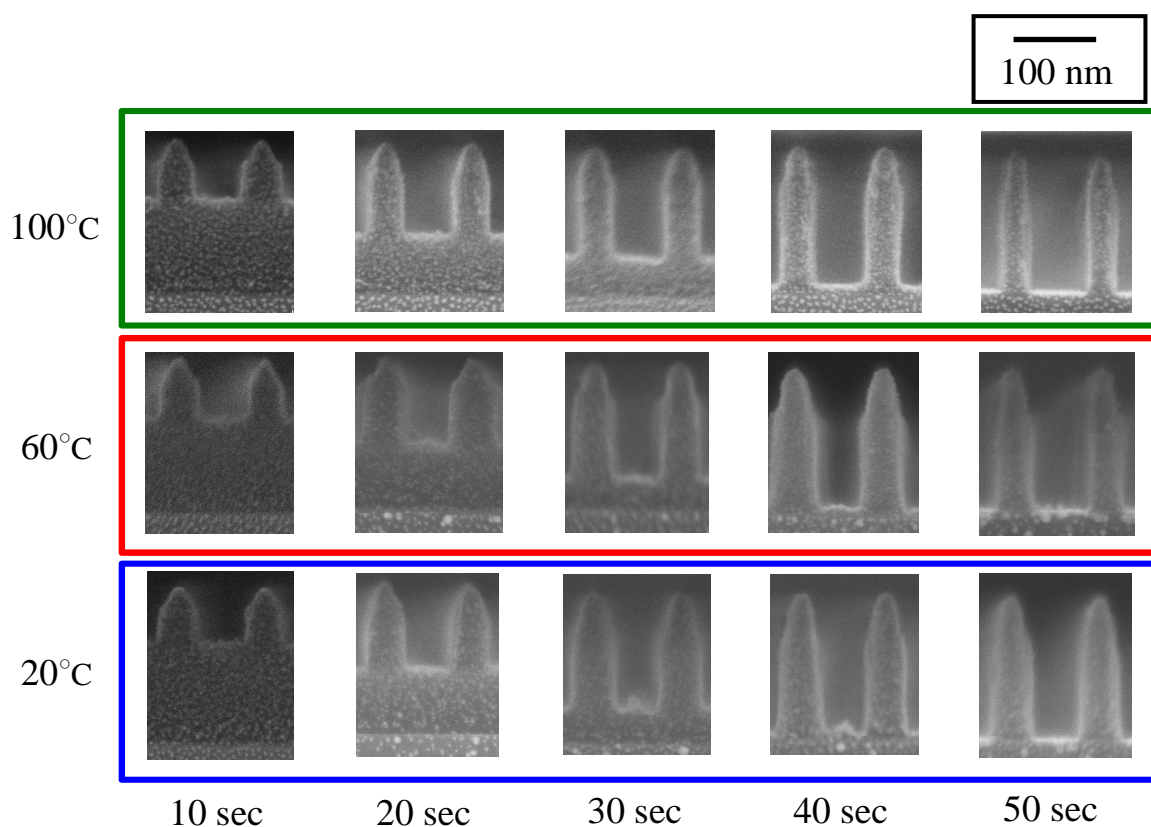


Fig. 5.9 SEM images of etched features of organic films.

The temperature dependence of the etch depth increasing with discharged time was shown in Fig. 5.10. These etch depths were estimated from 40 trenches in each temperature. Since variations of etch depth with discharged time were independent on temperature, the ion bombardments were contributed to the vertical etching of the organic film. Figure 5.11 shows the averaged vertical etching rate for all each ten seconds of the etching time in all temperatures. The accelerated ions near the substrate incident not only vertically, but also obliquely to the substrate. Since the ions have the density distribution as a function of incident angle or the incident ions collide against gas molecules in the trench, the number of the ions bombarding the surface of the bottom depends on the depth position of the bottom. This is why the rate of the vertical etching decreased with discharged time.

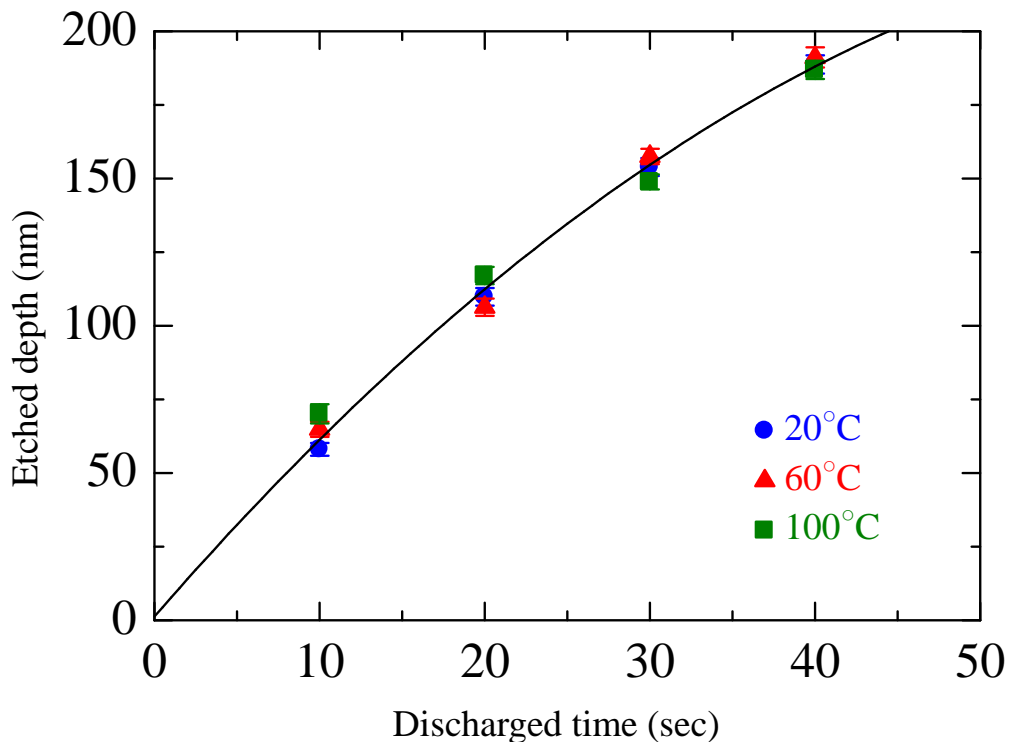


Fig. 5.10 Etch depth of organic film as functions of the discharged time and the substrate temperature.

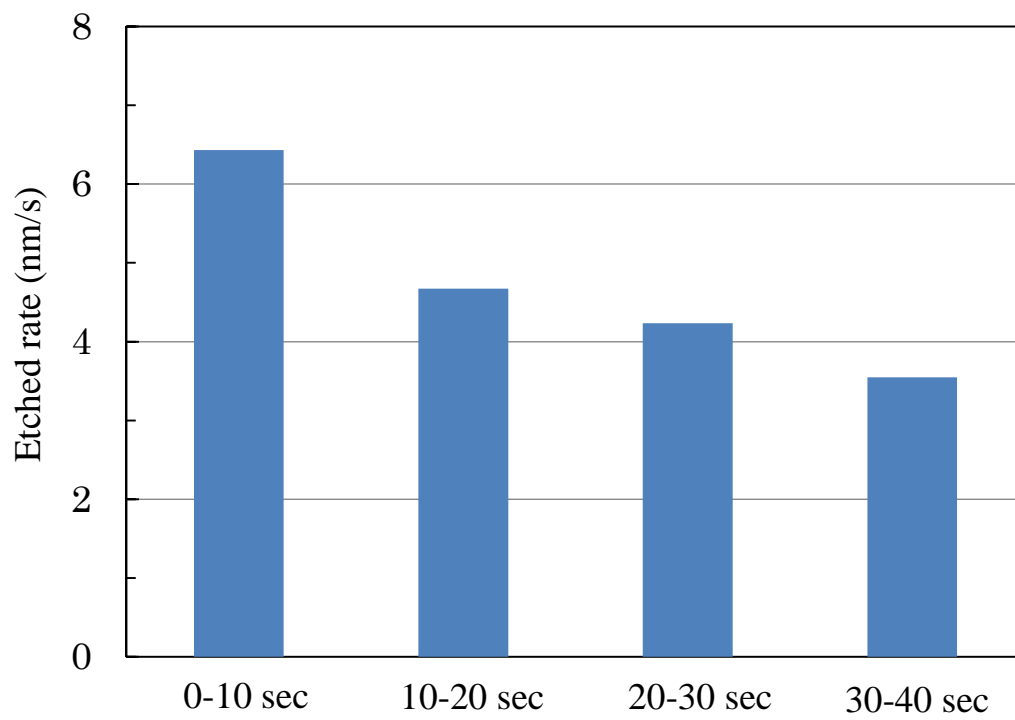


Fig. 5.11 Variation of the rate of the vertical etching with discharged time.

The variations of the width of etched bottom in all temperatures were shown in Fig. 5.12. Under 20°C and 60°C, the width decreased slightly with discharged time until 40 sec. Under 100°C, on the other hand, the width increased until 30 sec. These trends, which were the wider trench with the temperature, were indicated by Fig. 5.9. Hence, the etched features exhibit the sidewall tapering near the bottom in lower temperatures, and sidewall bowing in higher temperatures.

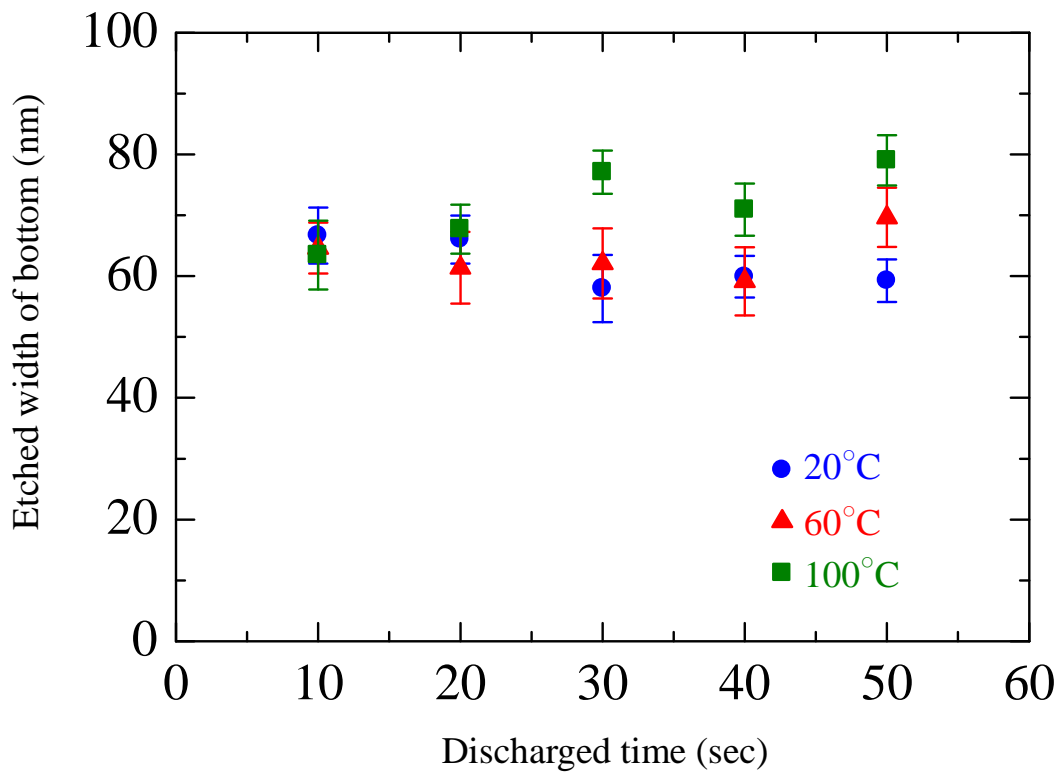
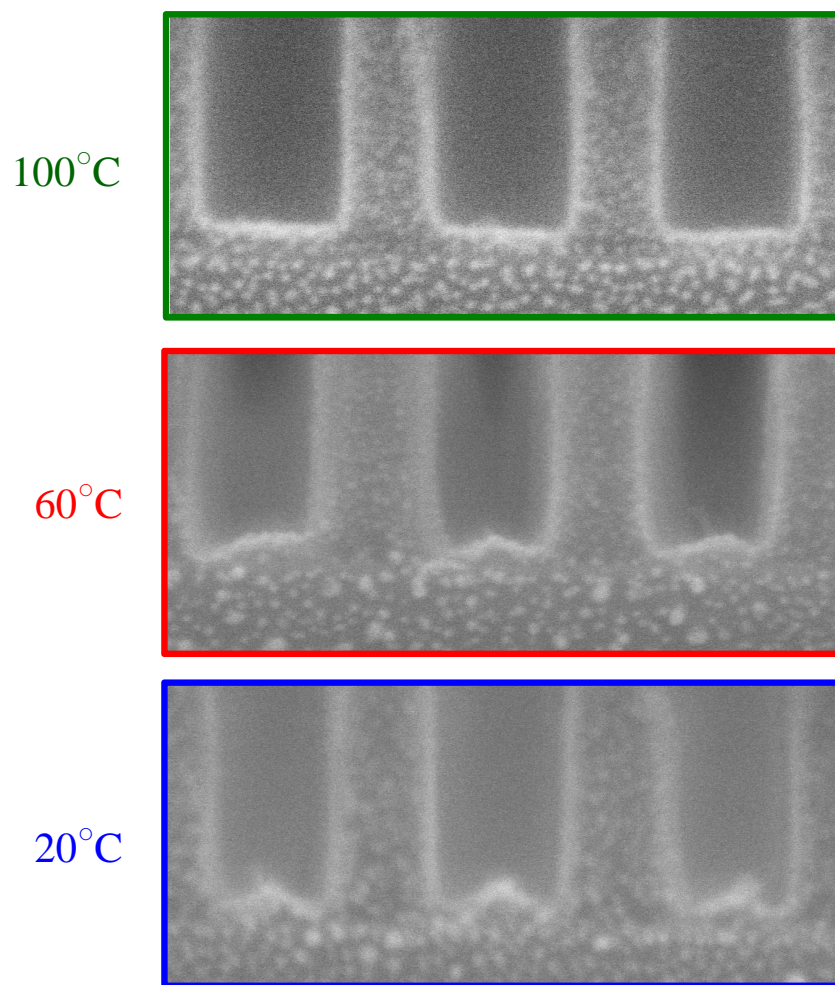


Fig. 5.12 Variation of the width of the etched bottom depending on the substrate temperature as a function of discharged time.

The etching feature during the over-etching exhibited over 43.3 sec when the process time of vertical etching of the organic film was estimated from the curve of quadratic approximation shown in Fig. 5.10. The widths of the bottom increased in 60°C and 100°C to etch the sidewall by H radical during over-etch. On the other hand, this behavior during over-etch was not observed under 20°C. Since the bottom width increased in the discharged time from 40 sec to 50 sec in 60°C, it is likely that the deposition of etch products on the sidewalls near the bottom prevented the horizontal etching under 40 sec. Under 100°C, however, the protection of the sidewalls near the bottom by etch products may be insufficient due to decreasing the sticking probability of the product on the sidewall with increasing temperature.

As shown in Fig. 5.13, which shows the feature of the bottom at 40 sec in all temperature, the surfaces anomalies such as microtrench improved with increasing temperature. It was reported that the microtrench and the tapering sidewalls are enhanced due to the sticking of etching products [20]. From these results, I considered that the variations of the etched width and the surface anomalies are probably different between 60°C and 100°C due to the temperature dependence of sticking probability of the etch product. Under 20°C the etched bottoms kept the width during over-etch. This is probably because a CN layer formed by N radicals protected the sidewalls against the horizontal etching. The temperature dependence of the formed layer by N<sub>2</sub> plasma was investigated by Yamamoto et al [2]. The nitride layers that formed on sidewalls at lower substrate temperatures are thicker than those at higher substrate temperatures. Under the conditions of N<sub>2</sub> plasma exposure at a high substrate temperature, the protective effect of the nitride layer was weak. From this characteristic of layer formed by N radicals, the etched bottoms kept the width during over-etch. The substrate temperature strongly influenced on the etched feature due to the temperature dependence of sticking probability of the etched products and the layer formed on the sidewalls by N radicals.



Discharged time: 40 sec

Fig. 5.13 SEM images of cross section near the etched bottom of organic film at discharged time 40 sec.

## 5.4 Conclusion

Increasing the substrate temperature makes it difficult to understand the developing mechanisms of etched feature because of the temperature dependence of the rate of chemical reaction between the radicals and materials and the sticking coefficient of etched products on the material surface. The author developed a feedback control system of actual wafer temperature monitored in real time by dynamical change of on-off intervals of plasma discharges to keep the substrate temperature constant. He applied the feedback control system of wafer temperature to plasma etching processes. The organic film was used as an etched sample because it is extreme sensitive to temperature.

This system achieved the control of the substrate temperature in plasma processes within  $3.6^{\circ}\text{C}$ . In the case of the plasma process without this system, the substrate temperature reached about  $110^{\circ}\text{C}$  at 60 sec after plasma exposure. Since the efficiency of cooling of the substrate reduced with discharged time due to increasing the temperature of the focus ring, it is difficult to keep the temperature constant in conventional pulse discharge plasma. The value of the bias voltage and the power of the upper electrode and the lower electrode were stored in the main server governing all actuators. The rate of increase in the substrate temperature was proportional to the bias voltage generated in the lower electrode. The rate of the change of substrate temperature relates closely to the bias voltage.

The  $\text{H}_2/\text{N}_2$  plasmas etching processes of the organic film were performed in different ranges of the substrate temperature by this system. The widths of the trench in the organic film increased with increasing the substrate temperature. Since the ions bombarding to the etched surface have the density distribution of incident angle or the incident ions collide against the gas molecules in the trench, the rate of the vertical etching decreased with increasing the depth of the bottom. Moreover, the substrate temperature strongly influenced on the etched feature due to the temperature

## Chapter 5

dependence of sticking probability of the etched products and the layer formed on the sidewalls by N radicals. Hence, this system of feedback control, which keeps the substrate temperature constant, is effective to clarify the interactions among the plasma and the surface of the substrate and the formation mechanism of etched features. Moreover, controlling the substrate temperature in step with discharged time, the control of an etched feature with high accuracy must be achieved.

## 5.5 References

- [1] T. Ohiwa, K. Horioka, T. Aricado, I Hasegawa, and H. Okano, *Jpn. J. Appl. Phys.* **31**, 405 (1992).
- [2] H. Yamamoto, H. Kuroda, M. Ito, T. Ohta, K. Takeda, K. Ishikawa, H. Kondo, M. Sekine, and M. Hori, *Jpn. J. Appl. Phys.* **51**, 016202 (2012).
- [3] H. Oshio, T. Ichiki, and Y. Horiike, *J. Electrochemical Soc.* **147**, 4273 (2000).
- [4] H. Abe, M. Yoneda, and N. Fujiwara, *Jpn. J. Appl. Phys.* **47**, 1435 (2008).
- [5] H. Sugai, K. Nakamura, Y. Hikosaka, and M. Nakamura, *J. Vac. Sci Technol. A* **13**, 887 (1995).
- [6] M. Schaepkens, R. C. M. Bosch, T. E. F. M. Standaert, G. S. Oehrlein, and J. M. Cook, *J. Vac. Sci. Technol. A* **16**, 2099 (1998).
- [7] A. Doshita, K. Ohtani, and A. Namiki, *J. Vac. Sci. Technol. A* **16**, 265 (1998).
- [8] H. Kersten, H. Deutch, H. Steffen, G. M. W. Kroesen, and R. Hippler, *Vacuum* **63**, 385 (2001).
- [9] C. Koshimizu, T. Ohta, T. Matsudo, S. Tuchitani, and M. Ito, *Appl. Phys. Express* **3**, 056201 (2010).
- [10] T. Tsutsumi, T. Ohta, K. Ishikawa, K. Takeda, H. Kondo, M. Sekine, M. Hori, and M. Ito, *Jpn. J. Appl. Phys.* **54**, 01AB03 (2015).
- [11] K. Takeda, Y. Tomekawa, T. Shiina, M. Ito, Y. Okamura, and N. Ishii, *Jpn. J. Appl. Phys.* **43**, 7737 (2004).
- [12] T. Tsutsumi, T. Ohta, K. Ishikawa, K. Takeda, H. Kondo, M. Sekine, M. Hori, and M. Ito, *Appl. Phys. Lett.* **103**, 182102 (2013).
- [13] T. Ohta, C. Koshimizu, K. Kawasaki, K. Takeda, and M. Ito, *J. Appl. Phys.* **105**, 013110 (2009).
- [14] W. Chen, Y. Morikawa, M. Itoh, T. Hayashi, K. Sugita, H. Shindo, and T. Uchida, *J. Vac. Sci. Technol. A* **17**, 2546 (1999).
- [15] Y. Morikawa, S. Yasunami, W. Chen, T. Hayashi, and T. Uchida, *J. Vac. Sci. Technol.*

## Chapter 5

- A **19**, 1747 (2001).
- [16]H. Nagai, S. Takashima, M. Hiramatsu, M. Hori, and T. Goto, J. Appl. Phys. **91**, 2615 (2002).
- [17]H. Nagai, M. Hiramatsu, M. Hori, and T. Goto, J. Appl. Phys. **94**, 1362 (2003).
- [18]S. Uchida, S. Takashima, M. Hori, and M. Fukasawa, Jpn. J. Appl. Phys. **47**, 3621 (2008).
- [19]C. S. Moon, K. Takeda, M. Sekine, Y. Setsuhara, M. Shiratani, and M. Hori, J. Appl. Phys. **107**, 113310 (2010).
- [20]K. Ono, H. Ohta, and K. Eriguchi, Thin Solid Films **518**, 3461 (2010).

## Chapter 5

## **Chapter 6 Conclusion and future works**

### **6.1 Conclusion of present research**

The motivation of this dissertation is to clarify the influence of the substrate temperature on plasma processes for fabrication of the semiconductor materials in atomic scale. To achieve this goal, author developed an autocorrelation type frequency-domain low-coherence interferometry (ACT-FD-LCI), which has advantages on the precision and the response of temperature measurement, and constructed a system of feedback control of actual substrate temperature.

In Chapter 1, the history of the large scale integrated circuits and the influence of temperature for plasma etching processes have been shown as the introduction. The energy influx from the plasma and the temporal variation of the substrate temperature in plasma processes were also introduced. The demands for the temperature measurement in plasma processes are described.

In Chapter 2, the experimental system for analysis of plasma internal parameters and etched features have been described. Theories of measurement of substrate temperature by using frequency-domain low-coherence interferometry and of etched features by using scanning electron microscopy (SEM) were introduced.

In Chapter 3, he evaluated the characteristic of ACT-FD-LCI system, which removes the reference mirror from the conventional frequency-domain low-coherence interferometry (FD-LCI) system. The standard deviation of temperature measurement by ACT-FD-LCI was less than  $0.04^{\circ}\text{C}$  at temperatures below  $550^{\circ}\text{C}$  for a typical Si thickness of  $480\ \mu\text{m}$ . Because of the common-path interferometry due to removing the reference mirror, ACT-FD-LCI can successfully reduce the noise arising from the mechanical vibration, the fiber-induced dispersion, and the polarization mismatch. This technique is a robust and practically useful tool for measuring the substrate temperatures during the plasma process and the rapid thermal process. However, at photon energies

## Chapter 6

near the band gap of the Si, increasing the substrate temperature emphasized the absorption of the signal light in the substrate. Hence, the accuracy and the temperature range of measurement strongly depended on the center wavelength of light source.

In Chapter 4, he measured the temporal variation of the substrate temperature during the plasma exposure to comprehend the interaction between the plasma and the surface of the substrate and the control of the substrate-temperature during processes. The temporal variation of the substrate temperature deviated from the existing model of the balance between the heating and the heat loss since the model neglected the change of the other chamber parts near the substrate. He constructed the model of the heat balance considering the change of the temperature of the parts during plasma exposure. The electron density or the electron temperature may be obtained from the slope of the heat flux as a function of the bias voltage generated in the lower electrode when either the electron temperature or the electron density can be known.

In Chapter 5, he developed the feedback control system of substrate temperature monitoring in real time and applied for the plasma etching process of an organic film to clarify the formation mechanisms of etched feature depending on the substrate temperature exactly. The substrate temperatures were maintained within a few degrees by dynamical change of on-off intervals of plasma discharges to prevent complicating the formation mechanisms of etched feature. The duty ratios per discharge reduced gradually because of increasing the temperature of the chamber parts around the substrate. The fact means that the conventional pulse discharge plasma was insufficient to keep the substrate temperature constant. The change of the substrate temperature relates closely to the bias voltage generated in the lower electrode. He performed the plasma etching processes of the organic film at several temperatures by using the system. The widths of the trenches in the organic film extended with increasing the substrate temperature. This is because of the temperature dependence of sticking probability of the etched products and the layer formed on the sidewalls by

radicals.

This study revealed the temperature dependence of the etched feature of the organic film, which are sensitive to the substrate temperature, during the H<sub>2</sub>/N<sub>2</sub> plasma by feedback control system. This system of feedback control, which keeps the substrate temperature constant, is effective to clarify the interactions among the plasma, the surface of the substrate and the formation mechanism of etched features.

## 6.2 Scopes for future works

In this dissertation, the influence of the substrate temperature during a plasma etching processes has been studied based on results obtained by the autocorrelation type frequency-domain low-coherence interferometry (ACT-FD-LCI), real-time measurement during plasma processes.

For the formation mechanism of etched features, the temporal variation of the substrate temperature need to be considered to clarify the interaction between the plasma and the sample surface, and the influence of sticking the etched products on the surface. These interactions can be also clarified by obtaining the temperature, estimating the energy influx from the plasma to the substrate, and controlling the substrate temperature during the plasma processes.

In this study, author constructed the high-precision and high-response system of temperature measurement, the feedback control system of the substrate temperature. These systems helped the comprehension of the formation mechanism of the etched feature of the organic film in  $H_2/N_2$  plasma etching processes. However, this study does not achieve the quantification of the relation between the substrate temperature and the etched feature for the atomic-scale plasma etching. The quantification includes the etched rates on the sidewalls and the bottom surfaces. the rates relates closely to the sticking coefficients of several neutral species on sample surfaces, the number of each species reaching to the sample, the number of incident ions to the sample. The quantification means determining how much effect these values has on the etched rates.

In addition to neutral species, ion bombardments to the sample surface assist the procedure for forming anisotropic etched feature. This phenomenon means that the ions can contribute the etched rate at the bottom surfaces. This study indicates that the energy flux by ion bombardments to the substrate increases with the bias voltage, but it does not quantify the relation between the temporal variation of the substrate

## Chapter 6

temperature and several factors such as the number of electron, electron temperature, and bias voltage.

The future work in this study is to quantify those phenomena about etched features with various diagnostic techniques including the ACT-FD-LCI system. The comprehension will be a guideline for the development of the computer simulation. Furthermore, it can construct a new plasma chemistry which enables to construct the next generation smart nano process.

Additionally, the sticking coefficients depending on the substrate temperature are estimated by measuring the spatial distribution or the temporal variation of the species density while monitoring the substrate temperature with the ACT-FD-LCI system. The system developed in this study help estimating the sticking coefficient considered to the substrate temperature. Sticking coefficients determine not only features in etching processes, but also film qualities in deposition processes. Hence, the substrate temperature relating to the sticking coefficient is the important factor in most fabrication processes for semiconductor devices. The ACT-FD-LCI system has potential as diagnostic techniques to improve performances of semiconductor devices.

In the near future, the integrated-knowledge obtained by the control of the substrate temperature would be expected to construct a basis of the Plasma Nano-Science.

## Chapter 6

## **Acknowledgements**

The present research has been performed in Prof. Hori and Prof. Sekine Laboratory, Department of Electrical Engineering and Computer Science, Nagoya University. The research results presented in this thesis could not have been obtained without the support of the following people.

First and foremost, the author would like to express my deep appreciation to Prof. Masaru Hori, Institute of Innovation for Future Society, Nagoya University, for having given me the opportunity to pursue a Ph.D. in his group. He could not progress rapidly in my understanding of this research without His guidance, valuable advices, and encouragements.

He would also like to deeply thanks my co-supervisor, Prof. Makoto Sekine, Plasma Nanotechnology Research Center, Nagoya University, and associate Prof. Hiroki Kondo, Department of Electrical Engineering and Computer Science, Nagoya University, for lots of valuable comments.

At same time, he wish to express my sincere gratitude to the vice-adviser, Prof. Kazuo Nakazato, Department of Electrical Engineering and Computer Science, Nagoya University, for his valuable suggestions and discussions in progressing this research. He also thank to the vice-adviser, Prof. Kazuo Shiokawa, Solar-Terrestrial Environment Laboratory, Nagoya University, and Prof. Fumihito Arai, Institute of Innovation for Future Society, Nagoya University, for giving the big motivation for the passionate research.

He would like to express my appreciation to Prof. Masafumi Ito, Department of Electrical and Electronic Engineering, Meijo University, and associate Prof. Takayuki Ohta, Department of Electrical and Electronic Engineering, Meijo University, for collaborating and giving regular and valuable advices.

He is also grateful to the entire staff in Hori and Sekine's Lab., Prof. Kenji Ishikawa, Plasma Nanotechnology Research Center, Nagoya University, Assistant Prof.

## Acknowledgements

Keigo Takeda, Department of Electrical Engineering and Computer Science, Nagoya University, and associate Prof. Satomi Tajima, Plasma Nanotechnology Research Center, Nagoya University, Dr. Hiromasa Tanaka, Institute of Innovation for Future Society, Assistant Prof. Hiroshi Hashizume, Institute of Innovation for Future Society for their valuable comments and suggestions. for their fruitful discussion and valuable comments. The author would like to acknowledge Dr. Koji Yamakawa at Katagiri Engineering Co., Ltd. for their helpful advices and discussions.

He appreciates Prof. Uwe Czarnetzki, Ruhr University Bochum, for giving me the opportunity to study in her group. His guidance and valuable advices allowed me to progress in my understanding on plasma physics. He would like to appreciate deeply Mr. Steffen Meier and Dr. Tsanko Tsankov, and Dr. Shinya Iwashita for collaborating and giving valuable advices. Big thanks to all members of Prof. Czarnetzki's group.

The Author appreciates Prof. Timo Gans, York University, for giving me the opportunity to study in his group. His guidance and valuable advices allowed me to progress in my understanding on plasma physics. The author would like to appreciate deeply Dr. Deborah O'Connell and Dr. Arthur Greb for collaborating and giving valuable advices. A big thanks to all members of Prof. Gans's group.

A big thanks to my colleagues in Prof. Hori and Prof. Sekine's Lab, Dr. Yudai Miyawaki Dr. Shang Chen, Dr. Yudai Miyawaki, Dr. Yusuke Abe, Dr. Takuya Takeuchi, Dr. Takayuki Hiraoka, Dr. Hitoshi Watanabe, Dr. Lu Yi, Dr. Hyung, Dr. Toshiya Suzuki, Dr. Hironao Shimoeda, Mr. Jong Yun Park, Mr. Yusuke Kondo, Mr. Lingyun Jia, Mr. Atsushi Ando, Mr. Mr. Kuangda Sun, Mr. Zecheng Liu, Mr. Kohei Asano, Mr. Jun Kuki, Mr. Ryosuke Kometani, Mr. Atsushi Fukushima, Mr. Tatsuya Komuro, Mr. Takeyoshi Horibe, Ms. Ya Lu, Mr. Leyong Yu, Mr. Jiadong Cao, Mr. Haoran Wang, Mr. Tomoki Amano, Mr. Takashi Kako, Mr. Masayuki Nakamura, Mr. Keita Miwa, Mr. Xu Da, Mr. Yan Zhang, Ms. Sijie Liang, Mr. Shun Imai, Mr. Kazuki Iwamoto, Mr. Takumi Kumakura, Mr. Naoyuki Kurake, Mr. Hirotsugu Sugiura, Mr. Yusuke Fukunaga, Mr.

## Acknowledgements

Takumi Ito, Mr. Kazuaki Kojima, Mr. Peter Pan Mr. Takuya Kurihara, Mr. Shinnosuke Takai, Mr. Takuya Tonami, Mr. Kenichi Naitou, Mr. Ryo Furuta, Mr. Naoki Yoshitake, Mr. Syunichi Sato and all other students who have studied in Professor Hori and Professor Sekine Laboratory for giving the big pleasure in life and creating a most enjoyable work atmosphere.

He also appreciate the enough secretarial supports to Ms. Naoko Kataoka, Ms. Yukie Kase, Ms. Machiko Sakai, Ms. Hiroko Miyagawa, Ms Kotomi Shioya, Ms. Youko Kuwabara, Ms. Alena Chagay, Ms. Asako Nishiyama for lots of encouragements and helpful advices in day-to-day life.

Finally, He would like to dedicate this thesis to my parents, my brothers, my fiancé, and good friends.

*Takayoshi Tsutsumi*

January 2015

## Acknowledgements

## List of Papers

### 1. Original Papers

	<i>Title</i>	<i>Journal</i>	<i>Authors</i>
1	Rapid measurement of substrate temperatures by frequency-domain low-coherence interferometry	Applied Physics Letters, <b>103</b> , 182102 (2013).	T. Tsutsumi, T. Ohta, K. Ishikawa, K. Takeda, H. Kondo, M. Sekine, M. Hori, M. Ito (Chapter 2,3)
2	Robust characteristics of semiconductor-substrate temperature-measurement method using auto-correlation type frequency-domain low-coherence interferometry	Japanese Journal of Applied Physics, <b>54</b> , pp01AB03 (2015).	T. Tsutsumi, T. Ohta, K. Ishikawa, K. Takeda, H. Kondo, M. Sekine, M. Hori, M. Ito (Chapter 2,3)
3	Dependence of wavelength on Silicon-substrate temperature measurement by frequency-domain low-coherence interferometry	(To be submitted)	T. Tsutsumi, T. Ohta, K. Takeda, M. Ito, M. Hori (Chapter 3)
4	Etching Process of organic films with a temporal control of substrate temperature	(To be submitted)	T. Tsutsumi, Y. Fukunaga, M. Ito, T. Ohta, K. Takeda, K. Ishikawa, H. Kondo, M. Sekine, M. Hori (Chapter 4,5)
5	Radial Distribution of Electron Energy and dissociation degree dependence on Wafer Materials in Radio-Frequency Oxygen Plasma Discharge by Energy Resolved Actinometry	(To be submitted)	T. Tsutsumi, A. Greb, M. Hori, D. O'Connell, T. Gans

## 2. International Conferences

	<i>Title</i>	<i>Conference</i>	<i>Authors</i>
1	High Resolution Measurement of Silicon Substrate Temperature Using Frequency Domain Low Coherence Interferometer for Plasma Processing	3rd International Symposium on Advanced Plasma Science and its Applications for Nitrides and Nanomaterials, P1-002A, Nagoya, Japan, Mar. 6-9, 2011.	T. Tsutsumi, T. Ohta, M. Ito, M. Hori
2	Temperature Measurement of Silicon Wafer Treated by Atmospheric Pressure Plasma Using Frequency Domain Low Coherence Interferometer	4th International Conference on PLAsma-Nano Technology & Science, P-50, Gifu, Japan, Mar. 10-12, 2011.	T. Tsutsumi, T. Ohta, M. Ito, M. Hori
3	Non-contact Temperature Measurement of Silicon Wafer Using Frequency Domain Low Coherence Interferometer	5th International Conference on PLAsma-Nano Technology & Science, P-31, Aichi, Japan, Mar. 9-10, 2012.	T. Tsutsumi, T. Ohta, M. Ito, S. Tsuchitani, M. Hori
4	Temperature Measurement of Carbon Nanowall/Silicon Substrate Using Fourier-Domain Low-coherence Interferometry	5th International Conference on PLAsma-Nano Technology & Science, P-35, Aichi, Japan, Mar. 9-10, 2012.	T. Hiraoka, M. Natsume, H. Kato, T. Tsutsumi, T. Ohta, M. Ito, K. Takeda, H. Kondo, M. Hori
5	High Resolution Temperature Monitoring System of Semiconductor Substrate Using Fourier Domain Low Coherence Interferometer	The 15th Korea-Japan Workshop for Advanced Plasma Process and Diagnostics, S02, Suwon, Korea, Jun. 7-8, 2012.	T. Tsutsumi, M. Hori, M. Sekine, K. Ishikawa, K. Takeda, H. Kondo, T. Ohta M. Ito

List of Papers

	<i>Title</i>	<i>Conference</i>	<i>Authors</i>
6	Non-Contact Temperature Measurement of Sapphire Substrate for GaN using Frequency Domain Low Coherence Interferometry	The 11th Asia Pacific Conference on Plasma Science and Technology and 25th Symposium on Plasma Science for Materials, 1-P26, Kyoto, Japan, Oct. 2-5, 2012.	T. Tsutsumi, K. Takeda, K. Ishikawa, H. Kondo, T. Ohta, M. Ito, M. Sekine, M. Hori
7	Non-Contact Measurement of Wafer Temperature for plasma processing Using Low Coherence Interferometry	The 11th Asia Pacific Conference on Plasma Science and Technology and 25th Symposium on Plasma Science for Materials, 1-P24, Kyoto, Japan, Oct. 2-5, 2012.	T. Ohta, T. Tsutsumi, M. Ito, K. Takeda, M. Hori
8	Temperature measurement of substrate with a thin film using low-coherence interference	65th Annual Gaseous Electronics Conference, UF3.00001, Texas, USA, Oct. 22-26, 2012.	T. Tsutsumi, T. Hiraoka, K. Takeda, K. Ishikawa, H. Kondo, T. Ohta, M. Ito, M. Sekine, M. Hori
9	Monitoring of wafer temperature in plasma processing using optical low-coherence interferometry	The 16th International Workshop on Advanced Plasma Processing and Diagnostics, Okazaki, Japan, Jan. 26, 2013	T. Ohta (Invited), M. Ito, T. Tsutsumi, T. Hiraoka, K. Takeda, M. Hori
10	Real time temperature measurements of film-covered-substrate employing Fourier domain low coherence interferometer during plasma processes	5th International Symposium on Advanced Plasma Science and its Applications for Nitrides and Nanomaterials, P1023A, Nagoya, Japan, Jan. 28-Feb. 1, 2013.	T. Tsutsumi, T. Hiraoka, K. Takeda, K. Ishikawa, T. Ohta, M. Ito, H. Kondo, M. Sekine, M. Hori

List of Papers

	<i>Title</i>	<i>Conference</i>	<i>Authors</i>
11	Measurement of carbon nanowalls / silicon substrate temperature by fourier-domain low-coherence interferometry	5th International Symposium on Advanced Plasma Science and its Applications for Nitrides and Nanomaterials, P1022A, Nagoya, Japan, Jan. 28-Feb. 1, 2013.	T. Hiraoka, T. Tsutsumi, H. Kato, K. Takeda, T. Ohta, H. Kondo, K. Ishikawa, M. Ito, M. Sekine, M. Hori
12	Temperature measurement of carbon nanowall / silicon substrate using super-continuum light source on low-coherence interferometry	The 6th International Conference on PLASMA Nano Technology & Science, P-G11, Gifu, JAPAN, Feb. 2-3, 2013.	T. Hiraoka, H. Kato, T. Tsutsumi, T. Ohta, M. Ito, K. Takeda, H. Kondo, M. Hori
13	Precise Rapid Measurement of Substrate Temperature by Frequency-Domain Optical Low-Coherence Interferometry	17th Korea-Japan Workshop on Advanced Plasma Processes and Diagnostics & 4th Workshop for NU-SKKU Joint Institute for Plasma-Nano Materials, Sokcho, Republic of Korea, May 23-25, 2013	M. Ito (Invited), T. Ohta, T. Tsutsumi, K. Takeda, M. Hori
14	Effect of thin films on wafer temperature during plasma processes investigated by non-contact temperature measurement technique	The XXXI International Conference on Phenomena in Ionized Gases, PS4-013, Granada, Spain, Jul. 14-19, 2013.	T. Tsutsumi, K. Takeda, K. Ishikawa, T. Ohta, M. Ito, H. Kondo, M. Sekine, M. Hori
15	Non-contact measurements of substrate-temperature by frequency-domain low coherence interferometry	AVS 60th International Symposium & Exhibition, PS1-TuA10, California, USA, Oct. 27-Nov. 1, 2013.	T. Tsutsumi, T. Ohta, K. Ishikawa, K. Takeda, H. Kondo, M. Sekine, M. Hori, M. Ito,

List of Papers

	<i>Title</i>	<i>Conference</i>	<i>Authors</i>
16	Rapid precise measurements of film-covered-substrate temperatures during plasma processes	The 1st International Conference on Surface Engineering, WEDPM06-5, Nov. 18-21, Busan, Korea, 2013.	M. Ito (invited), T. Tsutsumi, T. Ohta, K. Takeda, K. Ishikawa, H. Kondo, M. Sekine, M. Hori
17	Rapid non-contact measurements of heat fluxes to substrate in nitrogen plasmas	8th International Conference on Reactive Plasmas 31st Symposium on Plasma Processing, 5B-PM-02, Fukuoka, Japan, Feb. 3-7, 2014.	T. Tsutsumi, K. Ishikawa, K. Takeda, T. Ohta, M. Ito, H. Kondo, M. Sekine, M. Hori
18	Accuracy of substrate temperature measurements using optical low coherence interferometry	8th International Conference on Reactive Plasmas 31st Symposium on Plasma Processing, 5P-AM-S02-P04, Fukuoka, Japan, Feb. 3-7, 2014	T. Ohta, H. Kato, T. Tsutsumi, K. Takeda, M. Hori, M. Ito
19	Measurement of Heat Fluxes of Si Substrate from Plasma by Using Frequency Low Coherence Interferometer	6th International Symposium on Advanced Plasma Science and its Applications for Nitrides and Nanomaterials, 03pP29, Aichi, Japan, Mar. 2-6, 2014.	T. Tsutsumi, K. Ishikawa, K. Takeda, T. Ohta, M. Ito, H. Kondo, M. Sekine, M. Hori
20	Effect of Ambient Air Engulfment on Generation of Activated Species in 60 Hz Non-Equilibrium Atmospheric Pressure Ar Plasma Jet	6th International Symposium on Advanced Plasma Science and its Applications for Nitrides and Nanomaterials, 03pP15, Aichi, Japan, Mar. 2-6, 2014.	S. Liang, T. Tsutsumi, A. Ando, K. Sun, K. Takeda, H. Kondo, K. Ishikawa, H. Kano, M. Sekine, M. Hori

### **3. Research Projects**

- International Training Program (Program for incubating young researchers on plasma nanotechnology materials and device processing, conducted by Japan Society for the Promotion of Science) in at Prof. Uwe Czarnetzki research group, Ruhr University, Bochum, Germany, from November 2012 to January 2013.
- The Internship Program in at Prof. Timo Gans research group, York University, North Yorkshire, United Kingdom, from October to November 2013.

### **4. Awards**

- **JSAP encouraging prize**  
73th Fall Meeting 2012, Japan Society of Applied Physics, 11p-E2-8, p.67, Ehime University, Japan, Sep. 11-14, 2012.